Sulfur-based cathodes operated at strict cycling conditions for Li-based batteries

by

Matthew Li

A thesis

presented to the University of Waterloo

in fulfillment of the

thesis requirement for the degree of

Doctor of Philosophy

in

Chemical Engineering

Waterloo, Ontario, Canada, 2020

Examining Committee Membership

The following served on the Examining Committee for this thesis. The decision of the Examining Committee is by majority vote.

External Examiner	**NAME:** Edward Shanqing Zhang **Title:** Professor School of Environment and Science, Griffith University
Supervisor(s)	**NAME:** Zhongwei Chen **Title:** Professor Department of Chemical Engineering, University of Waterloo
Internal Member(s)	**NAME:** Michael Fowler **Title:** Professor Department of Chemical Engineering, University of Waterloo **NAME:** Jeffrey Gostick **Title:** Professor Department of Chemical Engineering, University of Waterloo
Internal-external Member	**NAME:** Rodney Smith **Title:** Assistant Professor Department of Chemistry, University of Waterloo
Other Member(s)	n/a

Author's Declaration

This thesis consists of material all of which I authored or co-authored: see Statement of Contributions included in the thesis. This is a true copy of the thesis, including any required final revisions, as accepted by my examiners.

I understand that my thesis may be made electronically available to the public.

Statement of Contribution

The body of this thesis is based on a combination of adapted published work. Various sections are adapted from the following list of publications.

Chapter 1

Li, M.; Lu, J.; Chen. Z.; Amine, K., 30 years of Lithium-Ion Batteries. *Advanced Materials* **2018,** *30*, 1800561.

- M. Li and J. Lu formulated the structure, retrieved and analyzed the references.
- M. Li wrote the manuscript.
- J. Lu, Z. Chen and K. Amine revised and edited the review.

Li, M., Chen, Z., Wu, T., Lu, J. Li_2S- or S-Based Lithium-ion Batteries, *Advanced Materials*, **2018**, *30*, 1801190.

- M. Li and J. Lu formulated the structure, retrieved, and analyzed the references for this review.
- M. Li wrote the manuscript.
- Z. Chen, T. Wu and J. Lu, revised and edited the review.

Chapter 3

Li, M.; Zhang, Y.; Wang, W.; Ahn, W.; Jiang, G.; Feng, K.; Lui, G.; Chen, Z., Gas Pickering Emulsion Templated Hollow Carbon for High Rate Performance Lithium Sulfur Batteries. *Advanced Functional Materials* **2016,** *26* (8408-8417).

- I directed the project and performed all synthesis experiments with the general help of Y. Zhang.
- X. Wang, W. Ahn, K. Feng, G. Lui and G. Jiang helped analyze the data and review the manuscript.

Chapter 4

Li, M.; Zhang, Y.; Bai, Z.; Liu, W.; Liu, T.; Gim, J.; Jiang, G.; Yuan, Y.; Luo D.; Feng, K.; Yassar, R.; Wang, X.; Chen, Z.; Lu, J., A Lithium–Sulfur Battery using a 2D Current Collector Architecture with a Large-Sized Sulfur Host Operated under High Areal Loading and Low E/S Ratio. *Advanced Materials* **2018,** *30* (1804271).

- I performed all synthesis experiments, electrochemical testing, and analysis with the general help of Y. Zhang, L. Dan, and Z. Bai.

- W. Liu helped with the synthesis of graphene oxide.
- T. Liu and J. Gim helped with the synchrotron-based X-ray diffraction experiment and data analysis.
- Y. Yuan performed the transmission electron microscopy on the material.
- R. Yassar provided access to their transmission electron microscope.
- G. Jiang helped with discussion of general scientific topics.
- X. Wang, Z. Chen, and J. Lu provided overall guidance and helped review the manuscript.

Chapter 5

Li M.; Bai, Z.; Li, Y.; Ma, L.; Dai, A.; Wang, X.; Luo, D.; Wu, T.; Liu, P.; Yang, L.; Amine, K.; Chen, Z.; Lu, J., Electrochemically primed functional redox mediator generator from the decomposition of solid state electrolyte. *Nature Communications,* **2019,** Article Number:*1890* (10).

- I directed the project and performed all characterization experiments with the help of Z. Bai, A. Dai, D. Luo.
- Y. Li, X. Wang, and P. Liu synthesized and characterized the Li_3PS_4.
- L. Ma and T. Wu performed and helped the analysis and understanding of the X-ray absorption spectroscopy data.
- L. Yang, K. Amine, Z. Chen and J. Lu provided general advice for the project and helped edit the manuscript.

Chapter 6

Li M.; Shi J.; Son, S.; Luo, D.; Bloom, I.; Amine, K.; Chen, Z.; Lu, J., In situ polysulfide injector for the activation of bulk lithium sulfide. **2020,** in preparation

- I directed the project and performed all characterization experiments with the help of J. Shi and D. Luo.

- S. Son and I. Bloom performed and helped interpret the X-ray photoelectron spectroscopy data.
- K. Amine, J. Lu and Z. Chen provided general advice for the project.

Abstract

With widespread investments from the transportation sectors, the electrification of a significant portion of the transportation market appears to be on the horizon. However, the range and price of these vehicles remains a challenge and hinders the full market penetration of electric vehicles into the world markets. Although economies of scale can decrease the price of electric vehicles, at the core of the problem is the rising price of cobalt and the limited energy density of lithium ion batteries.

Next-generation battery technologies that rely on sulfur-based cathode have great potential in terms of cheap raw materials and higher energy density. Such a technology is perfect for increasing the range and decreasing the cost of electric vehicles. Lithium-sulfur battery (the most common configuration of a sulfur-based cathode) has many technical challenges that hinder it practical application. The combination of the notorious polysulfide shuttle effect, electron insulating nature of reactants/products and volume expansion of active material, has rendered the cyclability of lithium sulfur batteries very poor. Indeed, much progress have been achieved in the recent years, but the low areal loadings and high electrolyte contents (relaxed testing conditions) used for these cells are too low to be of any practical significance. Lithium-sulfur batteries operated at strict conditions have challenges that are amplified when compared to their relaxed testing conditions (low loading/high electrolyte content) counterparts. Adding onto the problems of the cathode, the decades-long task of resolving the challenges associated to Li metal anode also remains to be solved. Together, these challenges have prevented any significant commercial application of a sulfur-based cathode.

In this thesis, we look to study, explore and enhance the performance of sulfur-based cathode tested at strict conditions (sulfur areal loading of ≥4 mg cm^{-2} and electrolyte to sulfur ratio

of ≤8 μL $mg^{-1}{}_{S}$). Two class of sulfur-based cathodes will be presented to bypass and resolve the problems associated with strict conditions testing, successfully achieving significantly enhanced performance. The first class will be presented in Chapter 3 and 4. Chapter 3 will be the investigation of a specific carbon material with hollow structures and a porous shell with the objective of surpassing commercial carbon material in terms of performance at first relaxed testing conditions. An emulsion-based polymerization technique was used to simultaneously create large macropores in the form of hollow structure and mesopores on the shell. Significant performance improvements were observed in terms of rate performance and cycle life. In Chapter 4, this material was tested at strict conditions through further development by employing an aerosol based agglomeration technique. We found enhanced performance at strict conditions, but the performance was still not ideal. Noting from the research trends in literature, we decided that the use of Li metal is quite detrimental to the performance of sulfur-based batteries. Therefore, our subsequent work focused on a second class of sulfur batteries, that is, the Li_2S cathode. This unique configuration of a sulfur-based cathode bypasses the need of using a metallic Li metal as the Li can now be sourced at the cathode. However, Li-ion extraction (charging) from the commercially available Li_2S is difficult and requires inefficient electrochemical activation. Chapter 5 and 6 will be focus on the identification and application of electrode additive to activate commercially available Li_2S. These techniques have a large emphasis on ease of implementation and functionality at strict testing conditions. The first material is Li_3PS_4, which was found to function down to 10 wt.% in the electrode composition. The second is Na_2S, which was found to function at an exceptionally low 1 wt.% in the electrode composition. Notably, both of these techniques do not require sophisticated material synthesis techniques and take readily commercially available material to achieve exceptional performance at strict conditions.

Chapter 7 presents a summary of the findings in this thesis. Overall, this thesis demonstrated two different sulfur-based cathodes which can successfully function at low electrolyte to sulfur ratios and high sulfur areal loadings. A brief discussion will be given on potential future research directions of sulfur-based batteries and areas that require further improvements.

Acknowledgements

I would like to thank my supervisor, Prof. Zhongwei Chen, for supporting and guiding me throughout my studies, and giving me the freedom to pursue different research avenues. I would also like to thank Dr. Khalil Amine and Dr. Jun Lu at Argonne National Laboratory for providing research guidance throughout my stay at Argonne National Laboratory. I would like to thank Dr. Yining Zhang for offering me indispensable direction, collaborative efforts and invaluable advice towards my thesis research throughout the past several years.

I would like to thank my family for supporting me. I would also like to thank all my lab mates at both the University of Waterloo and Argonne National Laboratory for accompanying and helping me over the past few years. Special thanks to Dr. Gaopeng Jiang and Dr. Fathy Hassan for their patience in general scientific discussions, Dr. Yingying Xie, Dr. Jerry Xu, Dr. Tao Zhang, Dr. Lu Ma, Dr. Qidong Li, Dr. Yingbo Li, Dr. Xuanxuan Bi, Dr. Yifei Yuan, Yu Lei, Dr. Pan Xu, Dr. Kun Feng, Dr. Tongchao Liu, Dr. Xiaogang Fu, Dr. Meiling Xiao, Dr. Jianbing Zhu, Dr. Wenwen Liu, Dan Luo, Professor Wook Ahn, Professor Jingde Li, Professor Ge Li and Professor Xiaolei Wang for collaborative opportunities outside of my direct field and projects.

Finally, I am immensely grateful towards the Natural Science and Engineering Research Council of Canada (NSERC) and the Waterloo Institute for Nanotechnology and the University of Waterloo for their financial support throughout my career as a graduate student.

Table of Contents

List of Figures

List of Tables

List of Abbreviations

LIB	Lithium-ion Battery
LSB	Lithium-sulfur Battery
SEM	Scanning Electron Microscopy
TEM	Transmission Electron Microscopy
XRD	X-ray Diffraction
TGA	Thermal Gravimetric Analysis
CNT	Carbon Nanotube
BET	Brunauer–Emmett–Teller
EIS	Electrochemical Impedance Spectroscopy
LiTFSI	Bis(trifluoromethane)sulfonamide lithium salt
$LiPF_6$	Lithium hexafluorophosphate
DOL	1,3 dioxolane
DME	dimethoxyethane
KB	Ketjen Black 600 JD
PS	Polysulfide
MF	Melamine Formaldehyde Resin
EV	Electric vehicle

SEI	Solid Electrolyte Interphase
SC	Shuttle Current
DOD	Depth of Discharge
GO	Graphene Oxide
LPS	Li_3PS_4

Chapter 1: Introduction

Batteries are becoming more and more intertwined with the core operations of society. From electric vehicles (EV) to grid storage and even to novelty items such as smartwatches, modern applications for batteries are endless. One of the most common modern-day battery technologies is the lithium-ion battery (LIB). Many automotive companies are trying to develop commercially viable electric/ hybrid vehicles in response to concerns regarding climate change. If the electricity that is utilized in these vehicles are generated from a clean source (solar, wind, hydro, geothermal and nuclear), this change in transportation technology can serve to significantly reduce our release of greenhouse gas to the atmosphere. Unfortunately, the high price of EVs and their comparatively shorter driving range limits their practical application. Tesla's effort in bring electric vehicles to market has received significant attention from the consumer market and acquired over 400,000 pre-orders on their unreleased Model 3 ($35,000 USD) hinting at its popularity and potential to finally be able to break out of its niche transportation market. Additionally, Tesla has committed itself to create fast charging stations reasonably spaced throughout the United States of America and even placed in overseas countries such as China. It is important to realize that a boost in infrastructural support for EVs is only half of the problem at hand. Significantly more time is required to recharge/refuel for EVs when compared to internal combustion engine-based vehicles. When coupled with the typically lower total driving range and relative scarcity of recharging stations, consumers have brought forward the concern of range anxiety. Arguably, following this initial introduction of battery based EVs into the consumer market, nearly all other well-known automakers have begun to invest heavily into similar technologies with recent product lines that features hybrids to full EVs vehicles.

1.1 Lithium-ion batteries

Section 1.1 of Chapter 1 has been partially adopted and modified with permission from Advanced Materials

M. Li, J. Lu, Z. Chen, and K. Amine, 30 years of Lithium-Ion Batteries, Advanced Materials, 2018, 30, 1800561.

Batteries have been an energy storage device used by mankind for centuries. The earliest form of the battery could be dated back to a 2000-year old clay jar with copper cylinders and iron rods found in Baghdad. Modern cells can be categorized into two different configurations: primary and secondary. Secondary batteries are rechargeable whereas the primary cells are not. The rechargeability of secondary batteries stems from the reversible nature of the redox reactions that occurs at each electrode of the cell. Planté developed the lead acid battery which was the first secondary battery in the year of 1859. Over the years, many other technologies have emerged such as nickel metal hydride (NiMH) which has gained substantial commercial popularity. NiMH batteries have been vastly implemented in the early electric vehicle markets, such as the Toyota Prius. However, other technologies such as the NiCd battery have been phased out due to its negative effects on the environment. Newer electronics such as smartphones, laptops, tablets and even electric vehicles all contain what is known as the lithium-ion battery (LIB). Being more compact and lightweight, the LIBs have grown to hold a major portion of the battery market.[1]

1.1.1 Principle of operation of commercial Li-ion batteries

Like all electrochemical systems, a lithium ion battery (LIB) consists of a cathode and an anode. Commercially available LIBs consist of lithium metal oxide cathodes such as $LiCoO_2$ (LCO, for portable electronics) or the more contemporary $LiNi_xMn_yCo_zO_2$ (NMC, where $x + y + z = 1$)/$LiNi_{0.8}Co_{0.15}Al_{0.05}O_2$ (NCA, for electric vehicles), and a graphite-based material for the anode.[2] Both electrodes operate under the principles of lithium intercalation. The basis of this technology dates back to work by Stanley Whittingham at Exxon in the late 1970s where reversible Li-ion intercalation was observed for TiS_2 with intense commercial interest.[3] The mechanism of energy storage in Li-ion batteries (LIB) lies in the Li-ion being transferred from the anode and intercalated into the layered lattice structure of the cathode material. During discharge, the battery operates as a Galvanic cell where electrons are transfer from the anode to the cathode, converting the difference in chemical potential into electric work. After delivering the power to the electric load (vehicle, cell phone, etc.), to recharge, an external voltage is applied to induce the transfer of the Li^+ from the low chemical potential cathode back to the higher chemical potential to recharge the battery (operating as an electrolytic cell). During operation, the Co and Ni typically serves as the redox center (cationic redox centers[4,5]) while the Mn or Al acted as thermal and cycle stabilizer.[6] The voltage of charge is also of concerns because it controls the degree of delithiation in the lithium metal oxide, possibly inducing unwanted phase transformations if not controlled properly, leading to quick battery cycle degradation. In fact, at high enough charge voltages/state of charge, oxygen (anionic) redox begins to occur.[7] The switch from a cationic redox center to an anionic redox center has been a topic of much discussion in the field of LIBs because it offers an avenue for activating additional energy density for next generation LIBs. However, its practical relevance has yet to be proven even when very exotic transition metal oxides are used in the cathode composition.[8] If anionic redox is accessed in traditional NMC materials, it typically leads to irreversible and ultimately detrimental O_2 gas evolution.

In terms of material selection, LCO had initially a dominant presence in the market due to lack of an alternative. However, the use of NMC and NCA began to dominate the battery market as both academia and industry began to understand its properties and synthesis techniques. The advantage of NMC and NCA lies in their lower Co content, which equates to a lower manufacturing cost. It is this difference in cost that has allowed LIBs application in EVs applications.[9]

In addition to the electrode materials, an electrically insulating and Li^+-permeable membrane separates the cathode from the anode. This membrane or so-called separator is crucial to ensure that the electron transfers via the external circuit and does not undergo internal cell short-circuiting. However, this membrane cannot be too thick to reduce its impact on the specific and volumetric energy density. The separator is wetted by an organic-based electrolyte of low viscosity and high Li^+ mobility at room temperature. If the mobility of Li^+ is low, the experienced overpotential of the battery will be increased and could cause the cell to prematurely reach its cycle cut-off voltage resulting in loss in energy density. Typical salts used in the electrolyte includes $LiPF_6$ for LIBs and LiTFSI for lithium sulfur batteries. Most important of all, the electrolyte must be stable in a relatively wide voltage window, and operating temperature to decrease the chance for a catastrophic failure of the cell. The operating voltage window of a battery system is limited by first the cathode and anode chemical potential and then the stability of the electrolyte. Anodic stability at the electrolyte/cathode interface is considered a relatively minor problem (albeit still a problem in some performance stressing conditions[10]) when compared to the initial problems associated with the cathodic electrolyte decomposition on the anode. It is very difficult to find an electrolyte composition that is stable against the highly reductive power of a lithiated graphite. The solution to this problem is the formation of a solid-electrolyte interphase (SEI) which is electronically insulating but Li-ion conductive and insoluble in the electrolyte. Accordingly, the first cycle of each freshly formed LIBs is known as the formation cycle, where the LIB is charged (shuttling Li-ions from the cathode to the graphite anode). Upon lithiation, the graphite will reduce and decompose the electrolyte into the SEI, effectively passivating the anode from further decomposing the electrolyte. It is worth noting that the SEI has been known as one of the final enablers of the modern LIBs.[9]

The traditional method to manufacture LIBs is to first formulate and then cast a battery slurry onto an aluminum (for cathode) or copper (for anode). The choice of current collector has been established based on the voltage window of these materials and their raw material cost. A crucial component of the slurry is the conductive additive. Because the active material (metal oxide) typically only have moderate electron conductive, it requires the use of conductive additive such as various types of carbon black to enhance the electrical conductivity of the cathode. Furthermore, the use of a binder is required to obtain a mechanically robust electrode with good adhesion between all electrode components throughout the slight volume variations during cycling. Typically, this binder is made of various polymers such as the water-soluble sodium carboxyl methylcellulose with styrene butadiene and the organic solvent-based polyvinylidene fluoride. The binder is required to have good surface interaction to ensure good adhesion between the active material, conductive additive and current collector. The viscosity and solid content of the slurry is of great importance when controlling the areal mass loading of the active material (in mg cm^{-2}). Finally, the method of which the electrode is dried will affect its porosity. This typically includes the atmosphere, temperature and convection rate are optimized to obtain a certain desired electrode quality.

1.2 Limitation of Li-ion batteries

Current LIB technology has several disadvantages ranging from slow recharge and discharge rates to temperature sensitive cycling performance. However, the most important parameters for enabling a battery’s application in electric devices are the battery’s energy density.

How much energy the LIB can store on a given charge and, how long is required to recharge an electronic device reduces to a matter of the energy density of the battery. Unfortunately, the energy density of current LIB material is reaching its theoretical limit. Traditionally, the redox centers for LCO is the Co atom providing cationic redox capabilities. Current research trends have pushed towards oxygen redox (anionic redox) to achieve higher energy densities but have ultimately failed due to the sharp decline in cycle stability. To put this into perspective, the theoretical practical gravimetric energy density taking into account all the cell components is ~250 Wh kg^{-1}.[11,12] The state of the art LIBs have an energy density of 210 Wh kg^{-1}. [11] This indicates that only a mere 20% further improvement can theoretically be made if LCO is used. This limitation stems from the inherent ability of the metal oxide and graphite to uptake and accommodate Li^+ into its crystal lattice. As the chemical formula of LCO suggests, only a ratio of one mole of Li-ion per one mole of CoO_2. A calculation based on molar masses indicates that at least 13 grams of deadweight metal oxide exist for every gram of lithium in the battery indicating that the lithium only represents 7% of the total mass of the cathode's active material. A more convenient representation would be to measure how much charge or specific capacity the cathode material can take, typically expressed in mAh g^{-1} to align with popular convention. The lithiation of the cobalt oxide cathode material theoretically has a specific capacity of 274 mAh g^{-1}.[13] As such, one strategy to improve the energy density is to find a host for Li-ions which forms compounds with a higher Li-ion to deadweight host material ratio. Another is to utilize a material that has a higher voltage versus the anode (lithiated graphite). In the field of LIBs, the current most promising category of material are the anionic redox active materials. These mainly fall into two categories, Li-rich layered metal oxides[14] and Li-rich disordered rock-salt[15] both possessing possibilities in achieving significantly higher energy density, while also possessing detrimental problems. Although some work has been conducted to mediate these problems, they typically require very expensive transition metals such as Ru[16] or Ir, [17] which are practically impossible.

In contrast, another possible candidate of cathode material is sulfur, possessing substantially lower cost and higher capacity for Li-ions than any of the metal oxides. Sulfur-based batteries come in two major forms. The most common is a sulfur cathode paired with a metallic Li anode (known as a Li-S battery, LSB). The other is a Li_2S base cathode (Li-source in the cathode) and a Li-metal free anode such as graphite, silicon. While in this thesis we did not investigate the full-cell performance of a Li_2S-based cathode, the advantage of a Li-metal free anode is that Li metal batteries are exceptionally challenging to achieve commercially. While over the past few years there has been many contemporary efforts devoted to Li-metal anodes, its overall performance is still well below commercial levels, especially at low electrolyte content conditions.

1.3 Sulfur-based batteries

The emerging electronic markets and global warming concerns has pushed researchers to look for more ambitious battery concepts (anode and cathode selection) that has been previously abandoned due to engineering difficulties. The selection of better cathodes and anodes has been discussed by Liu *et al*.[18] One of the most important criteria is the energy density which is the product of the electron capacity of the redox reaction and the voltage of that reaction. The calculation of the capacity of the redox reaction involves the stoichiometric calculation of the number of electron transfer per mass of lithium host. The capacity of various redox pairs can therefore be easily estimated if the redox reaction stoichiometries are known.

The redox potential or voltage of a redox pair can be estimated from tabulated Gibbs free energy (after some calculations). It can also be roughly correlated to the ionization energy and electron affinity trends in the periodic table, where the more electronegative cathode material (oxidizing power) of the chalcogen and halogen groups can serve to be decent cathode material. The alkali and alkali earth metals can be easily identified as the easiest groups to ionize, indicating its potential as anode active material. More complex chemicals such as metal oxides compounds also roughly follow the same trends. For example, metal oxides in the fourth period such as NiO_2, CoO_2, FeO_2 are on average more oxidizing (better cathode i.e. higher lithiation/delithiation potentials) than those in the fifth period such as MoO_2 and RuO_2. Additionally, the metal oxides in the same period are more oxidizing the further right the metal elements are located on the periodic table. Sulfur, located in the chalcogen group, possesses a multiplateau discharge potential ranging from 2.3-2.1 V vs Li^+/Li. Although this potential is lower than commercial metal oxide cathode materials (~3.9-4.35 V vs Li^+/Li) due to the lack of the stronger oxidizing power of oxygen, the specific capacity for Li-ions of sulfur (~1675 mAh g^{-1}) is significantly superior to commercial metal oxides (due to the different lithium storage mechanism. Overall, sulfur is theoretically a vastly superior cathode material when compared to cathodes of commercial batteries with a theoretical energy density of 2500 Wh kg^{-1}.[19]

1.4 Principle of operation of lithium-sulfur batteries

The operation of an LSB is fundamentally different from a modern-day intercalation chemistry based LIB and relies on the conversion reaction of S to and from Li_2S. In an LSB, the sulfur is dissolved into the electrolyte during discharge upon reduction from its $S_{8(S)}$ form to polysulfides such as S_8^{-2}, S_6^{2-}, etc. A LIB, as stated previously, relies on intercalation of Li^+ into the lattice of the metal oxide crystal structure with or without change in crystal phase. The reduction mechanism of sulfur is much more complex in nature compared to that of metal oxides and remains rather elusive and debated among the research community. The following equations illustrate a proposed reduction pathway:

Equation 1

$$S_8 + 2e^- \leftrightarrow S_8^{2-}$$

Equation 2

$$S_8^{2-} \leftrightarrow S_6^{2-} + \frac{1}{4}S_8$$

Equation 3

$$S_6^{2-} \leftrightarrow 2S_3^{\cdot -}$$

Equation 4

$$2S_3^{\cdot -} + 4e^- \leftrightarrow 3S_2^{2-}$$

Equation 5

$$S_2^{2-} + 6e^- \leftrightarrow 4S^{2-}$$

Equation 6

$$S^{2-} + 2Li^+ \leftrightarrow Li_2S$$

Overall:

Equation 7: Discharge Mechanism of Sulfur in a LSB [20]

$$S_8 + 16Li^+ + 16e^- \rightarrow 8Li_2S$$

Like the LIB, the charge carriers (Li^+) are exchanged back and forth between the cathode and the anode. In this case the product formed when discharged is lithium sulfide (Li_2S), possessing a much higher lithium to dead weight material than CoO_2. As a matter of fact, the specific capacity of sulfur for lithium is actually ~1675 mAh g^{-1} [21] more than 5.6 times that of CoO_2. Although specific capacity is a useful unit of measure of the duration of a discharge cycle, an electrical device requires energy which relates to the voltage of the battery. In terms of energy density (Wh kg^{-1}) sulfur possesses 2500 Wh kg^{-1} if a lithium anode is used in a full cell. After all the other components of the battery such as current collector, separator and electrolyte are taken into consideration, the practical energy density is more along the lines of 700 Wh kg^{-1} , whereas commercially available LIB has only realized 210 Wh kg^{-1}.[11] In short, the LSB can potentially offer an impressive 3-fold increase in energy density.

Sulfur exists at room temperature in its orthorhombic octet solid form. It is sparingly soluble in typical organic electrolyte (1,3 dioxolane and dimethoxyethane). While the discharge mechanism is still debated, one proposed mechanism is that upon accepting electrons, sulfur (S_8 , solid) is first reduced to S_8^{2-} (soluble. Equation 1), which disproportionate to S_6^{2-}(soluble, Equation 2). Based on electron paramagnetic resonance spectroscopy[22] and X-ray absorption near-edge spectroscopy (XANES), [23] it was determined that S_6^{2-} spontaneously forms $S_3^{\cdot -}$ (soluble Equation 3) third-order polysulfide radicals. These radicals are further reduced to S_2^{2-} (soluble, Equation 4) and finally to S^{2-} (Equation 5), which precipitates as Li_2S (Equation 6). The intermediate series of sulfur oligomers have been colloquially called lithium polysulfides (LiPS).

All the reactants, intermediates and products of this battery chemistry can undergo some form of disproportionation or comproportionation reaction throughout the course of cycling. In fact, just the physical simple mixing of mostly insoluble solid Li_2S and solid elemental S_8 together inside of a polysulfide soluble-organic solvent will readily generate solvated LiPS[24] (comproportionation reaction) with the comproportionation and disproportion reactions in equilibrium.[25]

As the initial discharge reactant and final discharge products are insoluble, the operation of an LSB entails some form of "electro-stripping" and electrodeposition over the course of a single discharge. Similarly, upon charge the insoluble Li_2S are dissolved and redeposited as sulfur at the end of the cycle. Unfortunately, LSB technology has yet to be used in mainstream electronic devices due to many technical challenges centered on the complex discharge/charge mechanism of sulfur. These challenges result in extremely poor cycle stability and poor practical capacity from sulfur nullifying all its benefits for secondary battery applications.

1.4.1 Technical challenges

The challenges of LSB can be described by three main points. The first is the 80% volumetric expansion of sulfur after lithiation. This is problematic because the volume expansion can lead to disconnection of lithiated sulfur (Li_2S) from the circuit. Furthermore, a volumetric expansion would possibly lead to an overall macroscopic expansion of the whole battery resulting in packing problems. This expansion is not so much a concern at this point of the LSB research field because most sulfur cathode already possesses an excess amount of void space built into its architecture. These void spaces are not necessarily created for mitigating the effects of volumetric expansion but are created with the intention to allow more electrolyte to contact the sulfur, which leads to the discussion of the next two problems. The next two problems are significantly more detrimental to the performance than the first. The second problem stems from the fact that sulfur is a very good electrical insulator, much better than its metal oxide cathode counterparts. This would commonly require some sort of conductive additive in the electrode to efficiently deliver electrons to the sulfur. In the case of LSB, the simple incorporation of conductive additive is usually insufficient to ensure good performance because of the third problem. The third problem is the dissolution of sulfur into the electrolyte during discharge. This works synergistically with the second problem (sulfur's low electron conductivity). The dissolution/deposition of sulfur and Li_2S upon cycling leads to the possibility of undesired redistribution of sulfur among its conductive matrix. This usually creates large agglomerates of sulfur throughout the battery. Regardless of what is used as a conductive additive, it must be homogenously dispersed within the cathode and maintain intimate contact with all the sulfur. If sulfur is redistributed and agglomerated during cycling, the homogeneity and intimacy of electrical contact would be compromised. Adding to this, the dissolution of sulfur into the electrolyte changes the fundamental mechanism of the reaction. No longer are the Li^+ simply entering and positioning itself in a crystal lattice structure of metal oxides, but the reduction and oxidation mechanism of LSB are a series of complicated redox reaction where the physical state of matter changes from solid to solvated salts in liquid. Reactions sites are dictated by not only the availability of Li^+ and electrons (in the case of metal oxides) but also on the availability of solvated polysulfide anions (PS). PS species if not reduced quickly upon generation, has the possibility of diffusing away from reaction sites out of the cathode, losing its availability for future reduction. Moreover, the leakage of PS out of the cathode leads to consumption by unwanted side reactions. The first set of side reactions are the disproportionation of PS at different oxidation states and results in precipitation of solid S_8 in potentially electronically inaccessible locations in the battery. The second set of reactions occur on the lithium anode. Once the PS escapes the cathode, it can further diffuse to the surface of anode and directly complete a redox reaction on the anode circumventing the electron transfer across the external circuit. Simply put, PS can short circuit on the lithium anode resulting in poor capacity. Moreover, the products of these short circuit reactions are usually Li_2S or Li_2S_2 both of which are sparingly soluble in typical LSB electrolyte and electrically insulating. This indicates that any PS that is short circuited on the anode will likely remain electrochemically inactive on the anode throughout the lifespan of the battery because it is extremely difficult to reactive reduced sulfur species on the surface of the Li anode. In a sense, sulfur disconnects itself from the circuit/battery over a few cycles and results in a quick decrease in battery capacity.

Finally, the last problem is a low Coulombic efficiency. Because higher order PS can be short circuited/reduced directly on the lithium anode, it opposes the act of recharging. Specifically, during charging, higher PS are generated at the cathode. For example, sulfur at its -2 oxidation state, when charged is oxidized to -1, -2/3, -2/4, -2/6, -2/8 and then finally to 0 upon full charge. This complex oxidation reaction mechanism results in some mass transfer complications. Once the initial soluble -2/6 or S_6^{2-} polysulfide species are generated/charged from S_4^{2-} at the cathode, they will be allowed to diffuse to the anode (shuttle effect), discharging themselves once in contact with the anode and reduces/discharges back to its -2/4 or S_4^{2-} oxidation state. This re-discharged S_4^{2-} must be recharged once again at the cathode. This counterproductive self-discharge mechanism intrinsic of charging an LSB with a polysulfide soluble electrolyte is reflected in its poor Coulombic efficiency, creating cells which deliver significantly less amount of electrical energy than which was initially “stored” in them. Typical LIB cells have above 99% Coulombic efficiency, indicating for every 100 electrons that was stored in the battery, 99 can be extracted. In the case of LSB, without any effective mitigation strategy a Coulombic efficiency of 40% will be typically obtained.[26]

1.4.2 Literature review of LSB

As stated in the previous section, LSB has many problems: poor practical capacity, poor cycle durability and low coulombic efficiency. These problems must be addressed before any commercialization of LSB can be made. Although known since the 1970s, research into LSB have been halted until recent years. Many groups around the globe have begun to solve these three problems since 2009. The pioneering work of Ji, Lee and Nazar has brought forward the use of porous carbon. After impregnation of sulfur into the pores, the wall of these pores can serve both as a conductive matrix while the complex pore network can increase the diffusion resistance of PS [27]. Ji *et al* has successfully prevented major S redistribution, PS shuttle and allow for LSB cell with significantly higher cycle stability. Boasting an initial discharge capacity of 1000 mAh g^{-1} (60% of theoretical) and remained relatively stable for 20 cycles. Since then, many concepts have been tested to overcome the problems with the LSB battery. These concepts typically fall into one of three categories, modification of the separator,[28,29] electrolyte [30,31] and electrode material design. Modification of separator involves the application of Li^+ selective film that hinders PS diffusion. Typical examples involve, graphene, porous carbon and lithiated Nafion coatings on the separator. Additive is used in electrolyte to limit the dissolution of sulfur. For example, researchers attempted to add PS into the electrolytes and due to the common-ion effect, the dissolution of new sulfur is hindered. Obviously, this is not a complete solution, as the PS additive would decrease the overall energy density of the cell. Researchers have also used ionic liquid as the electrolyte. The so-called tailor made solvents can be designed such that PSs are insoluble, Li^+ conduction is sufficiently high while at the same time remain stable in the operating voltage of the cell. Modification of the cathode material usually incorporates the use of some porous network to house the sulfur. A high pore volume and high surface area material is usually used for accommodating the less dense discharge products and efficient delivery of electrons to the insoluble redox reactant and products. Recent electrode material designs incorporated the use of graphene foams, [32,33] carbon nanotubes [34] and various types of porous carbon[35,36] as conductive S housing. In attempts to mitigate the effects of the PS shuttle, researchers aim to increase tortuosity of the diffusion pathway with complex pore structures. Furthermore, sulfur housings usually have some PS adsorption mechanism which can further limit the PS diffusion out of the cathode. Various other chemical species such as metal oxide, atomically doped carbon and polar functional groups have been introduced into the cathode to attract and retain PS [33,37,38]. Cycle stability have been improved to the point where 1500 cycles can be achieved in the laboratory with capacities well over 70% of theoretical is achievable a low areal sulfur loading <2 mg cm^{-2}.

Despite the large volume of publications, a relatively small portion of work has been performed at practically/commercially relevant conditions. One important metric for practicality is the energy density, which directly relates to the areal sulfur mass loading (in mg_s cm^{-2}). Recently Pope *et al* published an informative review,[19] that describes the relationship between sulfur loading per area and battery energy density. This review states that most LSB studies report thin film LSB with forecasted full battery energy densities that are not even comparable to current LIB. Nearly 9 years after the ground breaking work of Ji et al [27], recent works still mainly focusses on the material at 1-2 mg cm^{-2}.[19] Interestingly in the past years (2015-present) the volume of papers which discusses high loading LSB has increased.[39,40] Some notable work by Professor Donghai Wang's group [38,41,42] has achieved high sulfur loading electrodes up to 5 mg cm^{-2} and Professor Arumugam Manthiram's group has achieved incredibly high sulfur loadings of up to 61.4 mg cm^{-2} with decent stability up to 100 cycles. The performance of LSB has improved dramatically in the lab setting throughout the years, but a commercially viable electrode is far from realization due to the new emerging stability problems of high areal loading electrodes and lack of commercializing power of some of the electrode designs.

1.5 Emerging problems of lithium-sulfur batteries tested at strict conditions

LSBs as a system has been essentially “solved” when looking at low areal loading/high electrolyte content literatures [43] revealing cycle life on the order of thousands of cycles. However, recent reports of sulfur loading of >4 mg cm^{-2} reveal drastically decreased cyclability to only a couple hundreds of cycles.[44] This decrease in stability is inherent to the increased areal sulfur mass in the cell. The increase in sulfur mass per unit area increases the total absolute required current of the battery to maintain an acceptable discharge time, which then imposes a higher current on the Li-metal anode, causing Li deposition problems.

Moreover, the electrolyte to sulfur ratio in an LSB battery system is critical in determining the practical energy density of the final battery product. Typical electrolyte to sulfur ratios are range from 10-15μL mg^{-1},[19] which at a electrolyte specific density of ~1.1 g ml^{-1}, indicates that at 15 μL mg^{-1} (16.5 $mg_{electrolyte}$ mg^{-1}_{sulfur}), the mass of sulfur is only represents 5.7% of the combined electrolyte and sulfur mass with 94.3% of the mass as dead weight. Using this concept and considering other components of the cell, Hagen *et al* has projected a maximum allowable electrolyte to sulfur ratio of 3-4 μL mg^{-1}[45] for LSB technology to even compete with current LIB technologies. Even at this low electrolyte content the proportional of mass of the cell that is taken by the electrolyte is still 32.6%,[45] As such, high electrolyte loading cells are to be avoided due to their impracticality. However, the use of high electrolyte content is beneficial for the fabrication and performance of the cell. For example, a higher electrolyte content can serve to ensure proper wetting of the electrode. Additionally, the higher electrolyte content can decrease the average concentration of the PS in the cells and subsequently the viscosity which can ensure good rate performance of the cell.[46] Whereas, at low electrolyte contents, severe problems with electrolyte wetting, electrolyte evaporation during cell assembly, poor rate performance and rapid “dry out” of cells due to the continuous SEI growth on the typically used Li-metal anode’s surface, significantly reduces the performance. Therefore, much of the works on LSB have incorporated excess amounts of electrolyte to enhance the performance of their cells. However, such high levels of electrolyte completely nullify the energy density potential for commercializing high loading sulfur-based batteries, thus making the electrolyte to sulfur ratio an extremely crucial parameter for any future high loading sulfur-based batteries work. The difficulty in achieving high performance sulfur-based batteries operated at what we will refer to as “strict conditions” i.e. high areal sulfur loading ($\geq$4 mg cm^{-2}) and low electrolyte ($\leq$8 μL mg^{-1}) content remains to be the key barriers against practical sulfur-based battery operation. Moving below <4μL mg^{-1} with a sulfur mass loading above 4 mg cm^{-2} will be denoted as “practically relevant conditions”. Achieving good cyclability at “strict conditions” will represent a significant step towards the commercialization of sulfur-based cathodes. Below is a more detailed description of the challenges with respect to both the cathode and the source of lithium-ions.

1.5.1. Challenges of the Cathode

The increase in current density causes the amplification of the shuttle effect by increasing the flux of PS out of the cathode. Subsequent self-disproportionation (self-redox) reactions that occur and the amplified redistribution of sulfur throughout the cathode severely reduces the cyclability of the cell. Due to the increase in the absolute mass of sulfur in the electrodes, more discharge and charged products are randomly deposited near the surface of the cathode and can cause severe restriction of lithium ion access to parts of and even to the entirety of the electrode. Thus, more careful control and even superior methods of retaining/containing PS inside of the cathode's localized architecture are required. Prevention of PS migration out of their localized hosts is therefore paramount to the success of high loading sulfur electrodes. Overall, the problem set associated with the cathode at high sulfur loadings can be viewed as an amplification of the low loading LSB cells.

Additionally, in contrast to low areal loading and high electrolyte content cells, the wetting process of the electrode becomes nontrivial.[47] The combined negative effect of a thicker electrode film (higher areal loading) and lower ratio of electrolyte content makes it very difficult for fabricating even functional coin cells with very modest performance metrics. [48-50] Specifically, the casting of high sulfur loading films at over 200 µm, often leads to crack and delamination from the current collector. This problem stems from the typical and necessarily high surface area possessed by the sulfur/carbon composite. High surface area is ideal for better contact with sulfur and reaction sites for polysulfide reduction/oxidation. However, the higher surface also makes it very difficult to achieve proper adhesion between particle and the polymer binder. Solution usually involve the use of micron-sized secondary particles, which reduces the "exposed" surface area.[51]

1.5.2 Challenges of the Lithium Source:

Section 1.5.2. of Chapter 1 has been partially adopted with permission from Advanced Materials

M. Li, Z. Chen, T. Wu, J. Lu, Li_2S- or S-Based Lithium-ion Batteries, Advanced Materials, 2018, 30, 1801190. Copyright Wiley-VCH 2018.

Higher current densities associated with a higher areal sulfur mass loading causes the severe stripping/plating of lithium metal from the lithium anode. At low current density, challenges associated with lithium anode are hidden due to minimal lithium material use and as such, lithium anodes are ubiquitously used as both the counter and reference electrode in half cell configurations. However, at higher current densities the problem of using lithium metal as the anode becomes apparent. With an effective infinite volume change upon delithiation (stripping) and lithiation (plating) and dendritic lithium growth the concept of using a lithium anode has been commercially unsuccessful. Researchers have traced the phenomenon of dendrite formation to two mechanisms: tip growth mode, which is due to the mass transfer limited nature of lithium deposition and mossy lithium growth which is derived from the SEI formation on the lithium's surface.[52] Together, these two types of dendritic lithium growth will result in at least the total dry-out of the cell (due to electrolyte decomposition) and at worst, the internal short circuiting posing significant safety concerns.[53]

Various mitigation strategies have been investigated by Professor Lynden Archer's group [54,55] and Professor Yi Cui's group[56] among others with promising results. Mitigation strategies usually falls into the category of a coating/membrane on the surface of the anode surface to limit the mossy lithium dendrites to reach the cathode (short circuit) and added tortuosity to hinder the tip growth mode.[54] Another popular strategy is to design and direct the deposition of lithium through usage of nucleation sites placed inside of hollow carbon material. The performance of such a design offered stability at 1 mA cm^{-2} for up to 150 cycles.[56] Work has also been performed on changing the electrolyte formulations, from ionic liquids[57] to cationic shields with a lower redox potential than lithium such as Cs ions[58] to reduce the electromigration of the anions and maintain a stable electric field across the anode's surface.

While the use of Li metal has been recently a very popular topic throughout the research community, its commercial relevancy is still of question.[59] In a similar fashion as the development history of LSB, the lab-scale testing of LMB at commercially unrealistic conditions (high electrolyte, large excess of Li metal in comparison to cathode capacity) has mostly dominated the literature. Only recently have a few groups been able to produce some modest performance at commercially relevant or even strict conditions.[60-62] With that said it is desirable to look beyond Li metal as an anode for sulfur-based batteries. Other anodes such as Si and graphite are comparatively more stable than Li (at the expense of energy density). While maintaining a higher capacity and cheap sulfur-based cathodes, an alternative type of sulfur-based battery is revealed. With a Li-metal free anode, a Li-ion source must be introduced into the battery. Accordingly, one of the key methodologies to achieve a Li metal free sulfur-based battery is the use of Li_2S as the lithium source.

As a commonly overlooked and a quickly growing field,[63-65] the use of Li_2S holds the key benefit of using sulfur as the main redox center on the cathode while being able to not use a metallic Li anode. Compared to the large volume of LSB literature, research articles featuring Li metal free sulfur-based batteries are rather rare. To the best of our knowledge, there are only 16 published works that pairs a S based cathode with a non-Li metal anode.[63,66-79] Of these works, ~1/3 can be classified as sulfur-based LIBs (S based, Li free cathode) that relied on various prelithiation methods to employ the Li-ion into the system. Prelithiation can be a delicate process and greatly depends on the prelithiation cell setup. If the coin cell configuration is chosen, the researcher must decrimp the coin cell to retrieve the lithiated anode, which could damage the electrode, producing inconsistencies between cells. Other methods such as using a Swagelok cell or direct pressure contact with Li foil in electrolyte might be more suitable due to ease of electrode retrieval, but the lithiation process is hardly scalable. Additionally, any retrieval procedure of the lithiated anode must be performed in an inert environment to prevent reaction with air. Above all, commercial prelithiation of anodes such as Si or graphite will most likely be even more logistically problematic. A widely considered alternative could be the use of the stabilized lithium metal powder (SLMP), but this type of powder can be quite dangerous. Designs of Si anodes would often include some form of nano-sized morphology to mitigate its volumetric expansion/contraction challenges[80] which typically possesses large surfaces areas. The higher surface area of the anode would promote a quick and possibly dangerous lithiation reaction with SLMP. In fact, the most common application of SLMP in LIB literature is to provide a capacity compensation against the slight capacity loss from SEI formation.[81,82] Therefore, the quantities of SLMP often used are much lower than the required amount envisioned in lithiating the entire anode. Furthermore, since the absolute capacities of sulfur-based lithium ion batteries are required to be significantly higher than that of commercial LIB (to compensate for sulfur lower discharge voltage plateau), it is likely that an uncontrolled lithiation of a high capacity anode with SLMP (technically a short circuit reaction) can lead to severe thermal runaways especially when brought to the commercial scale. Even under an inert atmosphere, a metal fire can still occur if the heat transfer is not properly managed. Alternatively, a more promising and scalable method is to introduce lithium into the cathode. Borrowing the idea from commercial lithium metal oxides, the use of Li_2S as starting cathode material not only allows for circumventing the anode prelithiation problems but also offers a few unique advantages over the S electrode.

The first and foremost most important benefit of using Li_2S is its ability to eliminate the need for a Li metal anode. This crucial benefit directly eliminates much of the problems associated to the Li metal anode. The development of a viable cathode alternative that has a Li source (i.e. Li_2S-based cathode) will be key in enabling alternative and more stable anodes such as silicon and graphite. Additionally, compared to Li_2S, sulfur is highly volatile due to its naturally low surface tension and will easily sublimate at slightly elevated temperatures (70-80 ^oC) or partial vacuums,[83] limiting synthesis options and material stability during storage.[84] Even the typical drying process of the electrode laminates can be detrimental to electrochemical performance if not carefully controlled.[85] Finally, it is well known that sulfur experiences a ~80% volume expansion upon being lithiated to Li_2S. This could be detrimental in maintaining a mechanically robust electrode throughout the cycles. Intriguingly, this problem of volume expansion is often overshadowed by the much emphasized polysulfide shuttle effect. A common practice in LSB research is the lack of calendaring which allows for large electrode pore volumes. This conveniently helps to alleviate the problems associated with S volume expansion. Accordingly, work by Lv *et al.* have shown the negative effects on performance after calendaring to a certain thickness, especially for high areal loading cells.[86] The lack of calendaring severely penalizes volumetric energy density estimates of the already intrinsically bulky sulfur material (density $\simeq 2$ g cm^{-3}).[87] Like the hidden symptoms of LSB's Li-anode, it could be expected that the problems associated with volume expansion of sulfur to Li_2S will most likely reveal itself as research into sulfur-based cathodes reach closer to commercial targets. If Li_2S (Li_2S-LIB) is used instead of sulfur (sulfur-LIB), concerns with volume expansion can be effectively mitigated.

While the benefits are clear, the use of Li_2S is far from trivial due to electrochemical inertness of commercial Li_2S.[64] The highly insulating nature (both ionically and electronically) of Li_2S renders it extremely difficult to delithiate (i.e. extract Li-ions). Typical strategies include the decrease in Li_2S particle size to reduce the effects of the conductivity limitations. These techniques typically require complex synthesis methodologies[63,88-90] that introduce a large economic uncertainty if subjected to industrial scrutiny. An alternate and arguably superior strategy is the use of redox mediators, which are soluble species that can be oxidized by the cathode, diffuse to, and then chemically get reduced by Li_2S (oxidation of Li_2S/delithiation).[90-93] We will focus on a new class of Li_2S activation technology that uses initially solid electrode additives that decomposes into redox mediators upon electrochemical activation to achieve cyclability at strict cycling conditions.

1.5.3. Thesis objectives

From our discussion on the challenges relating to operation at strict testing conditions, modification in terms of cathode design must be realized to achieve progress in sulfur-based batteries are achieve. In this thesis, the overarching goal is to achieve cyclability (200 cycles or cyclability with 60% retention) of sulfur-based electrode at “strict conditions,” which we define as high areal sulfur loading (> 4 mg_S cm^{-2}) and low electrolyte to sulfur ratios (<8μL $mg^{-1}{}_s$). Any cycling parameters at lower area sulfur loadings or higher electrolyte to sulfur ratios will be deemed as “relaxed conditions” Such cyclability at strict conditions would represent a significant improvement towards any commercial relevancy for sulfur-based cathode. To achieve this goal, two major strategies will be employed:

The first direction revolves around the lithium sulfur system, that is the starting material is elemental sulfur at oxidation state zero. The intended anode will be Li metal. Two strategies will be investigated, the modification of the cathode. For the cathode, the enhancement of electrolyte infiltration into the cathode structure, while limiting outwards diffusion of polysulfides. This will be achieved by the development of agglomerated hollow structures with graphene shielding and nitrogen doping to prevent dissolution.

The second strategy is the efficient substitution of the elemental sulfur cathode with a Li_2S-based cathode. This will enable the use of other anodes other than metallic lithium. In this context, the word, “efficient” pertains to achieving a lower activation energy, higher material utilization without significant modifications of the Li_2S cathode.

1.5.3 Thesis layout

This thesis explores sulfur-based Li battery systems with an emphasis on achieving performance at strict conditions. Specifically, this means battery cycling at high areal loading and low electrolyte content. There are 7 chapters in this thesis and the overall thesis workflow is shown in **Figure 1-1**. Chapter one introduces the thesis in terms of the challenges, current state-of-the-art, and specific motivation for each research direction selected for this thesis work. Chapter two provides a brief background on the experimental techniques used to characterize and evaluate the materials and designs in this thesis. Chapter three will begin the sulfur cathode-based part of this thesis. Primary, this chapter will discuss about a new methodology we developed for synthesizing hollow carbon with a porous shell. This material significantly outperformed commercially available carbon black at low loading and high electrolyte content (i.e. relaxed conditions). Specifically, the rate performance was particularly impressive with high specific capacity at up to 9C and appears to be promising for testing at strict conditions (of $\geq$4 mg cm^{-2} and electrolyte to sulfur ratio of $\leq$8 μL $mg^{-1}{}_{s}$). Electrochemical testing will be presented with some detailed mechanistic information. Chapter four will bring the material developed in Chapter three, build upon its design through physical particle agglomeration and wrapping with reduced graphene oxide and present cycle life at record high sulfur loading and low electrolytes. Mechanism of failure will be investigated. Chapter five and six will present the work done on moving away from the well documented problems of using a metallic Li anode at strict testing conditions *via* the development of Li_2S based cathodes i.e. changing source for Li-ions. We discuss the first ever implementation of what we named a solid-sourced redox mediator generator for high loading and low electrolyte content electrodes. This technique is key towards achieving sulfur-based batteries at strict testing conditions. Specifically, Chapter five will discuss the first iteration where Li_3PS_4 is used while Chapter six describes the use of Na_2S, a newer more intrinsic redox mediator source that is more effective at lower proportions. The last chapter, Chapter seven will provide a summary and overview of the work presented in this thesis along with future direction of research to further advance the field.

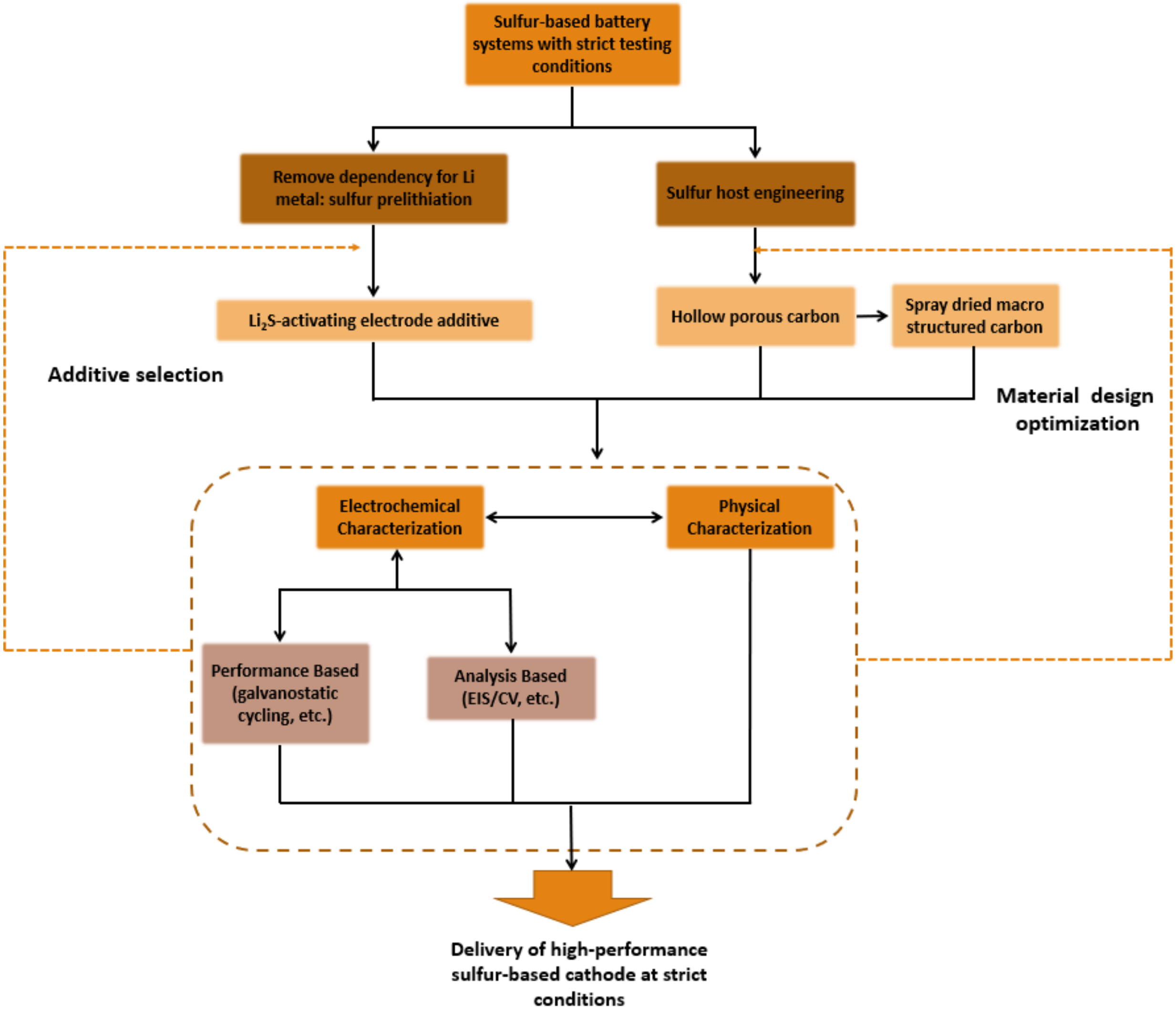

Figure 1- 1: Thesis workflow

Chapter 2: Characterization Techniques

Physical and electrochemical characterization of the various material and LSB cells are important tools to allow for quantitative and qualitative comparison between samples. Physical characterization techniques such as dynamic light scattering, scanning electron microscopy, transmission electron microscopy, X-ray diffraction and thermogravimetric analysis are all used to determine specific traits of the materials. Electrochemical techniques such as galvanostatic discharge is used to emulate actual battery operating conditions, allowing us to gauge the performance of the developed sulfur-based batteries. Furthermore, other electrochemical technique such as electrochemical impedance spectroscopy can offer valuable insight into the nature of mass transfer in a cell. This is especially important when investigating high loading electrodes where diffusion of ions and electron conductance become a major problem. To follow is a brief description of each characterization methods used in the research presented in this thesis

2.1 Scanning electron microscopy

Scanning electron microscopy (SEM) utilizes electron beams to analyze the topological properties of a sample. Fired from an electron gun, the beam is passed through a condenser and focusing lens composed of electromagnetic fields. Once the beam contacts the sample a combination of three events occur. The electrons are reflected, absorbed and excite the electrons within the material. After measuring these signals with detectors, a signal is sent to the computer which creates a real-time image displaying the morphology of the sample. Typical SEMs operate under high vacuum (~10-5 mbar), although SEMs that can operate under low vacuum and even with different atmospheres exists i.e. atmospheric SEMs. A Zeiss Leo FESEM 1530 scanning electron microscope (SEM) is used to characterize the morphology of the materials proposed in this work. SEM will be used in this thesis to characterize the surface morphology of the designed sulfur host material.

2.2 Transmission electron microscopy

Transmission electron microscopy (TEM) enables high resolution images of nanostructured materials. Electrons are ejected from the electron gun (cathode) which is composed of a high voltage applied to a hairpin-shaped tungsten wire. The ground or the anode directs electron flow through a hole in the anode's body and the electron is further passed through and focused by electromagnetic condenser lenses. A liquid nitrogen cooled anticontaminator rod is placed near the objective lens to condense and prevent drifting in of the sample's image. Once the electron has passed through the sample, it is magnified by the projector lens and is projected onto a fluorescent screen of which the user can example their samples morphologies. Like SEM, TEM is also operated under high vacuum of usually 10-5 mmHg to prevent deflection and absorption by atmospheric gas molecules.

2.3 X-ray diffraction

X-ray diffraction is a technique that is used to characterize the crystal structure of samples. The basic concept is that electromagnetic waves such as X-rays, can be diffracted by the crystal structure to form an interference pattern as the wavelength of the X-rays correspond well with the d-spacings of crystalline materials. The intensities of these patterns can be detected and correlated to the structure and ordering of the atoms in the sample. Bragg's law is used to relate the scattering angle to the lattice spacing and is given in the following widely known equation:

Equation 8: Bragg's Law

$$2d\ sin\theta = n\lambda$$

where d is the lattice spacing, θ is the incident angle of the X-ray, n is any whole integer and λ is the wavelength of the X-rays. **Figure 2-1a** depicts the experimental setup while the **Figure 2-1b** illustrates the spatial relationship between the lattice spacing and scattering angle. Lab-based XRD measurements were performed on a MiniFlex 600 Rigaku unit.

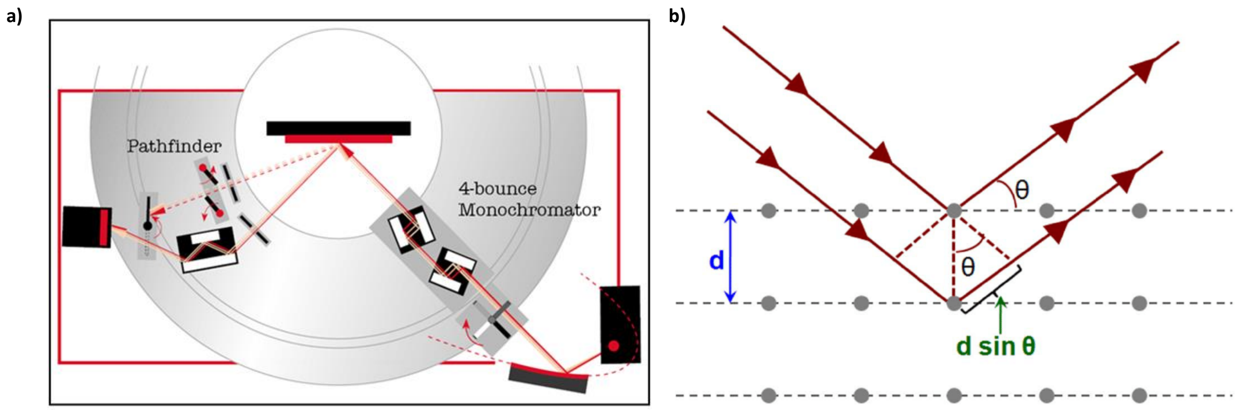

Figure 2- 1: a) Illustration of typical X-ray diffraction set up[94] and b) schematic of Bragg's Law.[95]

XRD will also be used to show the successful removal of silica template after HF etching. It is expected that the amorphous broad silica peak (2θ =~20^{o}) disappear after HF etching. While slight peaks at ~42^{o} and ~27^{o} should be present representing the (100) and (002) plane of graphite, respectively. The purpose is to provide evidence of a thin film of sulfur as appose to sulfur agglomerates, which is to be expected due to the high surface area and pore volume of the nitrogen doped porous carbon.

In addition to the benchtop XRD, high energy XRD (HEXRD) was performed at the Advanced Photon Source at Argonne National Laboratories. The synchrotron-sourced X-rays have significantly higher energy. Cu Kα-based lab XRD have a wavelength of 0.154 nm whereas the HEXRD from the 11 ID-C beamline has a much smaller wavelength of 0.01173 nm (high energy, hard X-rays). It should be noted that 2θ between the two different X-ray sources will be different and can be converted to a comparable basis based on Bragg's Law since *d*-spacing is purely dependent on the material. Additionally, the flux from a synchrotron source flux is also much higher, requiring a much lower sampling time. The key advantage of using a synchrotron-based radiation source is that it allows for *in operando* transmission-based sampling of the battery electrode in a coin-cell. This is because scattering cross section of elements typically decrease with increasing X-ray energy. However, though high energy X-rays are much more penetrative, the millimeters thick coin cell casing will still absorb/scatter a significant portion of the incident X-rays, rendering the useful scattered X-rays intensity too low. Therefore, a special coin cell setup is used to ensure X-ray only interact with the sample of interest plus as little of background material as possible. Specifically, **Figure 2-2a** illustrate the special *in operando* coin cell design. The stainless-steel components of the cell are hole-bored to allow for X-ray passage. The hole sizes are about 2 mm in diameter. As the cells are air sensitive and the electrolyte are relatively volatile, the cell must be near-hermetically sealed. To achieve at decent seal of the cell, Kapton-tape is typically employed on each side of the caps. That is, for each cap (top and bottom) there are two layers of Kapton-tape (from inside and from outside) sealing the cells (as shown in Figure 2-2a). The beam first passes through two layers of Kapton polymer on the bottom cap (background scattering), Li metal (background scattering), Celgard based separator (background scattering), electrode containing sample of interest and finally another two layers of Kapton polymer on the top cap before the beam exiting the coin cell. A digital image of the experimental setup can be found in **Figure 2-2b**.

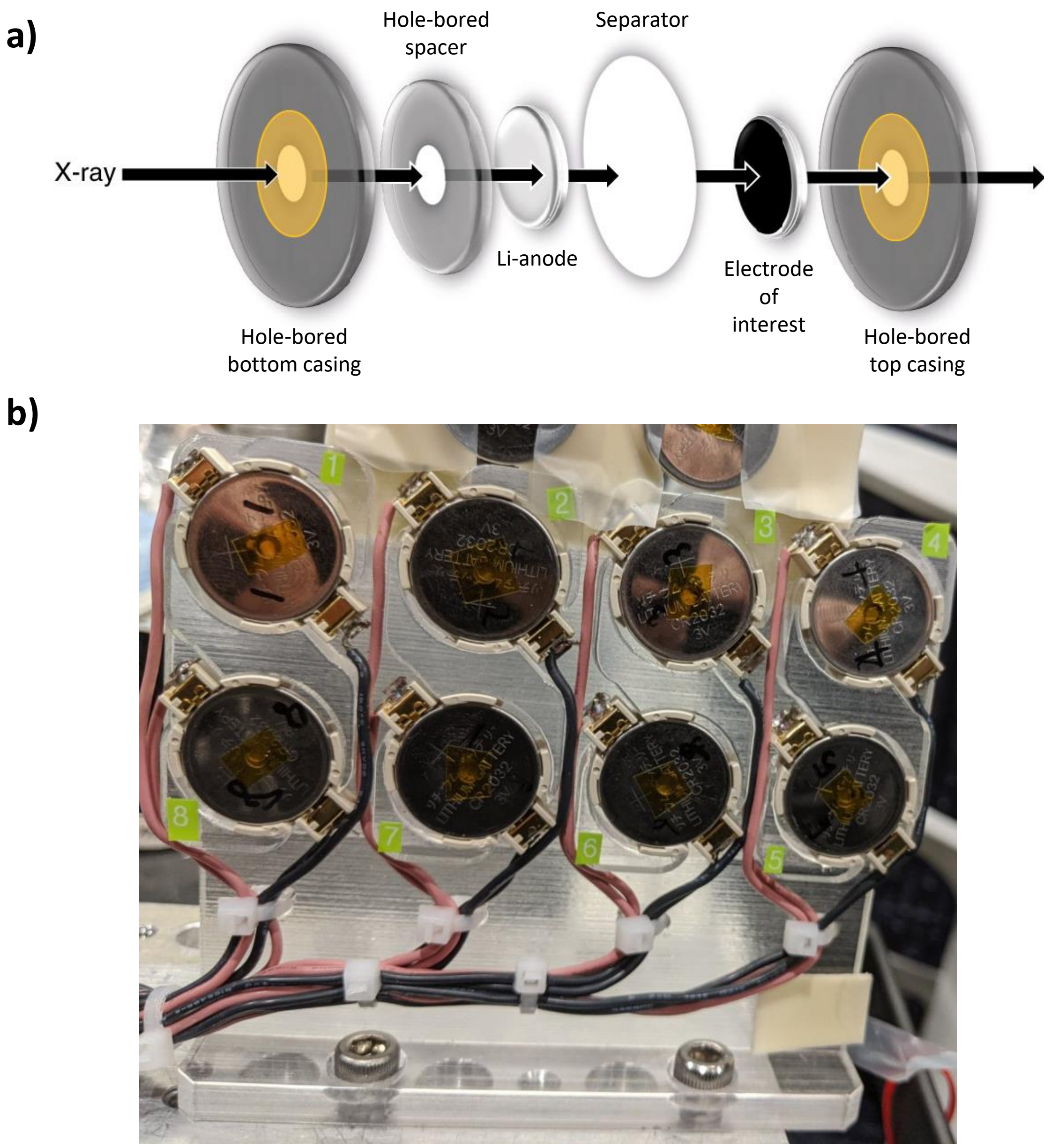

Figure 2- 2: a) Schematic of coin cell used for operando X-ray diffraction studies and not to scale, Copyright © 2019, Springer Nature[96] and b) digital picture of experimental setup with the backside of the coin cell visible where the X-rays will leave the sample.

2.4 Raman spectroscopy

Raman spectroscopy is an inelastic scattering technique where the scattered photons have different kinetics energies than the incident photons. This difference in kinetic energy yields a change in wavelength and is known as Raman scattering, which can provide important information on the functional groups of the material of question. In contrast, for some absorption-based spectroscopy, the emitted electromagnetic waves from the samples after interaction are not measured. This means that the only measured value is the total absorbed intensity, which is a sum of both elastically and inelastically scattered radiation. Raman spectroscopy specifically differentiates and measures the inelastically scattering radiation, which amounts to a very small portion of the signal. This technique is considered complementary to an absorption-based spectroscopy (such as FTIR) because it measures the polarizability of bonds rather than the dipole moment. As such, bonds with symmetrical structures such as alkane, alkene, etc. are more easily detected by Raman scattering than FTIR. Additionally, in contrast to FTIR, Raman spectroscopy experiments typically only probes the samples with a single wavelength laser and the corresponding detector scans different wavelength of inelastically scattering light. It should be noted that more sophisticated Raman spectrometers can tune the incident laser in a continuous manner yielding, a full three-dimensional plot of incident wavelength, emitted wavelength and emitted photon intensity. In this thesis, all Raman spectroscopy was only tested with a 785 nm laser to probe the chemical species present in sulfur-based electrode over the course of cycling.

2.5 Thermogravimetric analysis

Thermogravimetric analysis (TGA) is a technique where the weight change of a sample is measured as a function of temperature. Samples can also be exposed to different atmospheres as they are being heated during TGA. For example, heating carbon in nitrogen gas does not result in any weight loss even at 900 Celsius but once the atmosphere is changed to air, carbon is readily oxidized into carbon dioxide. A typical TGA measures the sample weight with a precision balance while purging the heated region with the desired type of gas. The heating is done in a small furnace and the temperature is precisely measured with a temperature resistance probe in close vicinity to the sample holder. The sample holder is usually made up of an inert heat resistant material such as platinum and alumina. A platinum sample holder is used in this research study.

The main purpose of TGA in this work is to determine the exact sulfur amount in the porous carbon/sulfur composite. Since sulfur boils at ~444 ^{o}C, a sharp decline in mass is to be expected near this temperature. If the atmosphere was chosen to be nitrogen, all the sulfur would vaporize leaving behind the porous carbon when this temperature is reached. The mass changed measured by the TGA will determine the accurate composition of the porous carbon/sulfur composite. This is imperative to obtain an accurate estimate of specific capacity. TGA was performed in this thesis on a TA instrument Q500.

2.6 X-ray photoelectron spectroscopy

X-ray photoelectron spectroscopy (XPS) is a method that provides information of the electronic structure of atoms and ionization energy of certain electrons of those elements. The sample is bombarded by X-rays and the resulting electrons ejected are captured by detectors. The basic concept XPS revolves around the conservation of energy. Since the wavelength of the X-ray is known prior to its interaction with the sample, the energy entering the system is known. Upon interacting with the atoms of the sample, electrons will be ejected from the sample with a certain amount of kinetic energy through the photoelectric effect. A simple energy balance determines how much energy is absorbed by the atom. This absorbed energy is called the binding energy or the ionization energy of the atom. This provides valuable information of the orbitals from which these electrons are emitted and the nature of the chemical bonds. Furthermore, because different electron shells require drastically different ionization energies, electron configuration of the sample can be found and hence a fingerprint for the atom in the sample. XPS is also surface sensitive and cannot penetrate more than a few nanometers of the sample. The key disadvantage of XPS it the requirement of a vacuum or a partial vacuum, which limits some of its application.

XPS will be used in this thesis to quantify the degree and type of nitrogen doping in our carbon-based sulfur hosts in Chapter 3 and 4. The three type of nitrogen doping should be pyridinic, pyrrolic, and graphitic. Furthermore, XPS will be used to identify the presence of Na species on the surface of the Li anode during oxidation of a composite Li_2S and Na_2S cathode presented in Chapter 6.

2.7 X-ray Absorption Spectroscopy

X-ray absorption spectroscopy (XAS) where the samples are bombarded by X-rays at different energies. When the X-ray energy reaches the correct energy level to excite the electrons of a given atom, an X-ray absorption phenomenon would occur. The energy level at which absorption occurs are known as the absorption edges. The term “edge” implies a sudden and sharp rise in absorbed energy which is due to minimal energy required to excite the electron of the orbital structures of the given atoms. Electrons at different orbital of the atom have different terminology with respect to their absorption edges. Specifically, the K-edge refers to the energy required to excite the core 1s orbital electrons (principal quantum number n=1). While not measured in this thesis, the $L_{1,}$ L_2 and L_3 –edges, more common to transition metals, refers to the energy required to excite from the 2s, $2p_{1/2}$ and $2p_{3/2}$ respectively (n=2) and M-edge refers to the electrons in n=3. In the vicinity of each edge are three main areas of interest, pre-edge, rising-edge and extended X-ray absorption fine structure (EXAFS). EXAFS measures the backscattering radiation of neighboring atoms. EXAFS was not performed in this thesis. The pre-edge, rising-edge and a few EV post-edge constitute what is known as the X-ray absorption near-edge spectroscopy (XANES) technique. This technique provides information about the oxidation and some information on the bonding environment and will be used in this thesis. Together, XANES and EXAFS are colloquially known as X-ray absorption fine structure (XAFS).

In terms of XANES, before the K-edge, there exist a pre-edges which occurs because there is a finite energy required to excite the core 1s electron to certain orbitals before to full vacuum. This gives rise to slightly convoluted edge rise. After the edge-step, the continued absorption is due to the interaction between the atom of interest and the neighboring atoms (bonding environment) *via* backscattering. This experiment is usually performed at synchrotron-based facilities due to the large range of X-ray radiation wavelength required to be swept while maintaining high photon intensity. However, benchtop systems are beginning to appear on the market. For this thesis, XAS was performed at beamline 9-bending magnet (BM) at the Advanced Photon Source (APS) at Argonne National Laboratory (ANL). BM beamlines operate by utilizing the photon release from the electron changing trajectory to complete each incremental turn inside the storage ring, this photon release is uncontrolled and yields a distribution of wavelengths. Broadband photons from synchrotrons are usually selected/filtered to specific wavelengths with a crystalline monochromator. At 9 BM, Si (111) and Si (220) monochromator are used. Mainly the S K-edge and P K-edge were investigated in this thesis. S K-edge position was calibrated with a $Na_2S_2O_3$ and the P K-edge position was calibrated with P_2O_5.

2.8 Potentiostatic Electrochemical Impedance Spectroscopy

Potentiostatic electrochemical impedance spectroscopy (EIS) is a very useful technique in the field of electrochemical engineering. It can provide insight into the mechanism of an electrochemical cell. EIS operates by treating the cell as a circuit of capacitors and resistors, the configuration of which is decided by the user. By applying an AC voltage signal at different frequencies over a pre-set voltage range a corresponding alternating current (AC) can be obtained. The dependence of the impedance of an AC circuit on the frequency can be used to fit a proposed electric circuit model. In the case of lithium sulfur battery the circuit below has been used.[97] Re is the ohmic loss from the electrolyte resistance, R_{int}/CPE_{int} is the resistance between the conductive interface of sulfur and any conductive material, R_{ct}/CPE_{dl} is the charge transfer resistance interpreted as the charge transfer process at the interface between the electron conductor and electrolyte/electrochemical reaction kinetics, and CPE_{diff} is the lithium ion diffusion resistance.[97-99] Through fitting the model (impedance versus frequency function) to the data set obtained from experiments a value for each circuit element can be obtained.

It should be noted that the interpretation and subsequent allocations of the mid frequency and high frequency semicircle on the Nyquist plot are often debated. Since the time constants for the physical transport properties between the electron conduction (R_s) and diffusion CPE_{diff} are very different, these physical phenomena are widely and confidently allocated to high frequency intercept and low frequency features (respectively). However, in the mid-high frequency regime, the time constant between different physical phenomena can become convoluted and highly dependent on the nature of the system. In the case of LSB, the allocation of R_{int} and R_{ct} have been used for high and mid frequency respectively and *vice versa* throughout literature. To this end we would like to first clarify that there are indeed experimental supported way to allocate the R_{int} and

R_{ct} for LSB. Work by Deng *et al* have shown that when varying temperature, only the mid frequency semi-circle is changed.[97] Compared to the contact resistance, that is the conduction of electron between conductive and non-conductive surfaces, a chemical reaction is expected to be more susceptible to temperature variations. This provide strong evidence that the mid frequency semi-circle is highly correlated to charge transfer (reaction rates) and the high frequency semi-circle is correlated to interfacial resistances.

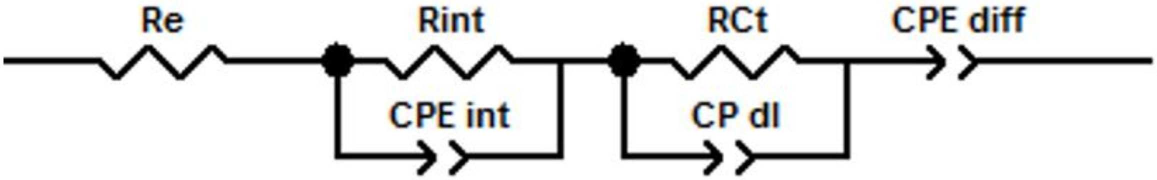

Figure 2- 3: Equivalent Circuit used for EIS

In the context of this thesis, EIS measurements will be used to characterize the cell impedance over the course of cycling. **Figure 3** depicts the equivalent circuit that will be used. Typically, experiments are run *operando* where the cell is cycled galvanostatically with intermittent EIS spectrums sampled at different states of charge/discharge. Spectra were then fitted using the Zfit function developed by Jean-Luc Dellis, implemented in Matlab. Zfit calls the 'fminsearch' function of MATLAB with heavy reliance on the quality of initial guess. Initial guesses were based on the raw Nyquist plots where the size of the semi-circle and their intercepts. The distortion of the semi-circle either towards the Z_{im} (more capacitive-like) or Z_{re} (more inductor-like) were used to provide initial guesses for "n". The admittance term, "Y" can then be estimated based on features (frequency position of impedance increase) of the Bode plots. The constant phase elements (CPE) were fitted using the following equation.

Equation 9

$$\mathbf{Z_{CPE}} = \frac{\mathbf{1}}{Y_o \boldsymbol{\omega}^{\mathrm{n}}} e^{-\frac{\pi}{2} n i}$$

Where Z_{CPE} is the constant phase element impedance value, Y_o is the admittance term, ω is the frequency, n is a constant term that is frequency independent that changes how capacitive or resistive the CPE is. i is the imaginary unit.

2.9 Galvanostatic Discharge

Batteries were evaluated with a coin cell. This technique entails a constant current discharge of the battery cells, followed by a constant current charge. The number of electrons transferred are counted from the start to the end of the cycle. The cycle ends when the voltage reaches a specific target voltage set by the user. In the case of LSB, typically fresh cells are first charged to 2.8 V vs Li^+ /Li followed by discharge to 1.9 V vs Li^+ /Li with a two-minute rest between charge and discharge. The current of discharge/charge is called the C-rate and is defined as the reciprocal of the discharge/charge time with units: $hour^{-1}$. One important note is that the discharge time can be based on many different factors in the battery. Therefore, the discharge time can vary greatly between battery technologies. Due to this variation, the convention used in most LSB research studies is to base the C-rate on the theoretical discharge time of the active material. For example, theoretically, one gram of sulfur in a battery at a current of 1675 mA g^{-1} would be fully discharged in one hour, assuming a completely theoretical (100% efficient) use of sulfur. Therefore 1675 mA g^{-1} would be called 1 C, an estimated 30-minute discharge (1675x2 mA g^{-1}) would be 2 C and a 10 hour discharge (1675/10 mA g^{-1}) would be 0.1 C. However, since the real specific capacity obtained from these cells are typically much lower than theoretical, the real discharge time are usually much lower. In the case of 1 C, it is predicted that discharge time should be 1 hour, but it is common for the real observed discharge/charge times to be around 36 minutes due to a much lower deliverable specific capacity (~1000 mAh g^{-1}). Galvanostatic cycling will be used to emulate real operation of the LSB in attempt to evaluate its cycle life performance.

Rate performance evaluation is done by ramping the C rates from an initially low rate (e.g. 0.1C) to higher rates (e.g. 5C). This is followed by recovery to the initial slow rate to show reversibility. This test will be used to determine the performance of the cell at different current densities, which again emulates real operation.

2.10 Shuttle current measurement

The shuttle current will be measured by holding the cell Potentiostatic at 2.3V versus Li^+ /Li and measuring the corresponding current response. This technique was first implemented by Moy *et al*[100] and its versatility was demonstrated in our publication.[46] The shuttle current is an attempt for the researcher to quantify and measure the rate of PS mass transfer out of the cathode and to the anode. When the PS species diffuse out of the cathode and reaches the anode, they will be reduced on the surface of lithium. As this occurs, a concentration gradient is generated from the anode to the cathode of the lower oxidation state PS and results in its diffusion back from the anode to the cathode. If a charging current (cathode receiving electron) is applied to the cell, then these lower oxidation state PS will be oxidized back to the its higher oxidation state counterparts. In the case of a potentiostatic experiment, the charging current can be described as the exact current or rate of which PS is reduced on the anode surface. This is possible only for higher order PS species i.e. S_8^{2-} and S_6^{2-} owing to the soluble nature of the reduction products of both the S_8^{2-} and S_6^{2-} species. CR 2016 type coin cells will be used for testing.

Chapter 3: Hollow porous carbon for stable lithium sulfur battery at relaxed testing conditions

This chapter is reprinted in adopted form with permission from Advanced Functional Materials:

M. Li, Y. Zhang, X. Wang, W. Ahn, G. Jiang, K. Feng, G. Lui, Z. Chen, Gas Pickering emulsion templated hollow carbon for high rate performance lithium sulfur batteries, Advanced Functional Materials, 2016, 26, 8408-8417, Copyright Wiley-VCH, 2016

3. 1. Introduction

To enable strict cycling conditions LSB, first a baseline material must be identified. This material needs to at the very least, outperform the normal carbon-black/sulfur composites. Cycling of sulfur cathode with commercially available carbon black typically yield very poor cycle stability, specific capacity and Coulombic efficiency. In fact, cycling a lithium sulfur battery at relaxed conditions is still non-trivial. The soluble nature of polysulfide is still problematic if certain[101] materials are not used. In this chapter, we discuss the use of a combined three-pronged technique to address the polysulfide shuttle effect. Firstly, N-doped carbon was used as the main host. N-doping can generate a dipole on the surface of carbon material. This dipole enhances polysulfide sorption characteristics of the N-doped carbon.[37,102] Secondly, the carbon is porous with high surface area and pore volume allowing for high contact with sulfur (electrically insulating). Furthermore, the porous structure creates tortuosity that slows the diffusion of polysulfide out of the cathode particles. Up to this point, the material design focusses very much on a chemisorption- and physical confinement-based approach to limit the escape of polysulfide, which has been also been established by other groups[103,104] including ours.[105] The key contribution here is that the porous carbon is arranged in a hollow structure. The impact of hollow carbon and its mechanism is the key contribution of this chapter.

Throughout the many fields of science, hollow structured nanomaterials have proven to be quite useful. The advantages of a hollow morphology stem from its unique implications in mass transfer characteristics such as physical separation of the core from the bulk phase.[106-108] Recognizing these benefits, researchers have developed innovative application in fields such as drug deliver,[109,110] waste water treatment,[111,112] among many others. One particularly interesting application of hollow morphologies, is in energy storage,[113,114] specifically, the field of lithium sulfur batteries. While LSB's stability and energy density is crucial, a high rate performance should be considered to be equally important and put under more scrutiny in the scientific community. In the case of electric vehicles (EV), the rate capability of the battery can influence the recharge time, acceleration and regenerative braking efficiency. All these parameters directly affect the final user experience of the vehicle and can cause serious damage to the reputation of EVs if poorly implemented. Often researchers have achieved LSB with impressive cycle durability, coulombic efficiency and capacity, but do not fare well when subjected to higher rate performance tests. Indeed, a complex pore network will limit PS diffusion and provide enhanced durability, but the very same tortuous diffusion pathway out of the cathode will inevitably increase lithium ion diffusion resistance. When combined with the known electrolyte viscosity/resistance increase upon PS dissolution,[115-117] it is understandable as to why the rate performance is poor. Recent research into the rate performance of LIS revolves around providing efficient lithium ion and electron mass transfer pathways[118-121] or additional battery components such as an interlayer to provide additional surface area for faster PS reduction.[122] Interestingly, hollow structures which have been previously used to successfully address the stability problems of LIS, commonly demonstrates excellent rate performances.[36,123-126] The distinct difference between hollow porous structures and regular porous carbon lies in the separation of the core electrolyte from the bulk electrolyte phases. The shell can act as a physical barrier to encapsulate PS, limiting dissolution of active sulfur material into the bulk electrolyte. More importantly, the hollow structures can serve as an PS reservoir[127] to redirect some PS diffusion inwards. This mitigate the effects of the viscosity increase from PS dissolution. Accordingly, early work in hollow structures for LSB have demonstrated some of the highest rate performance of its time.[36] In terms of LSB operated at strict testing conditions (high loading and low electrolyte content), carbon structures with macro porosities are crucial.

Practical application of hollow structures is limited due to relatively complex synthesis procedures. Most hollow carbon structures requires the use of either chemical surfactants[124,128,129] with two separate liquid phases[130,131] or hard templates,[36,123] entailing complex and expensive synthesis processes. One solution can be the use of self-removing templates such as gas bubbles which requires no additional core template removal step. Regardless of the method used to template the core, to obtain a hollow structure with also a mesoporous shell requires the careful tuning of another set of templates in addition to the core template. We look to solve this problem by taking advantage of the nanoparticle positioning in a Pickering emulsion (PE). First discovered by S. Pickering in 1907,[132] a PE is a unique type of emulsion system that is stabilized not by surfactants, but by particles.[133-139] The stabilized emulsion droplet is therefore composed of a multi-layer nanoparticle shell of which, we conveniently used as pore templates for the shell.

In this chapter, to the best of our knowledge we report for the first time the design and development of a CO_2 PE templated micron sized hollow nitrogen doped porous carbon for high rate performance lithium sulfur battery. This novel synthesis technique demonstrates low material cost and facile synthesis compared to other methodologies. The hollow morphology is achieved by first obtaining a CO_2 in water PE and then utilizing the CO_2 bubbles as a template for the hollow core through polymerization of melamine. Conveniently, no pre-made CO_2 emulsion solution is required. By polymerizing the carbon precursor around the nanoparticles stabilized emulsion, a porous shell can be obtained. This procedure effectively unites the normally separate core templating and shell templating process, into one facile step. Through combination of the hollow structure, and nitrogen doping, superior rate performance is obtained.

3.2. Experimental method

3.2.1. Material synthesis:

A typical synthesis procedures is a modification and improvement upon that of previously published work.[140] In short, melamine (12.6 g) was reacted with 37% formaldehyde solution (20 ml) at 85^{o}C at pH 9.5 (adjusted by 2M Na_2CO_3). Once the solution turned from white (MF dispersion) to clear (MF prepolymer solution), the solution was stirred at 1200 RPM for 15 additional minutes. To follow, the solution was cooled to 40^{o}C in ambient condition (~15 minutes). A 5 wt% Ludox AS 40 aqueous solution (120 g) was added into the solution and continued to be stirred at the same RPM for 20 minutes. 2M HCl was then added into the solution until the desired pH was reached and continued to be stirred for 15 minutes, In this step, the reaction between HCl and Na_2CO_3 generates CO_2, which are then we believed to be emulsified by silica nanoparticles. Afterwards, agitation was halted, and the solution was allowed to polymerize under stagnant conditions at 40^{o}C for 4 hours. The spherical hollow morphology was strongly dependent on the RPM and polymerization pH. To obtain the hollow morphology the RPM used throughout the synthesis was 1200 RPM and the polymerization pH of 5.5 was used. The reaction was conducted with a cylindrical ~2 inch Teflon coated metallic stir bar in a 500ml beaker covered by a watch glass. Afterwards the polymer/silica composite was decanted and dried in an oven at 60^{o}C for 24 hours followed by an 180^{o}C heat treatment for 24 hours. The obtained white powder was then carbonized at 900^{o}C for 2 hours with a 5^{o}C/min ramp rate under argon gas. The resulting powder was washed with an 8M NaOH solution at 80 ^{o}C for 2 days and rinsed with water. After filtering and drying, PEHPC was obtained. pH was measured with a Mettler Toledo S20 SevenEasy pH meter. The sample without silica was synthesized under the same exact conditions except the amount of 2M HCl was modified to compensate for the lack of basic Ludox additive, still reaching an endpoint of pH 5.5.

PEHPC and sulfur composite was synthesized by mortaring together PEHPC and sulfur at a mass ratio of 30:70. The mixture was then transferred into a sealed, argon filled Teflon lined autoclave and heated to 155 ^{o}C for 12 hours. The same procedure was done to synthesize the Ketjen black 600 JD and sulfur composite. All chemicals were purchased from Sigma Aldrich.

The blue balloon inflation experiment was performed by first adding 2M Na_2CO_3 (0.5 ml) into a 150ml glass bottle filled with water (100 ml) to increase the pH to 9.5. To follow, a correct amount of 2M HCl was added into the basic solution until the pH dropped to 5.5 (pre-determined with a Mettler Toledo S20 SevenEasy pH meter). Specifically, the acid solution was kept in the balloon and then the balloon was attached to the bottle. The addition of the acid entail simply turning the balloon to an upright orientation and the 2M HCl filled inside poured into the glass container *via* gravity.

For the experiment with silica, the concentration of silica was kept at 3% (i.e. 7.5 g of 40% wt silica suspension), matching that of material synthesis conditions. It is important to note that the silica suspension is alkaline, therefore the amount of 2M HCl added was adjusted accordingly to ensure the same amount of CO_2 generation.

3.2.2. Physical characterization:

Thermogravimetric analysis (TGA, TA instrument Q500) was conducted under nitrogen atmosphere to confirm the accurate sulfur loading. The protocol entailed a heating rate of 5 °C min^{-1} from 25 to 600 °C and maintained at 600 °C for 2 hours. Nitrogen sorption (ASAP 2020 micromeritics) was used to retrieve data which was analyzed using Brunauer-Emmett-Teller (BET) theory to calculate and in return, characterize the pore size distribution, surface area and pore volume of PEHPC. A Zeiss Leo FESEM 1530 scanning electron microscopy (SEM) was used to characterize the morphology of the material. A JEOL 2010F transmission electron microscope was used to further characterize the morphology of PEHPC. X-ray diffraction (MiniFlex 600 Rigaku) experiments were performed to confirm removal of silica. X-ray photoelectron spectroscopy (XPS) was performed using a K-Alpha XPS spectrometer.

3.2.3. Electrochemical characterization:

A water-based slurry of 15% solid content was formed with the mass ratios of PEHPC/S: carbon nanotubes: sodium carboxymethyl cellulose as 85:5:10 respectively. The slurry was casted onto a carbon coated aluminum foil current collector (MTI) with a typical sulfur loading of 1.3 ± 0.2 mg_{sulfur} cm^{-2}. All electrodes were dried at 70°C for 4 hours and transferred into an argon filled glovebox (Labstar MB10 compact, mBraun) with water and oxygen levels both under 1 PPM. The electrochemical performances were evaluated using a 2016 type coin cell with a 1,3-dioxolane and dimethoxyethane electrolyte at a 1:1 ratio with 1M LiTFSI with 0.2M lithium nitrate (pre-blended by BASF. Electrochemical testing station purchased from Neware was used to perform all cycling tests. The electrolyte to sulfur ratio was maintained at 17 µl mg^{-1}_{sulfur} for both cycle life and rate performance tests. The testing conditions in this chapter are at the relaxed condition. The counter electrode used was a lithium metal chip (Linyi Gelon LIB Co., Ltd), while Celgard 2500 was used as the separator. The coin cells were cycled from 2.8V to 1.6V vs Li/Li$^+$ for rate performance test and 2.8V to 1.9V vs Li/Li$^+$ for cycle life performance to avoid decomposition of $LiNO_3$. Electrochemical impedance spectroscopy was performed on a Princeton VersaStat MC with frequency ranges from 100000 to 0.1 Hz with an amplitude of 50mV using the same 2016 type coin cells. The EIS circuit was fitted using the Zfiti function developed by Jean-Luc Dellis, implemented in Matlab. EIS cells were discharged at a constant current of 0.1C with EIS captures taken at once every 1200 seconds. Shuttle current measurement was performed in accordance to work done by Moy *et al*[100]. Briefly, the cells were first cycled 3 times (2.8V to 1.6V vs Li/Li$^+$) at C/20 and then charged to 2.8V. After leaving at open circuit voltage for 10 minutes, the cells were held at 2.3V and the corresponding current was monitored. This experiment was performed using a Princeton VersaStat MC

3.3. Result and discussion

3.3.1: Synthesis of nitrogen-doped hollow porous carbon

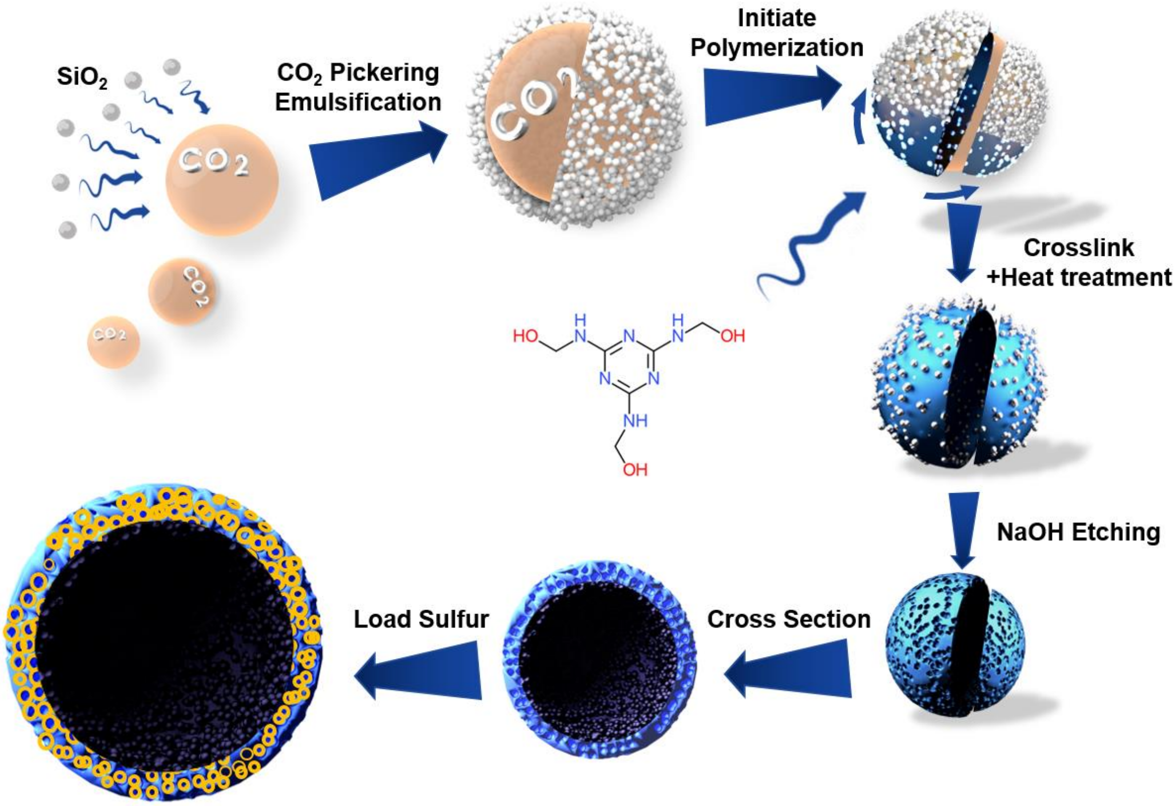

Figure 3- 1: Illustration of proposed synthesis mechanism. Briefly, HCl is added into a basic (Na_2CO_3) melamine formaldehyde prepolymer solution with silica dispersed homogenously. The first purpose of the HCl is to initiate the polymerization and crosslinking of melamine formaldehyde monomers. The second purpose is to generate CO_2 gas bubbles in situ inside the solution. At higher agitation rates, the silica nanoparticle diffuses to the surface of these CO_2 bubble to form a silica stabilized CO_2 Pickering emulsion in water. Subsequently, the melamine formaldehyde monomers begin to phase separate out of water and polymerize onto the silica covered CO_2 bubbles. After the monomer is crosslinked, the hollow morphology is casted and solidified. After carbonization and silica removal a nitrogen doped hollow carbon with a porous shell is obtained. Sulfur is the loaded into the shell of the porous carbon.

To synthesize the hollow carbon, Na_2CO_3 is added to increase the pH to react melamine with formaldehyde. Subsequently, nanoparticles (silica) are dispersed into the prepolymer solution prior to gas bubble generation, priming the system for PE formation. 2M HCl is then added to the solution to lower the pH, for first the generation of CO_2, and then the initiation of melamine formaldehyde (MF) polymerization. The proposed synthesis flow chart of the Pickering emulsion stabilized hollow porous carbon is presented in **Figure 3-1**. Once the pH is adjusted from 9.5 to 7, Na_2CO_3 reacts with HCl to an appreciable degree and generates CO_2 gas. The CO_2 gas bubbles are likely encapsulated by silica particles, forming a PE. When the pH is lowered to 5.5, the polymerization and crosslinking of MF begin to form a robust silica/MF composite shell around the CO_2 bubbles. Upon curing, the hollow morphology is casted. To further explore and elucidate the synthesis mechanism, **Figure 3-2a-c** presents an experiment where 2M HCl is added into a solution of Na_2CO_3 (without MF at pH 9.5) until the pH is lowered to 5.5 with a balloon covering the solution. Immediately, the reaction between HCl and Na_2CO_3 generates CO_2 and inflates the balloon. The degree of inflation provides an indication as to how much CO_2 is released from the solution and how much is emulsified. Aligning with our expectations, a significant difference is found if certain experimental conditions are adjusted. Specifically, three different scenarios are investigated: without silica i.e. no emulsifying agent (Figure 3-2a), with silica but no agitation (Figure 3-2b) and with silica in addition to rigorous agitation (Figure 3-2c). In the case without silica (Figure 3-2a), the produced CO_2 gas is captured by the blue balloon and inflates it. This is understandable as there are no emulsifying agents (silica) present to stabilize the CO_2 bubbles. One might suggest MF to be an important or even the dominant CO_2 emulsifying agent, implying the inflation of the balloon is causes by the absence of MF. If MF does indeed serve a more important role over silica in CO_2 emulsification, then the absence of silica should have little effect on the morphology. This is revealed not to be the case. Corroborating these observations, when the synthesis procedure is carried out without silica, the resulting SEM image of the morphology (**Figure 3-2d**) reveals no hollow morphology. Therefore, there exists a requirement of silica particles in the formation of hollow structure.

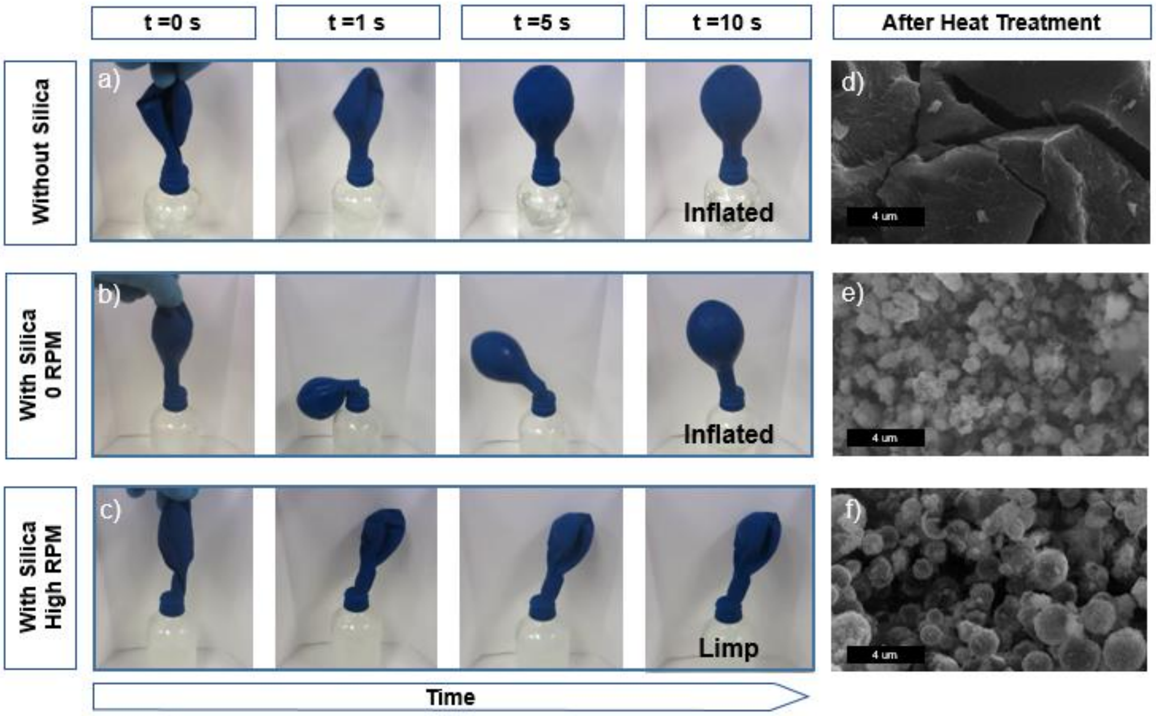

Figure 3- 2: Image of balloon inflated by generated CO_2 at different time steps after HCl addition a) without silica at high agitation rate; b) with silica at 0 RPM; c) with silica at high RPM; d) SEM image of morphology without silica template; e) with silica at low RPM; f) with silica at high RPM.

In Figure 3-2b, prior to HCl addition, silica is added into the Na_2CO_3 solution. After dispersing the silica, 2M HCl is added without agitation. The generated CO_2 once again inflates the blue balloon, indicating no CO_2 emulsification. In Figure 3-2c, the same experiment is performed, but this time with vigorous agitation while HCl is being added. The result is a limp blue balloon. The decreased inflation of the balloon indicates that the volume of CO_2 is compressed. Gas bubbles are at higher pressures than its bulk phase to balance the surface tension inherent to its spherical geometry. The contrast between Figure 2b and c is interesting and indicates that if the solution is not agitated, even the presence of nanoparticles (silica) cannot form CO_2 emulsions. This illustrates an important relationship between the encapsulation of CO_2 bubbles and the agitation rate, characteristic to bringing a system to a thermodynamically unstable state i.e. emulsion.[141-143]More importantly, this same relationship is found in the morphological results when applied to synthesis conditions. When the synthesis is carried out at low RPM (300RPM), almost no hollow spheres are found (**Figure 3-2e**), whereas at 1200 RPM, almost all MF/silica composites are in their hollow form (**Figure 3-2f**).

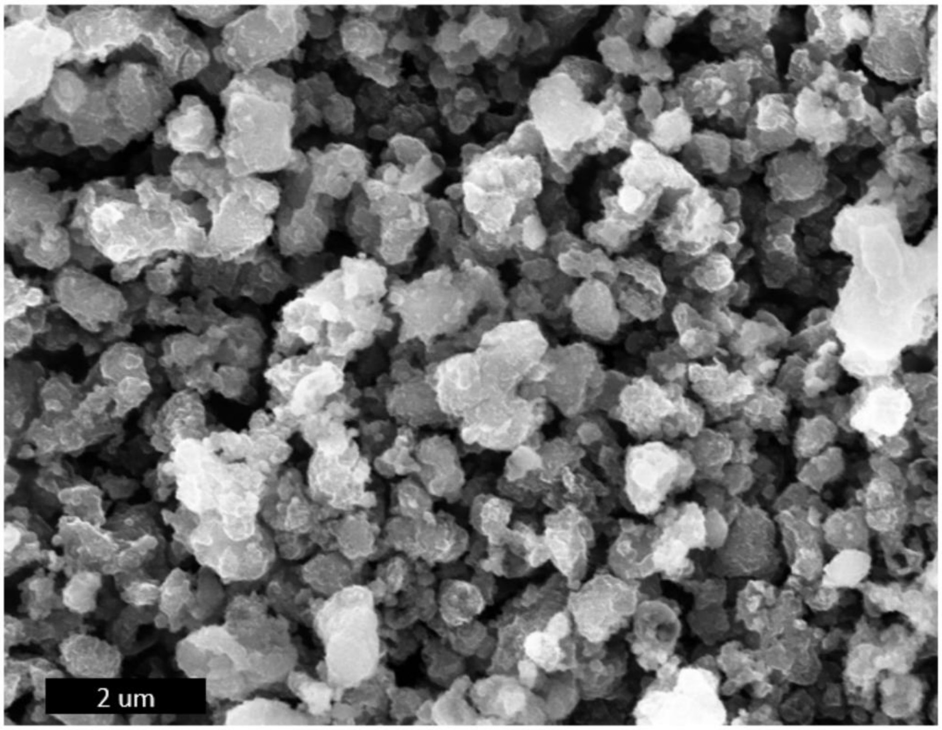

Figure 3- 3: Morphology with NaOH as base, i.e. without CO_2 generation

Additionally, NaOH is used to substitute Na_2CO_3 in synthesizing the MF prepolymer solution as another control experiment. This eliminates any possibility of CO_2 formation and should yield no hollow structure. Aligning with our theory, the result reveals no spherical morphology (**Figure 3-3**).

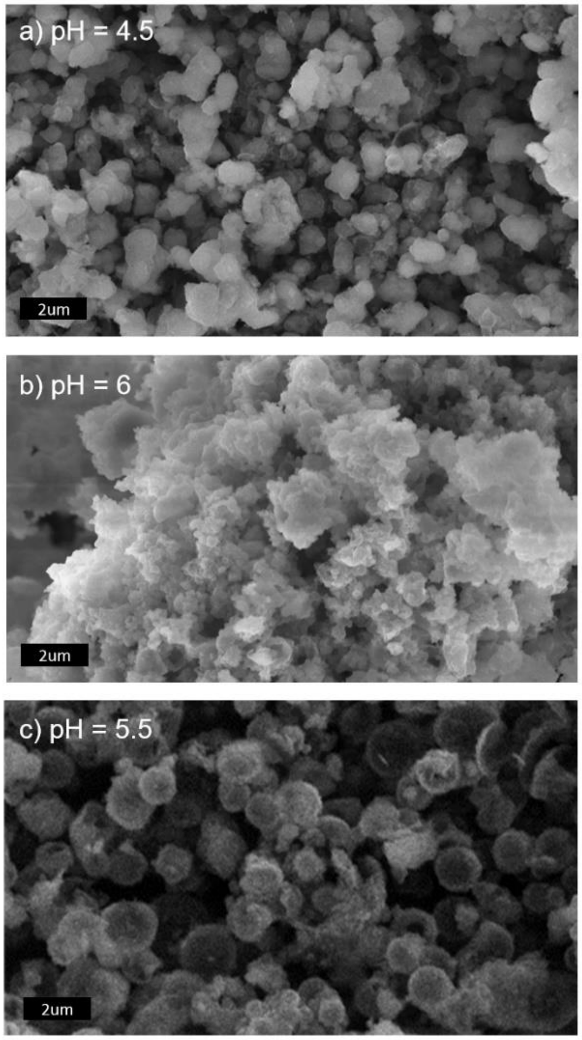

Figure 3- 4: SEM image of sample with synthesis carried out at a) pH 4.5, b) pH 6.5 and c) pH 5.5

The particle's morphology is also strongly dependent on the pH of the solution. When the pH value is held at 4.5 or 6.0 instead of 5.5, no hollow morphology is present, as seen in **Figure 3-4a-b**. CO_2 is widely known to be in equilibrium with carbonic acid when dissolved in water, [144] and the equilibrium shifts depending on the pH. If the pH is too low, the equilibrium will shift towards CO_2 and increase the rate of CO_2 generation. At a sufficiently low pH, the high rate of CO_2 generation can overcome the rate of emulsification, and result in the release of CO_2 into the atmosphere. Without CO_2 acting as the hollow core template, the resulting particles (Figure 3-4a) reveal no spherical morphology even at high RPM. On the other hand, if the pH is too high, the equilibrium will shift towards the carbonic acid. In this case, there are not enough CO_2 bubbles which allows the polymerization of MF to exceed that of CO_2 emulsification, resulting in formation of randomly seeded porous carbon particle without a hollow core. Again, the resulting SEM imaging of the morphology confirms no spherical morphology even at high RPM (Figure 3-4b). However, when the pH is kept at 5.5, in between 4.5 and 6, the resulting morphology reveals the desired spherical morphology (**Figure 3-4c**). Therefore, the pH can be used to effectively tune the rate of CO_2 release into the solution. From our experiments, perfect tuning can be defined as the pH at which the CO_2 release rate matches the rate of CO_2 emulsification.

These experiments show that CO_2, silica, correct pH tuning and a sufficiently high agitation rate are all required to form a hollow morphology. Furthermore, literatures have demonstrated that silica can form PEs.[133,138] It should also be noted that a gas/water emulsion will quickly coalescence or phase separate due to differences in density if left stagnant and will cause the CO_2 to lose its function as a hollow-structure template. Because of the relative instability of gas emulsion systems,[145-147]carbon precursors that do not adhere strongly to the nanoparticle stabilized gas emulsion droplets, but are merely adsorbed onto the surface, cannot form hollow carbon particles. This problem is circumvented in this work due to the polymerization of MF shortly after CO_2 emulsion formation. Not only can the prepolymer solution act as an emulsion co-stabilizer,[23] but once the pH is lowered past 7, MF begins to polymerize appreciably, and crosslink around each individual silica particle on the emulsion droplet. This forms a denser, mechanically robust MF/silica composite which consolidates the positioning and preserves the hollow morphology of the PE. Ultimately, this new synthesis methodology creates a MF/silica composite as the shell of a hollow particle. This brings forward another important role of silica. In addition to being an emulsion stabilizer, silica also conveniently acts as a hard template to form mesopores throughout the shell.

The benefits of this method lie in the use of gas bubbles as template for the hollow core. No prior preparation of a microbubble solution is required such as in Ref. 148 and no additional surfactants are required to facilitate the formation of this hollow morphology. This procedure is only a slight modification (change of reaction RPM and pH) of traditional hard templating porous carbon synthesis techniques, but effectively transforms a simple porous carbon particle into a porous carbon shell-hollow sphere. In this work, silica nanoparticles is selected as the CO_2 emulsion stabilizer due to its relatively low cost and commercial availability, but other nanoparticles can also be utilized depending on the application.149-151 The dual role of the nanoparticle in this system serves both as an emulsifying agent and a pore template. We believe this method can be carried over to many different combination of carbon source/pore template.

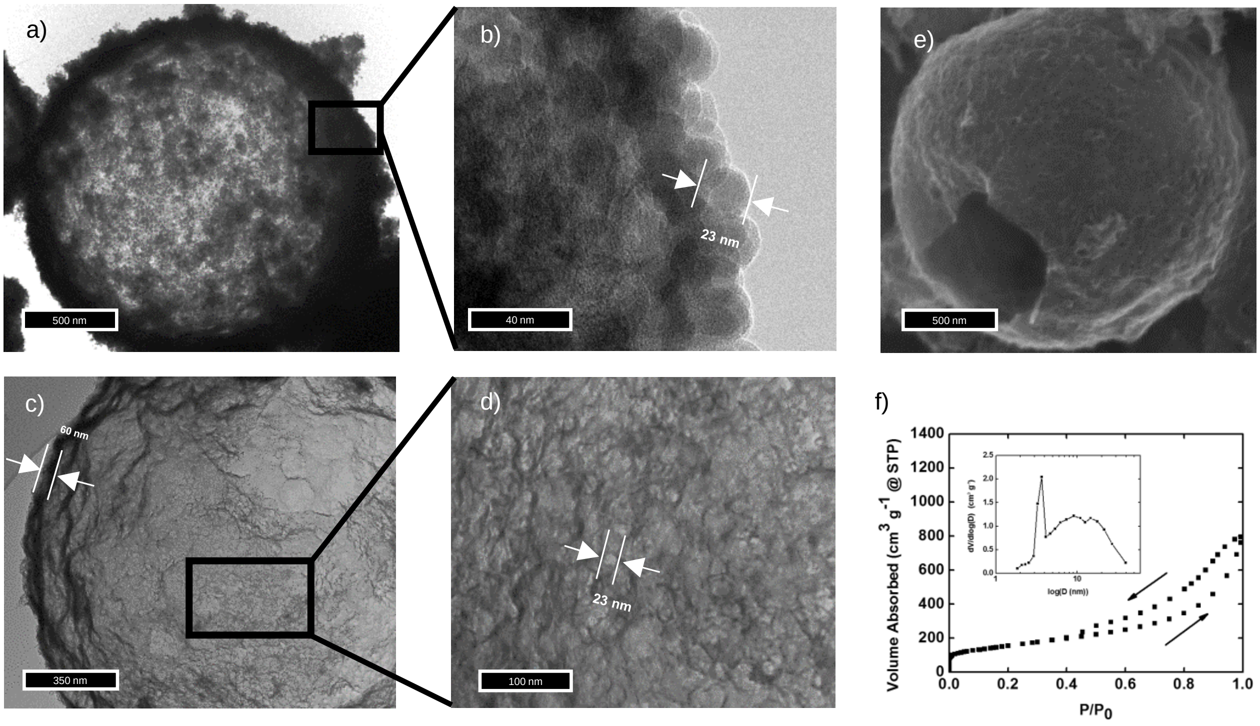

Figure 3- 5: a) TEM image of single PEHPC with silica; b) TEM image of shell of PEHPC indicating ~20 nm silica particle; c) TEM image of a single PEHPC revealing shell of ~60 nm d) TEM of shell of PEHPC revealing pores of ~20nm; e) SEM image of a single broken PEHPC revealing hollow core; f) Nitrogen sorption data and pore size distribution in inset, pore volume= 1.23 cm^3 g^{-1} and surface area= 550 m^{2}g^{-1}.

After carbonization, the resulting hollow morphology is studied under TEM, **Figure 3-5a** depicts a single hollow carbon sphere prior to silica removal. Higher magnification TEM (**Figure 3-5b**) at the edge of the particle reveals multiple layers of ~23 nm particles (silica) on the surface. This provides evidence that silica particles are on the surface of the gas bubble, confirming silica's role as an emulsifying agent for CO_2. After removal of silica, a ~60 nm thick porous shell remains. The pores on the shell are confirmed by **Figure 3-5c-d**, revealing pores sizes of ~23 nm which aligns with the size of the silica nanoparticle used. This confirms the high dispersion of silica on the surface of the CO_2 and throughout the MF composite and more importantly, confirms its function as a mesopores template. The hollow morphology is again shown through SEM imaging, **Figure 3-5e** depicts a single broken particle after silica removal, revealing a hollow core. The final material after silica etching will be referred to as Pickering emulsion hollow porous carbon (PEHPC). Nitrogen sorption experiment (**Figure 3-5f)** also confirms a broad peak at ~20 nm in the pore size distribution plot.

3.3.2. Physical and electrochemical characterization

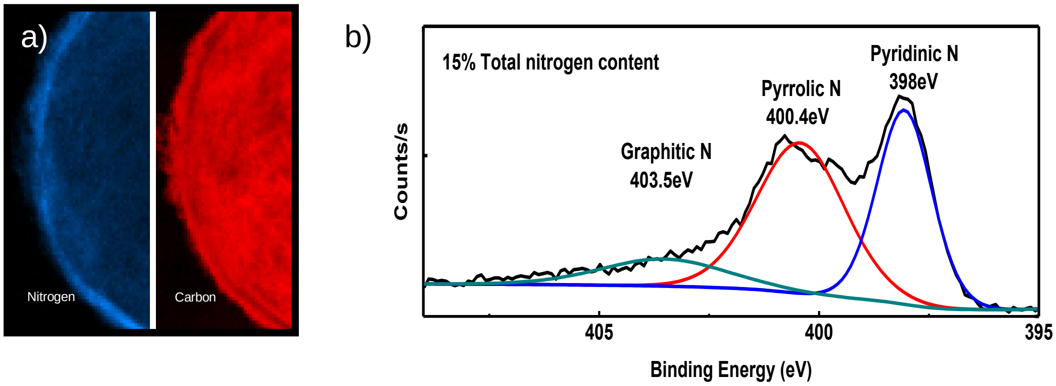

Figure 3- 6: a) EELS mapping of nitrogen and carbon; b) XPS binding energy spectrum of PEHPC.

Due to the use of melamine as carbon precursor, PEHPC possesses nitrogen doping. Electron energy loss spectroscopy (EELS) is employed to investigate distribution of nitrogen doping (**Figure 3-6a**). It is found that nitrogen is dispersed homogenously throughout the structure with very strong signals throughout. Finally, nitrogen doping in PEHPC is examined by XPS analysis (**Figure 3-6b**). The graphitic, pyridinic and pyrrolic form of nitrogen represents 12.5%, 39% and 48.5% of the total nitrogen content, respectively. It is important to note that the graphitic nitrogen has been shown through a few density function theory calculations [37,38,152,153] to possess the least amount of interaction with PS, while the pyridinic and pyrrolic have significantly higher affinity to adsorb PS *via* polar interactions. Therefore, to make the best use of nitrogen doping, the graphitic form should be minimized. Our material has the advantage of possessing a relatively low graphitic nitrogen content of 12.5% (relative to the other N-groups, while maintaining a high percentage of both pyrrolic and pyridinic nitrogen. The high nitrogen content of PEHPC (15 atomic %) is among some of the highest nitrogen doping content for hollow porous carbon structure.[129,154-161]

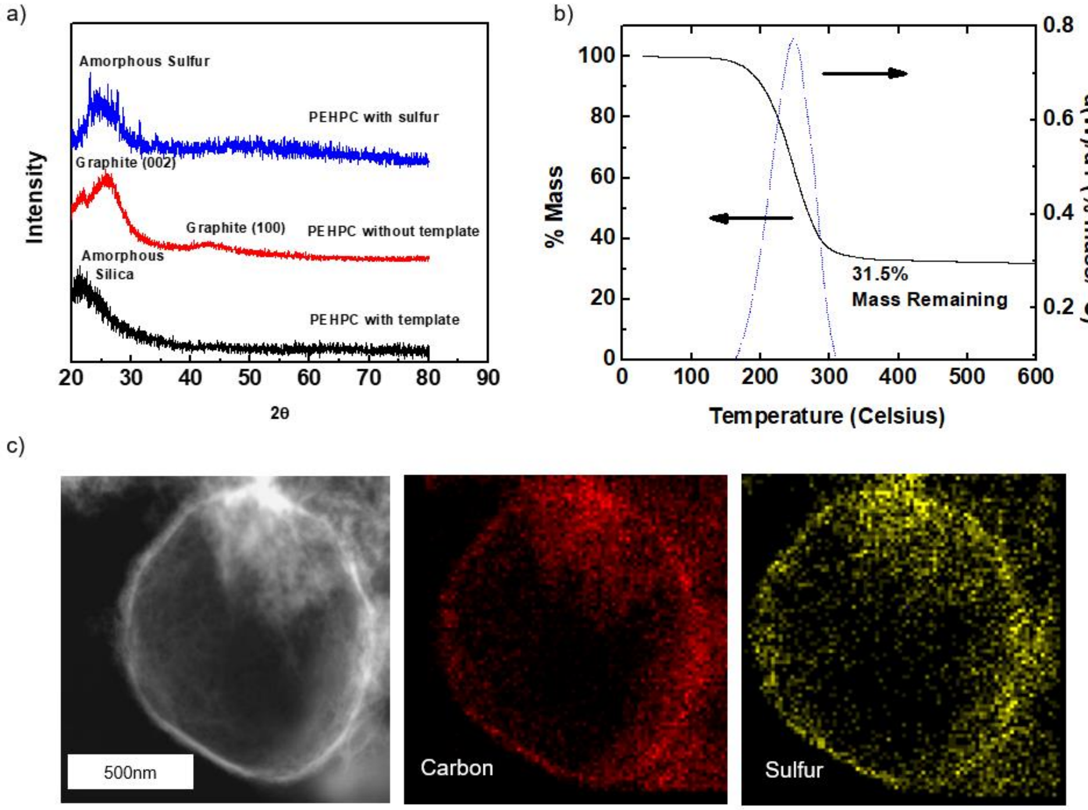

Figure 3- 7: a) X-ray diffraction spectrum of (from bottom to top) PEHPC with silica, PEHPEC without silica and PEHPC with sulfur loaded b) Thermogravimetric analysis of

PEHPC with ~70% sulfur loading. c) From left to right, STEM of PEHPC, energy dispersive spectroscopy mapping of carbon and sulfur of a broken PEHPC loaded with sulfur.

To test this material as a sulfur host, sulfur was loaded into PEHPC via the well-known melt-diffusion method,[162] where a mechanically blended mixture of sulfur and PEHPC is heated to 155^{o}C (where the viscosity of sulfur is the lowest). This allows for the diffusion or sulfur into the pore of PEHPC through capillary action. X-ray diffraction of PEHPC before and after HF etching is shown in **Figure 3-7a.** Interestingly, after sulfur loading, no sharp sulfur peaks are found which is indicative of small sized sulfur particles. Thermogravimetric analysis confirms that about 70 wt.% of the composite is sulfur (**Figure 3-7b**). Energy dispersive spectroscopy mapping (Figure 3-7c) reveals that the sulfur is deposited mostly on the rim of the particle with minor signals stemming from the core of PEHPC. This is desirable because if the PEHPC is over saturated with sulfur, the electrical connection between the carbon and sulfur will be compromised, rendering a portion of the sulfur material inactive.

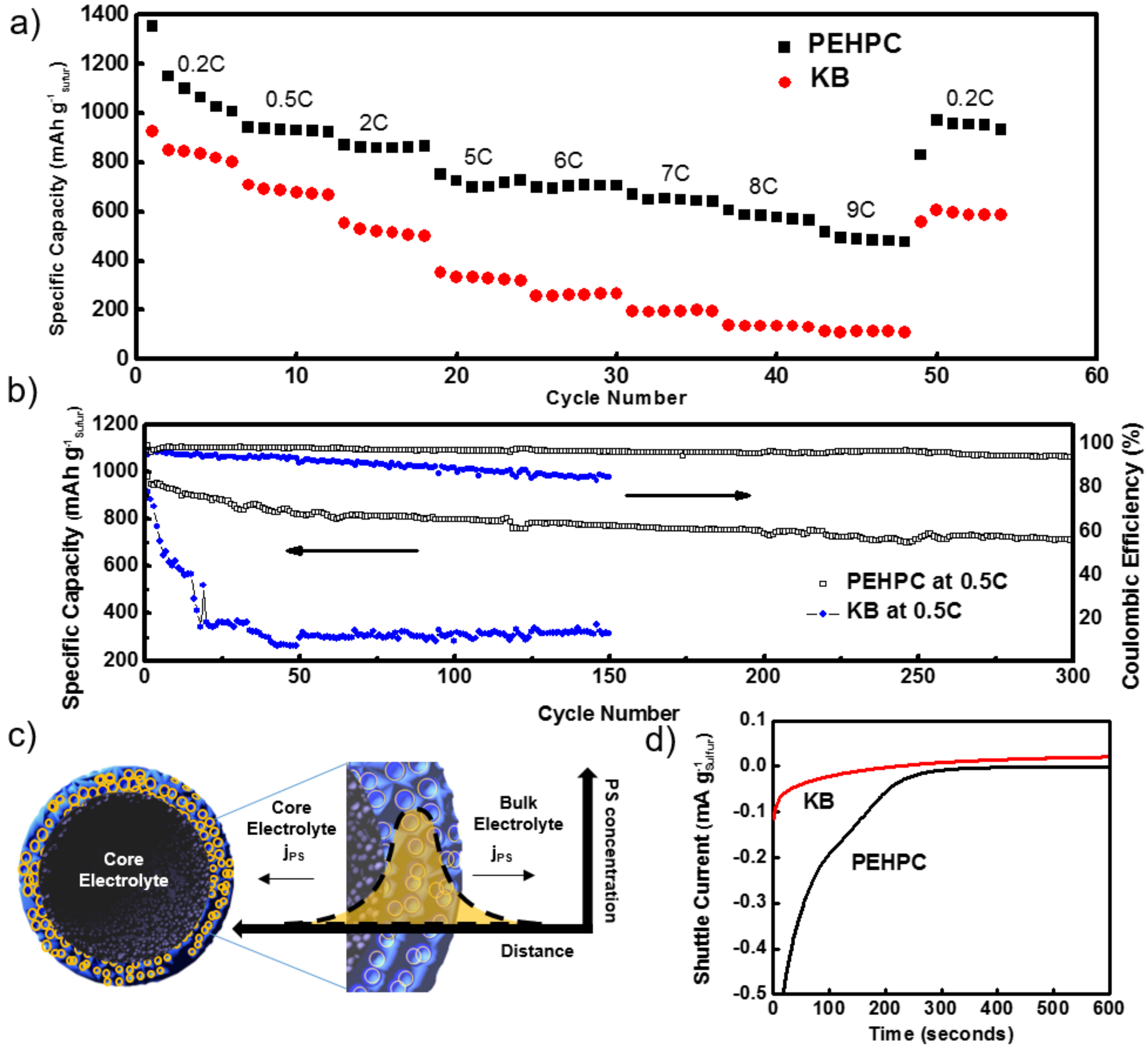

Figure 3- 8: Rate performance of a) PEHPC and KB; b) Cycling capacity and coulombic efficiency of PEHPC and KB at 0.5C; d) Illustration of PS diffusion mechanism of hollow structures; d) Time profile of the shuttle current of KB and PEHPC

PEHPC demonstrates impressive capabilities as a sulfur host for LIS. **Figure 3-8a** indicates that at high discharge rates of 7C and even up to 9C, PEHPC loaded with sulfur delivers a capacity of ~670 mAh g^{-1}_{s} and ~500 mAh g^{-1}_{s} respectively. In contrast, the KB electrode is found to deliver a significantly lower, 335 mAh g^{-1} at only a rate of 5C. At higher rates such as 9C, the KB electrode is only able to discharge 113 mAh g^{-1}. The impressive performance of PEHPC can be due to a combination of three properties of PEHPC. First, nitrogen doping had been previously speculated to possess catalytic properties towards the reduction of PS.[163] This can serve to lower the impedance in the cell, and allow for more reduction of polysulfide species. Secondly, owing to the micron sized nature of PEHPC, the interparticle spacing can allow for very efficient lithium ion mass transfer compared to smaller sized hollow carbon.[40] Thirdly, due to the hollow core, PS diffusion is initially directed inwards due to a concentration gradient. An inward PS flux obtains a portion of the PS and decreases the amount of PS diffusion into the bulk electrolyte. One commonly overlooked problem of LSB is the corresponding increase in viscosity due to increases in PS concentration. The increase in viscosity is highest during the end of the 1st plateau, when all solid $S_{8(s)}$ has been reduced to its soluble S_8^{2-}, S_6^{2-} and S_4^{2-} form.[98] At this time, the lithium ion transfer will be significantly retarded and will cause the cell to prematurely reach the cut-off voltage, resulting in very poor rate performances. At high discharge rates, the increase in Li^+ ion mass transfer resistance can drastically affect the ability of the cell to discharge. We believe in the case of PEHPC, some of the PS are redirected inwards, partially relieving the bulk electrolyte of PS and lowers the overall viscosity of the bulk electrolyte. The ability of PEHPC to discharge at 9C can have significant implication in the rate performance aspects of electric vehicles.

Additionally, PEHPC also exhibits exceptional cycle durability. Long galvanostatic cycling at 0.5 C (**Figure 3-8b**) reveals that PEHPC delivers 980 mAh g^{-1}_{sulfur} and continues to retain a capacity of 720 mAh g^{-1}_{sulfur} (73% retention) at the 300th cycle (0.088% capacity loss/cycle). This impressive cycle life is most likely due to the combined effect of the hollow structure in addition to the high nitrogen doping content (15 at%) of PEHPC, in alignment with previous studies.[164] Additionally, most of the nitrogen groups in PEHPC are found to be in the pyridinic and pyrrolic form. It has been theorized that the graphitic nitrogen can provide a permanent dipole on the carbon structure due to differences in electronegativity between N and C. However it has been shown that such dipole interactions with PS species are minimal when compared to the Lewis base-like characteristics of the lone pair in the pyridinic and pyrrolic nitrogen groups.[37,102] Hence the large amount of pyrrolic and pyridinic nitrogen sites throughout PEHPC can be seen as a bin, of which can adsorb/hold PS and ultimately retard any diffusion of PS away from each PEHPC particle. The advantage of using PEHPC as a sulfur host is evident when comparing against KB. The cycling result indicates an initial cycle of ~900 mAh g^{-1}_{sulfur} at 0.5C, lower than that of PEHPC and quickly decreases to 320 mAh g^{-1} (36% retention) at the 150th cycle, representing a severe capacity loss of 0.43%/cycle. Owing to the effects of $LiNO_3$, the coulombic efficiency of the KB electrode is still relatively high (>85%) over 150 cycles, indicating suppressed deposition of PS species on the lithium anode. However, the inability of the KB to locally retain PS can result in the redistribution of sulfur throughout the cathode. Once redistributed, the sulfur becomes electronically inaccessible and causes severe cycle degradation. Additionally, the Coulombic efficiency of PEHPC (93% at 300th cycle) is also significantly higher than that of KB (85% at 150th cycle). The higher coulombic efficiency further corroborates the fact that PEHPC is superior to KB in mitigating both the effects of the PS shuttle effect and in managing the redistribution of PS throughout the electrode.

We theorized that the observed rate performance and cycle durability is most likely due to the hollow structure. The distinct difference between porous carbon and hollow porous carbon lies in the separation of the electrolyte compartments. Electrolyte can be categorized into two types: the bulk electrolyte, the portion that is outside of the core and in between the PEHPC particles, while the core electrolyte is the portion that resides at the core of PEHPC as shown in **Figure 3-**

8c. The core electrolyte is an especially interesting feature of PEHPC and provides unique mass transfer dynamics. As PS molecules are generated in the shell, a corresponding concentration gradient (shown in orange) would be present both inwards and outwards. The outwards diffusion of PS will be obviously poor for PS retention, but the inwards diffusion will allow the void core to act as a PS concentration sink/PS reservoir. The inwards PS flux/diffusion works to deplete the PS in the porous shell, lowering its concentration. The shell with a now lowered outwards concentration gradient, generates a lowered outward flux (initially). Moreover, the PS in the core of any specific PEHPC particle can only be reduced/oxidized exclusively by that same PEHPC particle. Through the unique mass transfer mechanics of hollow structures and PS adsorption of nitrogen doping, PEHPC can achieve high rate performance and stable cycle life. To further investigate this phenomenon, measurement of the shuttle current (SC) is performed according to the work done by Moy *et al.*[100] The SC is a quantification of the amount of PS diffusion from the cathode to the anode. In short, the shuttle current can be obtained by first charging the cells to 2.8V, followed by holding the cell at a constant 2.3V, and then measuring the current response versus time. Initially, the current will be negative (discharging) because of the reduction of PS species that can thermodynamically be reduced at 2.3V. As time proceeds, the discharge current decreases due to depletion of all reducible species (at 2.3V) in the electrolyte and reaches zero. However, the current does not remain at zero because of the PS shuttle effect. Due to PS diffusion towards the anode, the lithium constantly short circuits/consumes PS species, resulting in the well-known self-discharge phenomenon and lowers the voltage of the cell.[165-167] In order to maintain the cell voltage at 2.3V, the current must change from negative (discharging) to positive (charging), oxidizing the lower order PS at the cathode to high order PS at a rate that matches the rate of PS diffusion away from the cathode/self-discharge. Therefore, the current time profile can be viewed as the real time result of the ongoing competition for PS mass between cathode reduction and PS self-discharge. When all reducible species has been reduced and the system has reached steady state, the corresponding steady state current matches exactly that of the rate of PS diffusion i.e. the shuttle current.[100] In the case of this work, the transient component of the SC time profile is more informative because it provides insight as to how exactly this steady state current is reached and sheds light on the PS mass transfer dynamics prior to consumption. **Figure 3-8d** reveals that at ~100 seconds, the transient component of PEHPC possesses a distinct decrease in the rate of change (inflection point) of the current. The inflection point indicates that some factor in the cell is suddenly providing PS for the cathode to discharge, slowing the onset of a positive/charging steady state current. This is intriguing, because in the case of a hollow morphology, the concentration profile in the core during SC measurement will also be time dependent. Initially, it will be lower than the shell (promoting an inward flux), but eventually, all PS in the shell will be depleted and the PS concentration in the core will be higher than the shell. We therefore attribute the inflection point to the reversal in PS flux resulting in PS diffusion from the core to the shell. The funneling of PS species from the core to the conductive shell allows for the cell to maintain a higher discharge current for an extended period. Once the core PS concentration is depleted, the current will then reach the steady state SC. One might argue that pores in KB can serve the same purpose, since the interparticle void space can function as PS mass sinks and should demonstrate the same SC time profile. This is experimentally shown to be not the case, because the KB SC time profile quickly reached steady state upon holding at 2.3V. This indicates a possible dependence of the shuttle current profile on the local void space size as oppose to the total magnitude of the void volume. The contrasting transient SC profile between PEHPC and KB provides interesting evidence of the beneficial effects of hollow morphologies while at the same time provide valuable insight into the mass transfer mechanism involved.

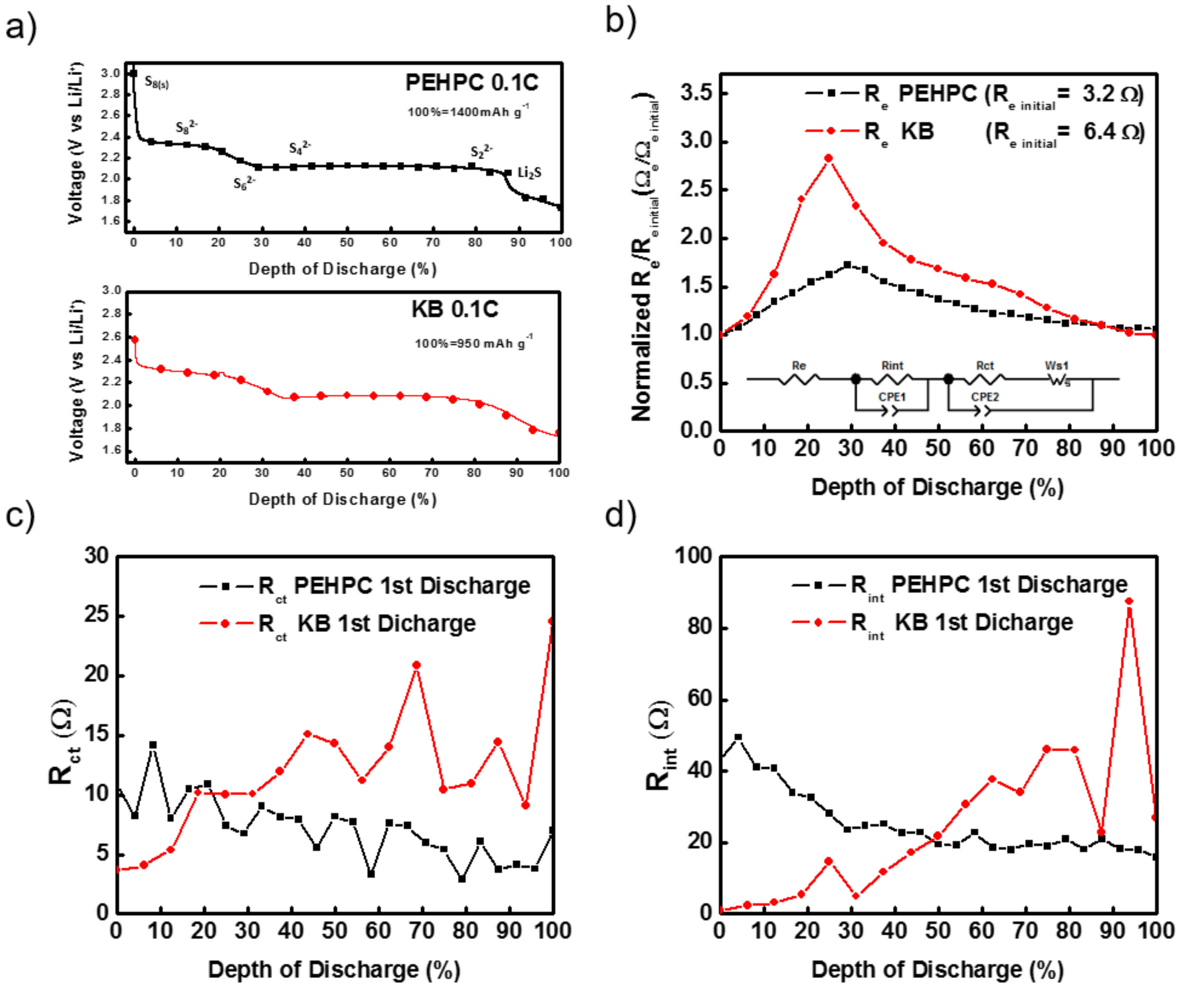

Figure 3- 9: a) First discharge voltage profile at 0.1C with squares indicating depth of discharge (DOD) at which EIS measurements were performed; b) R_e, c) R_{ct} and d) R_{int} at various DOD for PEHPC and KB

Finally, if the PEHPC can indeed redirect the PS diffusion inwards then there should be some significant difference in the electrolyte resistance between PEHPC and KB electrodes. To confirm this theory, *operando* electrochemical impedance spectroscopy measurements (EIS) is performed at various depth of discharge (DOD). A “snapshot” of various circuit parameters (R_e, R_{ct}, R_{int} shown in **Figure 3-9b-d** respectively) is revealed at different DOD. Specific fitted circuit parameters are presented in **Table 3-1** (PEHPC) and **Table 3-2** (KB). It should be noted that the n-value for the Warburg-like element was allowed to vary i.e. fitted.

Table 3- 1: Fitted Equivalent Circuit Parameters for PEHPC.

Voltage	DOD%	R_e	Y_{int}x10^5	N_{int}	R_{int}	Y_{ct}x10^5	N_{ct}	R_{ct}	Y_{War} x10^2	N_{War}
3.000	0.00	3.19	1.24	0.78	42.93	191.01	0.61	10.91	2.22	0.83
2.350	4.17	3.43	1.54	0.76	49.48	210.43	0.58	8.18	34.30	0.51
2.332	8.33	3.83	1.24	0.78	41.07	62.77	0.62	14.15	34.87	0.75
2.321	12.50	4.28	1.24	0.77	40.84	111.06	0.67	8.03	23.83	0.47
2.307	16.67	4.56	0.93	0.80	33.96	68.95	0.65	10.51	17.61	0.40
2.258	20.83	4.93	1.02	0.79	32.67	231.58	0.54	10.90	18.62	0.54
2.171	25.00	5.18	0.99	0.79	28.14	258.53	0.57	7.44	16.92	0.50
2.112	29.17	5.50	0.90	0.80	23.46	322.32	0.56	6.75	15.17	0.48
2.109	33.33	5.32	0.93	0.80	24.64	361.87	0.50	9.01	19.19	0.58
2.109	37.50	4.95	0.92	0.80	25.19	294.44	0.54	8.16	21.51	0.63
2.119	41.67	4.74	0.74	0.82	22.76	197.98	0.57	7.95	20.81	0.60
2.118	45.83	4.58	0.85	0.81	22.85	163.02	0.68	5.54	19.56	0.56
2.126	50.00	4.37	0.56	0.85	19.47	141.51	0.59	8.18	19.48	0.60
2.125	54.17	4.22	0.62	0.84	19.20	181.98	0.57	7.72	18.43	0.61
2.119	58.33	4.06	1.76	0.75	22.80	257.22	0.77	3.31	16.36	0.59
2.119	62.50	3.89	0.69	0.84	18.67	306.16	0.52	7.62	14.33	0.62
2.110	66.67	3.87	1.85	0.76	17.94	191.58	0.52	7.39	11.31	0.58
2.116	70.83	3.77	0.96	0.81	19.64	534.28	0.52	5.95	8.50	0.57
2.097	75.00	3.68	0.78	0.83	18.93	156.59	0.63	5.41	6.50	0.55
2.116	79.17	3.57	1.22	0.79	20.96	174.67	0.76	2.89	4.80	0.59
2.062	83.33	3.58	0.67	0.84	18.08	116.72	0.64	6.09	3.95	0.69
2.058	87.50	3.50	1.86	0.75	20.85	357.08	0.72	3.74	3.49	0.82
1.819	91.67	3.40	1.03	0.81	18.12	288.51	0.67	4.11	4.40	0.76
1.804	95.83	3.42	1.26	0.79	17.94	299.21	0.68	3.78	4.23	0.74

1.725	100.00	3.37	0.60	0.86	15.85	367.23	0.52	7.01	3.77	0.74

Table 3- 2: Fitted Equivalent Circuit Parameters for KB.

Voltage	DOD%	R_e	Y_{int}x10^5	N_{int}	R_{int}	Y_{ct}x10^5	N_{ct}	R_{ct}	Y_{War} x10^2	N_{War}
2.57	0.00	6.43	2.04	0.91	1.06	138.86	0.80	3.64	0.239	0.18
2.32	6.67	7.65	0.56	0.67	2.35	400.04	0.91	4.05	0.434	0.51
2.29	13.33	10.47	0.48	0.77	3.19	190.73	0.91	5.36	0.261	0.42
2.27	20.00	15.45	1.84	0.74	5.52	197.59	0.77	10.18	0.161	0.46
2.22	26.67	18.15	0.69	0.50	14.66	448.00	0.84	10.01	0.127	0.52
2.12	33.33	15.02	1.79	0.98	4.89	74.10	0.76	10.07	0.074	0.33
2.07	40.00	12.53	2.04	0.61	11.73	320.03	0.74	11.95	0.080	0.48
2.09	46.67	11.45	2.35	0.60	17.13	207.94	0.72	15.09	0.050	0.43
2.09	53.33	10.83	2.51	0.62	21.85	124.24	0.72	14.36	0.036	0.43
2.08	60.00	10.19	0.93	0.53	30.60	145.66	0.82	11.21	0.045	0.45
2.08	66.67	9.80	3.85	0.56	37.67	111.34	0.70	14.04	0.035	0.49
2.07	73.33	9.12	20.08	0.60	33.97	132.98	0.56	20.88	0.039	0.50
2.05	80.00	8.24	1.33	0.50	46.09	141.27	0.81	10.44	0.049	0.54
2.00	86.67	7.46	1.53	0.52	45.82	140.49	0.80	10.95	0.047	0.53
1.91	93.33	7.08	1.87	0.81	22.88	55.26	0.77	14.43	0.025	0.28
1.75	100.00	6.58	0.82	0.43	87.57	243.26	0.90	9.09	0.066	0.85

Figure 3-9a indicates the DOD locations of EIS captures with black and red squares for both PEHPC cell and KB cell (respectively) during 1st discharge at 0.1C. The circuit that is used for fitting is shown in the bottom portion of Figure 3-5b, identical to the circuit in work by Yuan *et al.* [98] R_e is normalized to the R_e of a fresh cell, this is done to de-convolute any differences in electrical connection between KB and PEHPC. If the viscosity of the electrolyte is to be controlled,

there should be drastic difference between KB's and PEHPC's R_e value throughout discharge. As seen in Figure 3-9c, R_e initially increases for both KB and PEHPC due to the dissolution of PS, and as expected, decreases once the soluble PS converts to solid Li_2S products. Aligning with our expectations, KB experiences a much higher increase in electrolyte resistance throughout discharge (~280% increase) when compared to PEHPC (~72% increase), indicating PEHPC can indeed limit PS dissolution into the bulk. The R_{ct} for PEHPC is higher than that of KB from 0-20% DOD. However, once 20% DOD is reached, KB's R_{ct} appears to increase while PEHPC decreases. This supports our speculation that the viscosity increases more for KB than for PEHPC. With a higher PS concentration, the R_{ct} of KB increases as the charge transfer between polysulfide will likely be hampered by more paired polysulfide interactions. Whereas in the case of PEHPC, the effect of PS dissolution on R_{ct} is insignificant. Instead, R_{ct} is observed to decrease continuously throughout discharge for PEHPC.

R_{int} value for PEHPC also starts at a much higher value than that of KB and remains higher from 0-50% DOD. This is most likely due to the higher electrical conductivity of commercial KB compared to our in-house-made carbon material. Interestingly, upon reaching 30% DOD in the KB electrode (corresponding to the beginning of the 2nd plateau), a sharp increase in R_{int} is observed. This is to be expected as the precipitation of Li_2S occurs during the 2nd plateau. At~50% DOD, the interfacial resistance for KB increases past PEHPC. This is most likely due to the inability of KB to retain PS in a localized region, resulting in random precipitation and agglomeration of Li_2S throughout the electrode. These Li_2S agglomerates greatly increase the interfacial transfer of electrons, whereas PEHPC is able to retain PS in the core, limiting redistribution. Hence, no increase in interfacial resistance is observed. By lowering viscosity of the bulk electrolyte and the corresponding resistance in the cell, PEHPC is able to deliver ~500 mAh g^{-1}_{sulfur} at 9C. Both the nitrogen doping and partial redirection of PS diffusion ensures a much larger population of sulfur participated in the reduction reaction even at a high 9 C discharge rate.

3.4. Conclusion

A novel method was employed to synthesize a micron sized hollow carbon with a nitrogen doped porous shell using a Pickering emulsion. Melamine formaldehyde resin was used to polymerize and crosslink over the CO_2 emulsion, consolidating and casting the delicate hollow morphology. The mechanism was revealed to be strongly dependent on the degree of agitation and the pH of the solution. PEHPC was used as a sulfur host for lithium sulfur battery and demonstrated impressive rate performance up to 9C (500 mAh g^{-1}) and excellent cycle stability (~85% retention at 150 cycles), outperforming commercially available KB carbon black (113 mAh g^{-1} at 9C, 36% capacity retention at 0.5C and 150 cycles). A comparison to other works is presented in **Table 3-3**.

Table 3- 3: Rate performance comparison between PEHPC and some published works.

Rate Performance	Loading	Electrolyte used	Citation	Year	Sulfur host
450 mAh g^{-1} @ 3C	N/A	N/A	Angew. Chem. Int. Ed. 2011, 50, 5904	2011	Hollow carbon
350 mAh g^{-1} @ 1C	N/A	N/A	Angew. Chem. Int. Ed. 2012, 124, 9730	2012	Double shell hollow carbon
713 m Ah g^{-1} @ 10C	0.8-1.1 mg cm^{-2}	100 µl per cell	Nat. Commun. 2014 , 5 , 3410	2013	Unstacked graphene
430 mAh g^{-1} @ 3C	3.9 mg cm^{-2}	N/A	Adv. Energy Mater. 2015 , 5 , 1402263	2015	Graphene wrapped double shelled, nitrogen doped, hollow carbon spheres
656 mAh g^{-1}@ 5C	2 mg cm^{-2}	15 µl per cell	Adv. Funct. Mater. 2016, 26, 577	2016	

					Hierarchical porous graphene
500 mAh g^{-1} @ 9C & 670 mAh g^{-1}@7C	1.3 mg cm^{-2}	17 µl g$^{-1}_{sulfur}$	This work	2016	PEHPC

To understand the superior performance of PEHPC, the shuttle current and EIS measurements were conducted. PEHPC revealed an interesting transient shuttle current profile when compared to the KB cells, providing a window into understanding the mass transfer dynamics of hollow structures for sulfur battery application. Electrochemical impedance spectroscopy revealed a drastic difference between the electrolyte, charge transfer and interfacial resistance of PEHPC and KB providing further evidence on the effects of a hollow nitrogen doped structure. We attributed these results to the inward diffusion of PS, which alleviated the viscosity increase experienced by the bulk electrolyte.

In this chapter, we have developed hollow nitrogen-doped carbon with a porous shell for Li-S batteries. However, the performance is only tested at relaxed conditions. In the next chapter, we will discuss the performance of this material at strict conditions followed by its role as a key building block for Chapter 4 where it was spray-dried with graphene oxide, achieving good performance at strict testing conditions. The next chapter will investigate the further develop of this material for application in strict testing conditions (high sulfur areal loading and low electrolyte content).

Chapter 4: A Lithium–Sulfur Battery using a 2D Current Collector Architecture with a Large-Sized Sulfur Host Operated under High Areal Loading and Low E/S Ratio

This chapter is reprinted in adopted form with permission from Advanced Materials

M. Li, Y. Zhang, Z. Bai, W. Liu, T. Liu, J. Gim, G. Jiang, Y. Yuan, D. Luo, R. Yassar, X. Wang, Z. Chen, J. Lu, A Lithium–Sulfur Battery using a 2D Current Collector Architecture with a Large-Sized Sulfur Host Operated under High Areal Loading and Low E/S Ratio, Advanced Materials, 2018, 30, 1804271. Copyright Wiley-VCH 2018.

4.1. Introduction

In Chapter 3, we discussed a strategy to mitigate the problems of LSB tested at relaxed conditions (low areal sulfur loading and high electrolyte content). However, at these relaxed conditions, the mass of the dead-weight materials (current collector and electrolyte) significantly reduces the energy density of the overall battery. This effectively renders the initial energy-density benefits of a sulfur-based cathode useless. To make sulfur-based cathode commercially competitive, cells must be tested at strict conditions (high areal loading and low electrolyte to sulfur ratio). Unfortunately, directly testing the hollow carbon material developed in Chapter 3 at strict conditions did not yield favorable results. As shown in **Figure 4-1a-b**, at a strict testing conditions of 4 mg_s cm^{-2} sulfur areal mass loading and electrolyte content of 7µL mg_s^{-1}, the cell did not run properly with severe capacity fade only after 5 cycles. Furthermore, a large overpotential is also observed at around 300 mAh g^{-1}, which could be related to a combination of high polysulfide concentration (as discussed in the *operando* EIS experiments presented in Chapter

3) and also nucleation of Li_2S.[168] Interestingly, the initial discharge capacity is still very high (1200 mAh g^{-1}). This indicates that the mass transfer limitation of increasing the sulfur loading by 2.7 times did not impede the Li-ion transfer at 0.05C, which could be traced back to the high rate performance offered by the HPC shown in Chapter 3. However, the low cycle retention is an indication of a lack of polysulfide retention. Therefore, in this chapter, we further enhanced this material *via* additional confinement of polysulfide and further increase of electrode pore volume for cycling at strict conditions.

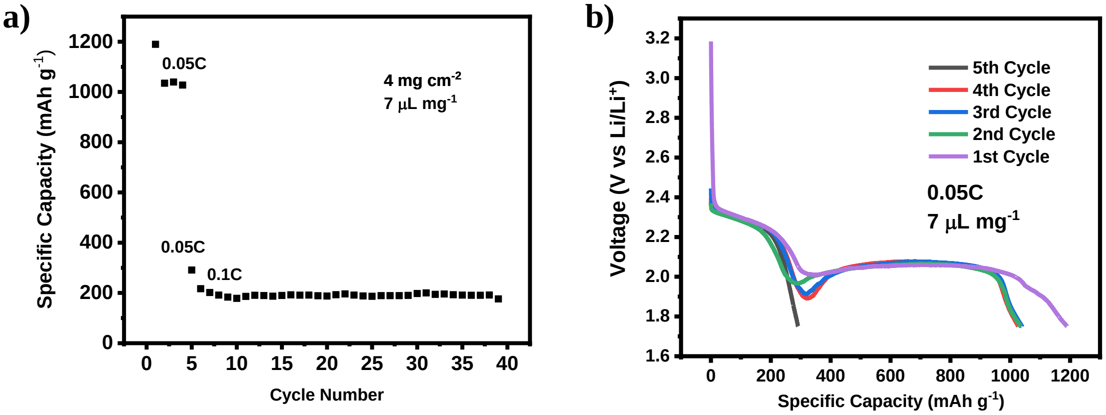

Figure 4- 1a) Galvanostatic cycling data of HPC at 0.05C for 5 cycles and then 0.1C @ 4 mg cm^{-2} and 7 μL mg^{-1} and b) the corresponding voltage profile of the first 5 cycles at 0.05C.

With more and more researchers beginning to realize the importance of these parameters, recent trends in literature reveal a large emphasis on the electrolyte to sulfur ratio (E/S) due to its large impact on the overall energy density of the LSB cell.[48,169,170] As a benchmark, Hagen *et al*[45] among others[171] have noted that even with an extremely low E/S of 3, the projected energy density would just match that of the current lithium ion battery (LIB) technologies. As the performance of LSB drastically decreases with decreasing electrolyte volumes, there are almost no published reports reaching E/S levels below 3. One of the key challenges in achieving low E/S ratio lies in enhancing the electrode's ability to access the electrolyte. This is a major factor influencing the observed excellent performance of the many backless freestanding electrodes (BFE).[47,172-175] BFE electrodes have at least double the pore openings (front and back) to access the electrolyte residing in the various free space of the coin cell while traditional 2-D blade casted electrode only have one opening. In addition to scalability issues such as electrode manufacturing, in-plane electron transfer, and electrodes to tab welding procedure,[176] the advantages of the BFE designs over the 2-D electrode might not carry over to the other battery cell configurations (pouch cell, cylindrical) where excess void spaces are mostly eliminated from the vacuum sealing process.

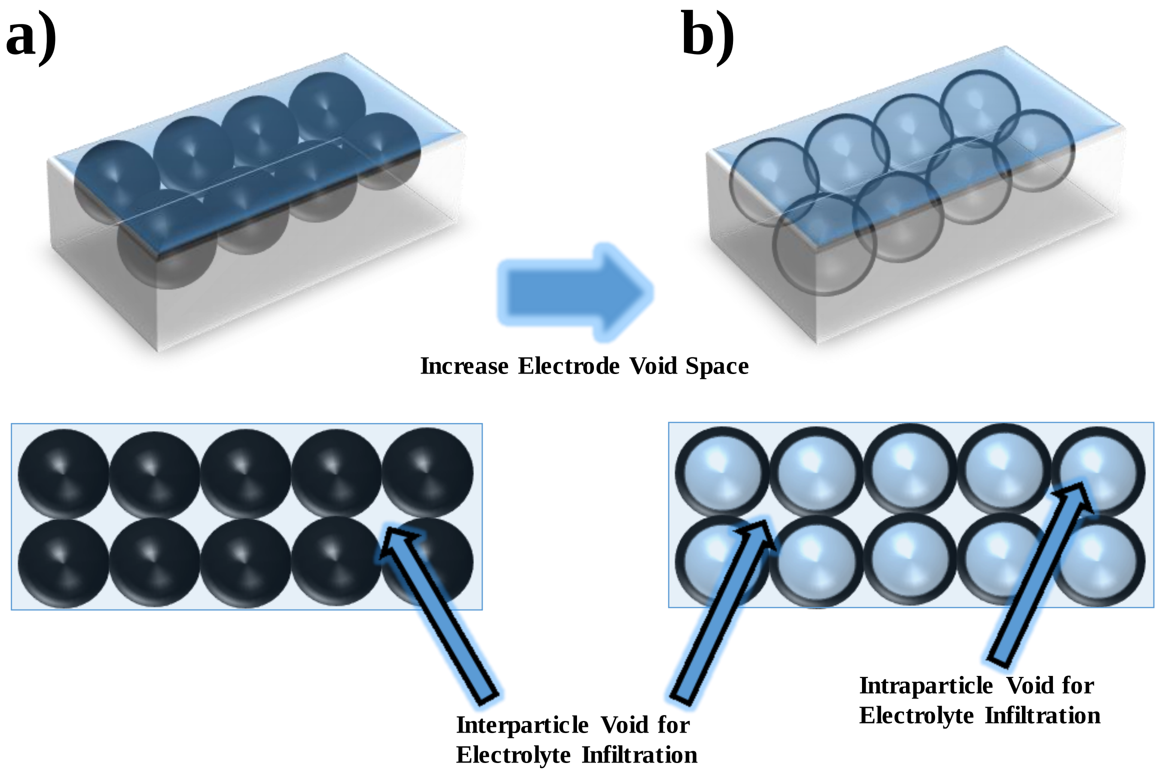

Figure 4- 2: Schematic of a) low porosity electrode with non-hollow material and b) high porosity electrode with micron sized hollow material.

While the 2-D electrode configuration is likely commercially imperative, their single sided nature, along with the typically used purely microporous/mesoporous sulfur hosts will form an overall porous structure with low void space for electrolyte (illustrated in **Figure 4-2a**). As a result, 2-D current collectors have a much smaller presences in the overall field of high loading sulfur electrodes, especially at strict conditions.[19] However, if the microporous/mesoporous sulfur hosts were made with large intrinsic voids, as envisioned in **Figure 4-2b**, the intrinsic macroporous void space can act as an extra electrolyte reservoir for enhancing electrolyte accessibility. In this way, some of the main benefits of BFEs can be transferred to the 2-D electrode configuration and is the key design strategy of this chapter.

Because the term macro-porosity is commonly associated with bulkiness, fluffiness and ultimately impracticality (in the context of battery specific/volumetric energy density), this might be pre-emptively dismissed as an invalid strategy towards lean E/S, as the large void spaces will be expected to demand a high E/S. Upon closer inspection, often reported electrolyte ratios of >10 E/S are theoretically impossible to reside inside of the cathode and separator (the only porous non-casing components of the cell). Listed in **Table 4-1** (shown below) are the calculated theoretical upper limit for E/S ratios of a few publications with reported electrode thickness. These values were calculated based on the following equation:

Equation 10: Theoretical E/S ratio equation.

$$E/S_{\ Theoretical}(\mu L\ mg_s^{-1}) = \frac{\left[V_{electrode} + V_{separator}\right](\mu L)}{m_s\ (mg)}$$

In this equation, $V_{electrode}$ represents the total volume of the electrode assuming the entirety of the electrode is void space, $V_{\mathrm{separator}}$ represent the total volume of the commercial Celgard separator as provided by the manufacturer and m_s represents the absolute mass of sulfur in the electrode. It should be noted that based on this equation, the theoretical upper E/S ratio is still quite a conservative estimate as it does not include the space taken by the solid material in the electrode. That is, this equation assumes the electrode volume is entirely void space.

This simple calculation of theoretical E/S ratio indicates that the performance enhancements observed by many works with a high E/S ratio are only physically achievable due to the extra void space in the coin cell, which are not available in the pouch/cylindrical cell configurations. However, when the electrolyte content is decreased, the wetting of the electrode becomes nontrivial and the accessibility of the extra void space in the coin cell casing might not be accessible anymore.

Table 4- 1: Calculated theoretical E/S ratio comparison with literature

Publication Title	Areal S loading [mg cm^{-2}]	Electrode Thickness [μm]	Thickness of Separator (Celgard 2340) [μm]	Void % of separator [%]	Theoretical E/S [μL mg^{-1}]
High Energy Density Lithium-Sulfur Batteries: Challenges of Thick Sulfur Cathodes[40]	3.5	80	38	45	2.77
Long-Life and High-Areal Capacity Li-S Batteries Enabled by a Light-Weight Polar Host with Intrinsic Polysulfide Adsorption[177]	5	150	38	45	3.34
A Comprehensive Approach toward Stable Lithium-Sulfur Batteries with High Volumetric Energy Density[170]	5.1	215	38	45	4.55
A High-Volumetric-Capacity Cathode Based on Interconnected Close-Packed N-Doped Porous Carbon Nanospheres for	5	50	38	45	1.34

Long-Life Lithium–Sulfur Batteries[178]					
Cathode materials based on carbon nanotubes for high-energy-density lithium–sulfur batteries[179]	3.72	215	38	45	6.23
Compact high volumetric and areal capacity lithium sulfur batteries through rock salt induced nano-architectured sulfur hosts[51]	4	109	38	45	3.15
Foldable interpenetrated metal-organic frameworks/carbon nanotubes thin film for lithium–sulfur batteries[180]	11.33	80	38	45	0.86
Strings of Porous Carbon Polyhedrons as Self-Standing Cathode Host for High-Energy-Density Lithium-Sulfur Batteries[44]	8	79	38	45	1.20
This work	8	239	25 (Celgard 2500)	55 (Celgard 2500)	3.16

To this end, we increase the porosity of the electrode. The material developed in Chapter 3 serves as an ideal starting point as it possesses large internal voids. Its large-sized hollow macroporous-sized diameters (i.e. intrinsic macropores) can replicate the main beneficial features of 3-D current collector designs. This type of material poses as a particularly attractive sulfur host material for the 2D electrode configuration under lean E/S. The large intrinsic internal voids should be excellent for providing local electrolyte reservoirs that can serve to lower the electrolyte viscosity, which would be ideal for low electrolyte-high loading sulfur electrodes. However, most particle sizes (<1 μm) are relatively small which would create small interparticle pores (poor "bulk" electrolyte Li-ion transfer), voiding any advantages gained from its hollow nature at higher areal sulfur loadings. Furthermore, it is well known that it is difficult to achieve robust high loading electrode when using a cathode active composite that has high surface area.[86] To solve these problems, there are numerous work in the LIB and LSB fields investigating techniques to produce secondary particles with the same advantages of nanosized morphologies while mitigating the disadvantages (reduced exposed surface area). These techniques can be considered quite mature in the field of 2D-electrode based high areal S loading LSB.[86,105,181,182] In this chapter, we build upon our developed hollow N-doped carbon with a porous shell and spray-dry them with graphene oxide to produce an agglomerate hollow N-doped carbon structure wrapped with reduced graphene oxide.

4.2. Experimental methods

4.2.1. Material:

1:1 v/v 1,3 dioxolane (DOL) and dimethoxyethane (DME) with 1M LiTFSI and 0.2M $LiNO_3$ was purchased pre-blended from BASF. All other chemicals were purchased from Sigma Aldrich.

4.2.2. Synthesis of Micron Size Hollow Carbon

The synthesis is similar to our previously reported work (as presented in Chapter 3).[46] Briefly, 12.6 g of melamine, 50 mL of water, 32.5 g of 40% formalin solution with 4 mL of 2M Na_2CO_3 was heated to 75 Celsius in a 400 mL beaker covered with a watch glass and under 900 RPM agitation with a 2 inch cylindrical Teflon coated magnetic stir bar. Once the solution became clear, the solution was stirred for an addition 2.5 minutes. To follow, 120 mL of 5% Ludox AS40 at room temperature was quickly added into the solution and the temperature set point was changed to 40^oC and stirred for 25 minutes. The pH was then lowered to 4.7 with 2M HCl and stirred for 1 minutes. The agitation was then halted, and the solution was allowed to precipitate for 2.5 hours. The top layer was decanted, and the remaining white slurry product was vacuum dried at 40^oC over two days and then cured at 180^oC under argon. The product was then carbonized at 900^oC for 2 hours with a ramp speed for 5 ^oC/min. The obtained black powder was then washed in 10% hydrofluoric acid for 1 day and then carefully washed to pH 6-7 with water.

4.2.3. Synthesis of sulfur and HPC composite

HPC was mechanically milled with sulfur to achieve a theoretical sulfur loading of 75%. The powder was then transferred into a Teflon lined autoclave under argon gas and heated to 155 ^{o}C for 12 hours. The resulting powder is HPC/S75.

4.2.4. Synthesis of graphene oxide

Graphite of 2-10 μm mesh was converted to graphene oxide through a modified Hummer's method,[183] washed to pH 5-6 and then freeze dried.

4.2.5. Synthesis of Sprayed Dried Graphene-N-doped Porous Hollow Carbon

300 mg of graphene oxide was dispersed in 60 mL of pure water. Separately, 1.5 g of HPC/S75 was dispersed in 100 mL of water via sonication for 4 hours. The two dispersions were then mixed with a magnetic stir bar for 2 hours. The resulting final dispersion was then dried through a spray dryer at 200 ^{o}C with a nozzle pressure of 0.1 MPa and a fan speed of 100 Hz. The collected product was then transferred into an argon filled autoclave and heated to 230 ^{o}C for 16 hours for the reduction of graphene oxide. The final product is known as SDHPC.

4.2.6. Electrochemical Characterization

All electrodes were fabricated in a similar fashion. Active material composite, carbon nanotube and LA 133 binder were mixed at 90:5:5 mass ratio with a 25% solid slurry content (water based) and casted onto commercial C-coated Al foil (MTI) with a doctor blade. The electrodes were punched into 16 mm diameter disc and dried at 65 ^{o}C for 4 hours and transferred into an Ar filled glove box (Labstar MB10 compact, mBraun) with water and O_2 content below 0.5 ppm. The electrochemical performances were evaluated using a 2016 type coin cell. Electrochemical cycling tests were performed with a Neware battery testing station. Lithium metal chip from Linyi Gelon LIB Co., Ltd was used as the counter electrode and reference electrode for all tests (600 µm thick) . The separator used was Celgard 2500. For coin cell assembly, the electrolyte to sulfur ratio was tested at 7 and 2.8 µL mg^{-1}. The coin cells were cycled from 2.8 V to 1.9 V vs Li/Li^+ was used for testing of the cell with 7 µL mg^{-1} electrolyte content and 2.8 V to 1.0 V vs Li/Li^+ for the 2.8 µL mg^{-1}. Shuttle current was performed accordingly to Moy *et al*,[184] after cycling the cells at 0.1C for 3 cycles and then finally discharging to 2.2 V, held at open circuit voltage for 10 minutes before holding potentiostatic at 2.2 V where the current response was recorded. Potentiostatic electrochemical impedance spectroscopy was conducted on a 1400 CellTest System from Solartron analytical tested from 100000-0.01 Hz with a 10 mV amplitude. After each galvanostatic discharge step, for the 2.5 mg cm^{-2} cells, the impedance was immediately taken without rest while the 8 mg cm^{-2} cells were allowed to rest 5 minutes before the impedance measurements were collected (to reduce noise at the cost of state-of-system accuracy). Impedance circuit fitting was performed using the Zfit function developed by Jean-Luc Dellis, implemented in Matlab. The 8 mg cm^{-2} electrode was 262 µm thick including the current collector (23 µm) with a theoretical E/S ratio of about 3.16 (details shown in Table 4-1). The diameter of the electrodes was 1.6 cm (2.01 cm^2). Each electrode had an absolute sulfur mass of 16 mg. 112 and 45 µL of electrolyte were added with a micropipette for 8 mg cm^{-2} cells tested at 7 and 2.8 µL $mg^{-1}{}_S$ respectively.

4.2.7. Physical Characterization

Electrolyte absorption measurements were performed by drop casting the droplet of electrolyte and monitoring the wetting process with a 30 fps camera and back light. The time resolved height of electrolyte droplet was manually measured using Image J software. A Zeiss Leo field-emission scanning electron microscope 1530 was used to characterize the morphology of the material. A JEOL 2010F transmission electron microscope was used to further characterize the morphology.

TGA (TA instrument Q500) was conducted under nitrogen atmosphere with a heating rate of 5 °C min^{-1}. *In Situ* X-ray diffraction experiment was conducted at the Advanced Photon Source at Argonne National Laboratory (11-ID-C beamline) The X-ray beam size was 0.2mm X 0.2 mm, and the X-ray wavelength was 0.1173 Å. Home-made coin cells were discharged at 0.05 C rate from 2.8 V to 1.2 V using a MACCOR cycler as shown in Chapter 2: Figure 2-2b . During the cell cycling, the XRD patterns were collected every 12 minutes, using a Perkin-Elmer 2D X-ray detector. The 2D diffraction patterns were then converted into 1D patterns of 2θ versus intensity using Fit2D software distant-calibrated using a CeO_2 standard.

4.3. Results and discussion

4.3.1. Synthesis and characterization of material

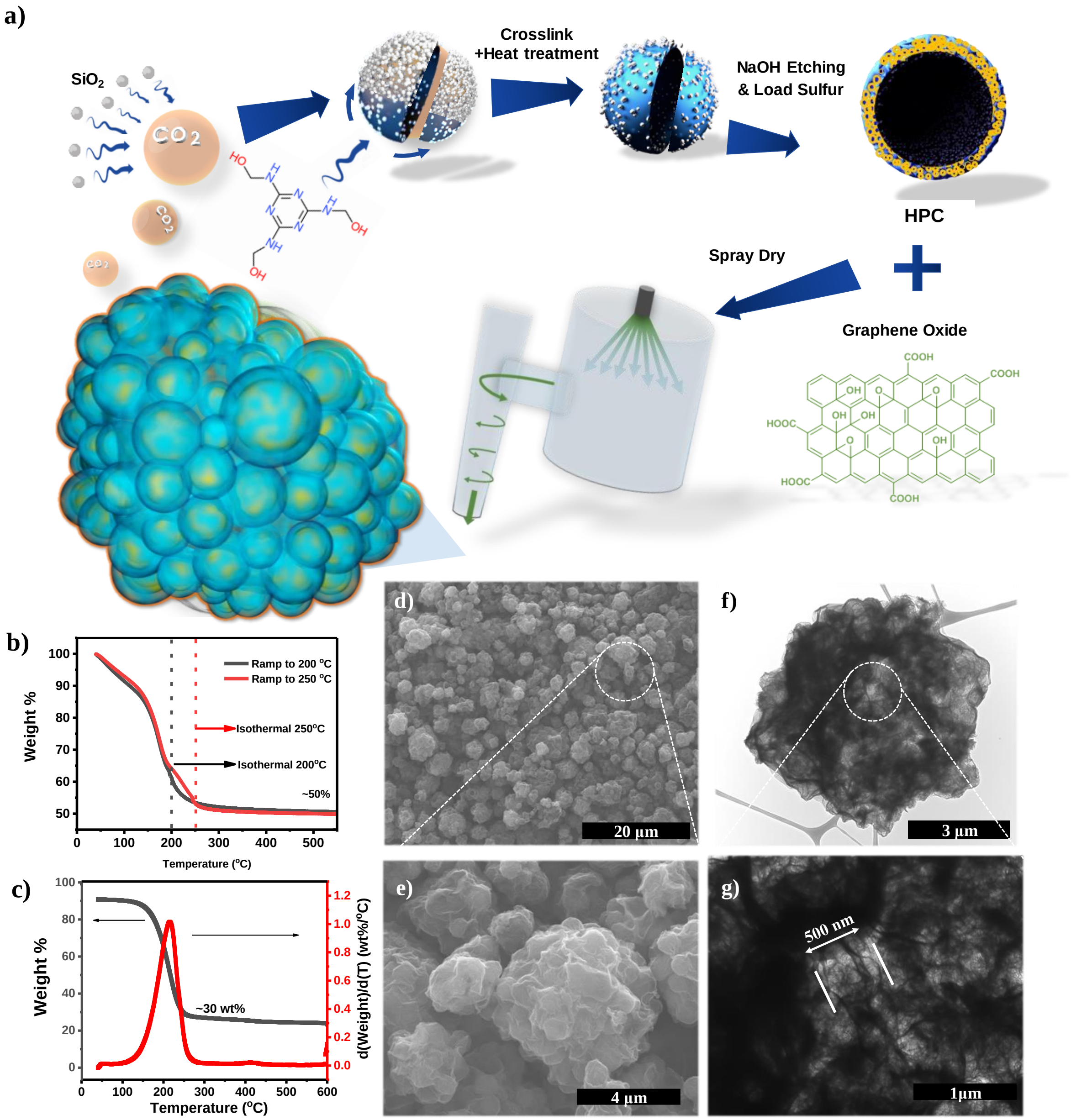

Figure 4- 3: a) Schematic of the synthesis process of SDHPC, b) TGA curves of graphene oxide ramping to 200 and 250°C followed by holding isothermal for 2 hours, c) TGA curves of SDHPC after heat treatment, d) low & e) high magnification SEM images and f) low & g) high magnification TEM image of SDHPC after spray drying and 230C heat treatment.

Our chosen agglomeration technique, spray drying,[185,186] (shown in **Figure 4-3a)** is widely used in many different industries due to its high throughput production capabilities. Specifically in this work, we first synthesized hollow porous carbons (HPC) with a large core,[46] loaded sulfur via the melt diffusion method and spray dried with graphene oxide at 200^{o}C (nozzle temperature) forming what we define as spray dried hollow porous carbon (SDHPC). The large droplet size of the atomized feed solution ensures the formation of secondary particles while the graphene oxide acts as structural support.

After heat treatment in an Ar filled autoclaved at 230^{o}C for 12 hours (GO reduction), the final SDHPC electrode material is obtained. To estimate the sulfur content in SDHPC, the mass change in GO must be first accounted for. Thermal gravimetric analysis (TGA) of GO in N_2 reveals that the stabilized mass percent did not vary appreciably between 200-250^{o}C (**Figure 4-3b**) indicating that the mass of SDHPC should have stabilized during the 12 hours 230^{o}C heat treatment in alignment with literature.[187] Accordingly, TGA of SDHPC after heat treatment only shows a single inflection (single peak in the rate of weight % change, **Figure 4-3c**) with a plateau starting at ~30 wt% at around 250^{o}C suggesting a sulfur loading of ~70%. This is in good alignment with the theoretical 68% calculated based on a HPC75S to GO mass ratio of 5:1 (spray-dryer feed) with a 50% mass retention of GO after the 230^{o}C heat treatment. The morphology of SDHPC is shown under scanning electron microscopy (SEM) in **Figure 4-3d & e** respectively, indicating the successful wrapping of graphene and the agglomeration of HPC into larger particles (SDHPC). The broad particle size distribution is due to the centrifugal-based collection mechanism of the spray dryer's cyclone [188,189] and could aid in the performance of the cell as shown in previous work.[105,190]

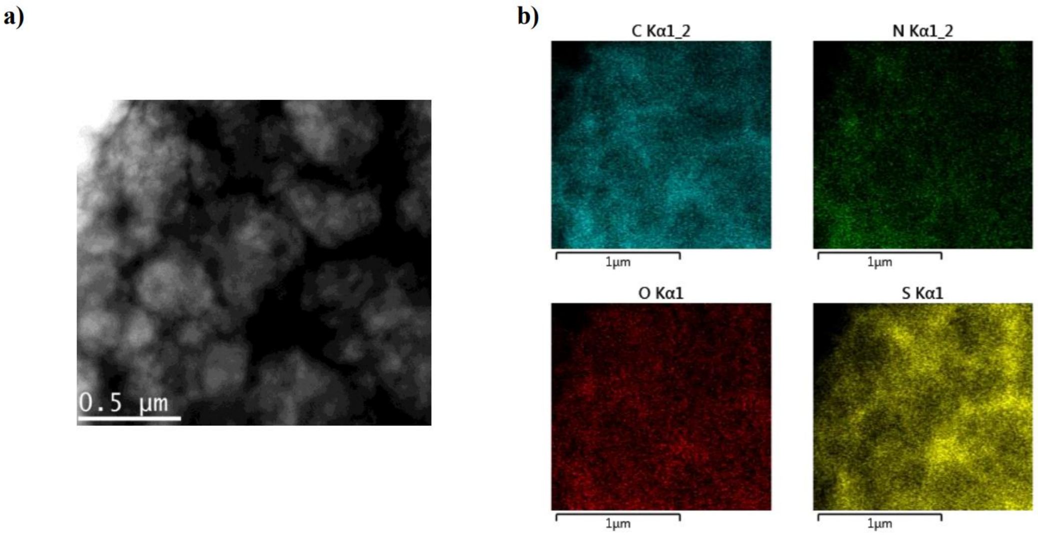

Figure 4- 4: a) TEM image of SDHPC and b) EDS map of C, N, O, and S of SDHPC

Moreover, transmission electron microscopy (TEM, **Figure 4-4f**) indicates that the graphene is wrapped throughout the structure of the secondary particle, providing an electron-conducting pathway. At higher magnifications (**Figure 4-4g**), the graphene is shown encapsulating the HPC primary particles. More importantly, the large intrinsic ~500 nm voids of the hollow structures can be clearly found intact throughout the large secondary particle. Energy-dispersive X-ray spectroscopy mapping of C, N, O, and S (**Figure 4-5a-b**, Supporting Information) further indicates that there is indeed large internal void throughout SDHPC and sulfur mostly resides in the wall of these voids. The existence of these internal voids is the most beneficial difference between SDHPC and other reported spray dried sulfur composites. These voids will serve as guaranteed intrinsic void spaces (shown in Figure 4-1b) throughout the electrode to provide electrolyte accessibility to sulfur even at a low electrolyte ratios.

4.3.2. Physical and electrochemical characterization of material in electrode

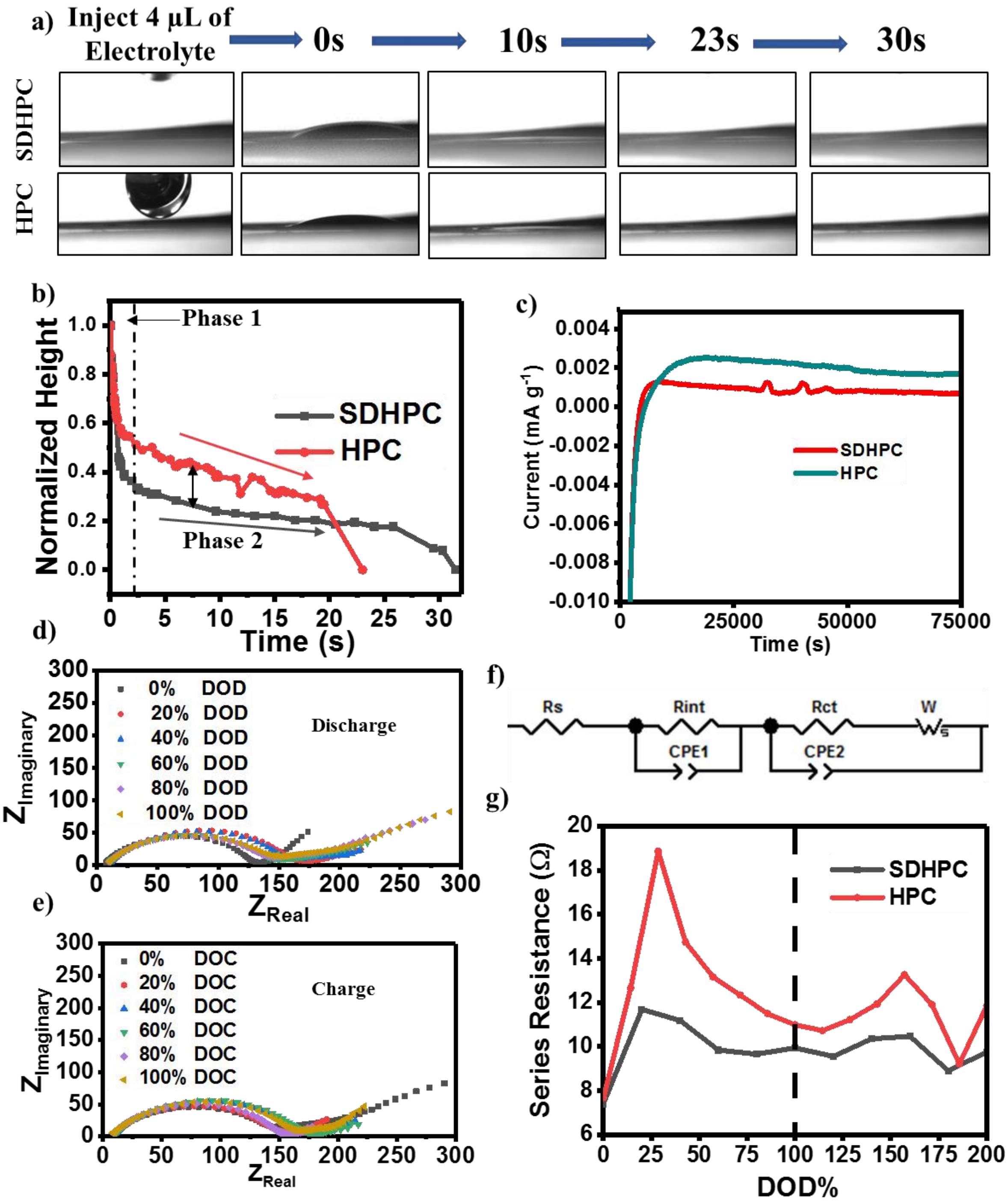

Figure 4- 5: a) Image sequence of the injection and absorption of 4 μL of electrolyte into SDHPC and HPC electrodes, b) corresponding droplet height versus time profile and c) shuttle current measurement of both SDHPC and HPC. d) Discharge and e) charge EIS

spectra of SDHPC electrode at different DOD, f) equivalent circuit model used for fitting impedance data. Fitted values of g) series resistance plotted versus DOD. Note that 0-100% DOD represents discharge while 100-200% DOD represent charge.

To confirm the infiltration of electrolyte into the voids, an electrolyte absorption test is performed. The test entailed the micro-pipetting of precisely 4 µL of electrolyte (0.2 M $LiNO_3$ and 1M LiTFSI in 1,3 dioxolane and dimethoxyethane at 1:1 v/v) onto a circular 15 mm diameter electrode (HPC and SDHPC, **Figure 4-5a**). The event was filmed and the time difference between initial contact and final absorption of the droplet is defined as the absorption time. By measuring the height of the droplet over time, a time resolved absorption profile of the electrolyte could be observed. The larger particle size of SDHPC should create larger interparticle pores,[86,105,181,182] which are expected to decrease electrolyte wetting time.[191] Interestingly, it was found that the total wetting time of SDHPC (larger interparticle pores) was ~31 s whereas HPC (smaller interparticle pores) only took ~23s, indicating that HPC absorbed the electrolyte slightly quicker. This result offers us with valuable insight into the pore structure of the SDHPC electrode. Both absorption process appears to proceed in a two-step manner (**Figure 4-5b**). It is well known that liquid (electrolyte) infiltration into a porous media (electrode) of the electrode depends on the apparent contact angle between the electrolyte and the particles, characteristic of electrode pore network and the pressure differential.[191] The initial rapid drop (labeled Phase 1) is followed by a slower plateaued infiltration region (label Phase 2) for both samples. The initial quick absorption profile is due to the pressure head produced by the height of the droplet. As the droplet is absorbed, the pressure head (a component of the driving force responsible for infiltration) will decrease to the point where it is slowed by the smaller pores in the electrode. During this slowing process, the height of the droplet will possess a more plateaued time profile. There are two distinct difference between SDHPC and HPC. Firstly, the initial decrease in height for SDHPC was much more than HPC, this is most likely due to the larger interparticle pores of the electrode.[86,105] Secondly, the slope of the plateau for SDHPC is noticeably lower than that of HPC. We believe the smaller slope of SDHPC is evidence of the wrapping of HPC with rGO and the infiltration of electrolyte into agglomerated hollow structures of SDHPC. With an increased sulfur loading, the PS retention capability of the host must be enhanced compared to the lower loadings. From the delayed infiltration of electrolyte into SDHPC, we note that it could imply a tortuous liquid pathway into SDHPC. As such, this could be beneficial in limiting the outwards diffusion of PS. Indeed, from our shuttle current measurements (**Figure 4-5c**), SDHPC possessed a significantly lower steady state current signal (0.747 $\mu A\ g^{-1}$) compared to HPC (1.68 $\mu A\ g^{-1}$) at the same areal loading (2.5 $mg\ cm^{-2}$). To further demonstrate the ability of SDHPC to limit PS outwards diffusion, we performed *in situ* electrochemical impedance spectroscopy (EIS) experiments on both HPC and SDHPC (2.5 $mg\ cm^{-2}$) as a function of state of charge/discharge (DOD, 0-100% represents discharge while 100-200% represents charge). According to the Nyquist plot for both discharge and charge of SDHPC shown in **Figure 4-5d & e** respectively, there appears to be a drastic change in cell impedance throughout discharge and charge. After fitting to a circuit model (**Figure 4-5f)**,[46,63,97,192] the series resistance versus DOD is shown in **Figure 4-5g**. All fitted values are presented in **Table 4-2** (SDHPC) and **Table 4-3** (HPC), it should be noted that the n-value of the lowest frequency value or “Warburg-like” was also fitted and was not held at 0.5.

Table 4- 2: Fitted Equivalent Circuit Values for ElS for SDHPC at 2.5 mg cm^{-2} & 7μL mg^{-1}

Voltage	DOC/ DOD	R_e	R_{int}	Y_{int}	N_{int}	R_{ct}	Y_{ct}	N_{int}	Y_{war}	N_{War}	Fval

2.4621	0	7.4	123	5.75E-06	0.793	38.6	0.113	0.936	0.0275	0.5	0.462
2.2365	20	11.7	155	7.62E-06	0.761	49.0	0.174	0.611	0.0281	0.5	0.885
2.1158	40	11.2	145	6.62E-06	0.774	54.1	0.105	0.432	0.0107	0.5	0.232
2.1251	60	9.8	126	6.05E-06	0.787	16.9	0.026	0.253	0.0034	0.5	0.259
2.1079	80	9.7	120	5.91E-06	0.787	19.3	0.015	0.269	0.0018	0.5	0.462
2.1029	100	9.9	122	5.31E-06	0.794	36.2	0.016	0.317	0.0022	0.5	0.446
2.1944	120	9.6	141	8.68E-06	0.752	36.9	0.165	0.641	0.0182	0.5	0.471
2.2409	140	10.4	157	8.37E-06	0.756	48.5	0.288	0.815	0.0171	0.5	0.534
2.3193	160	10.5	152	4.98E-06	0.802	24.8	0.149	0.499	0.0051	0.5	0.466
2.3723	20	8.9	139	5.83E-06	0.788	14.2	0.133	0.390	0.0112	0.5	0.481

Table 4- 3: Fitted Equivalent Circuit Values for ElS for HPC at 2.5 mg cm^{-2} & 7μL mg^{-1}

Voltage	DOC/ DOD	R_e	R_{int}	Y_{int}	N_{int}	R_{ct}	Y_{ct}	N_{int}	Y_{War}	N_{War}	Fval
3.2165	0	7.7	133	1.19E-05	0.744	32.4	0.020	0.849	0.0046	0.5	0.637
2.3169	16.7	12.7	44	7.17E-06	0.770	17.8	0.186	0.461	0.0051	0.5	0.232
2.1973	33.4	18.9	48	8.38E-06	0.736	19.1	0.204	0.653	0.0079	0.5	0.472
2.1449	50	14.7	41	6.22E-06	0.778	20.6	0.054	0.272	0.0058	0.5	0.233

2.1385	66.7	13.2	41	5.96E-06	0.788	20.6	0.029	0.250	0.0037	0.5	0.212
2.1352	83.4	12.3	43	7.82E-06	0.769	31.9	0.021	0.300	0.0036	0.5	0.258
2.1258	100	11.5	39	7.75E-06	0.780	20.9	0.014	0.318	0.0020	0.5	0.303
2.1169	114.28	11.0	42	1.27E-05	0.743	4.6	0.011	0.301	0.0014	0.5	0.447
2.1931	128.56	10.7	35	1.37E-05	0.742	16.2	0.121	0.451	0.0036	0.5	0.312
2.2121	142.84	11.2	34	9.52E-06	0.779	19.6	0.263	0.627	0.0032	0.5	0.178
2.2362	157.12	11.9	36	9.62E-06	0.777	20.4	0.317	0.663	0.0035	0.5	0.172
2.2903	171.4	13.3	39	3.71E-05	0.647	18.3	0.423	0.656	0.0040	0.5	0.924
2.3286	185.68	9.2	37	4.22E-06	0.843	19.9	0.665	0.694	0.0024	0.5	0.261
2.3596	200	11.9	35	5.22E-06	0.825	22.5	0.990	0.809	0.0021	0.5	0.361

The series resistance is found to increase until 25-30% DOD followed by a steady decrease into the end of discharge. During charge, the series resistance steadily increases again, peaking at around ~160 DOD followed by a decrease until the end of charge which is corroborated by literature.[46,97,99] Interestingly, throughout discharge and charge, the series resistance of HPC was higher than SDHPC. For LSB, changes in the series resistance are usually attributed to the resistance of the electrolyte, and increases with increasing polysulfide concentration.[98,193] Therefore, our results suggest that SDHPC is able to limit the polysulfide concentration in the bulk electrolyte more effectively than HPC, which corroborates well with the electrolyte absorption and shuttle current measurements

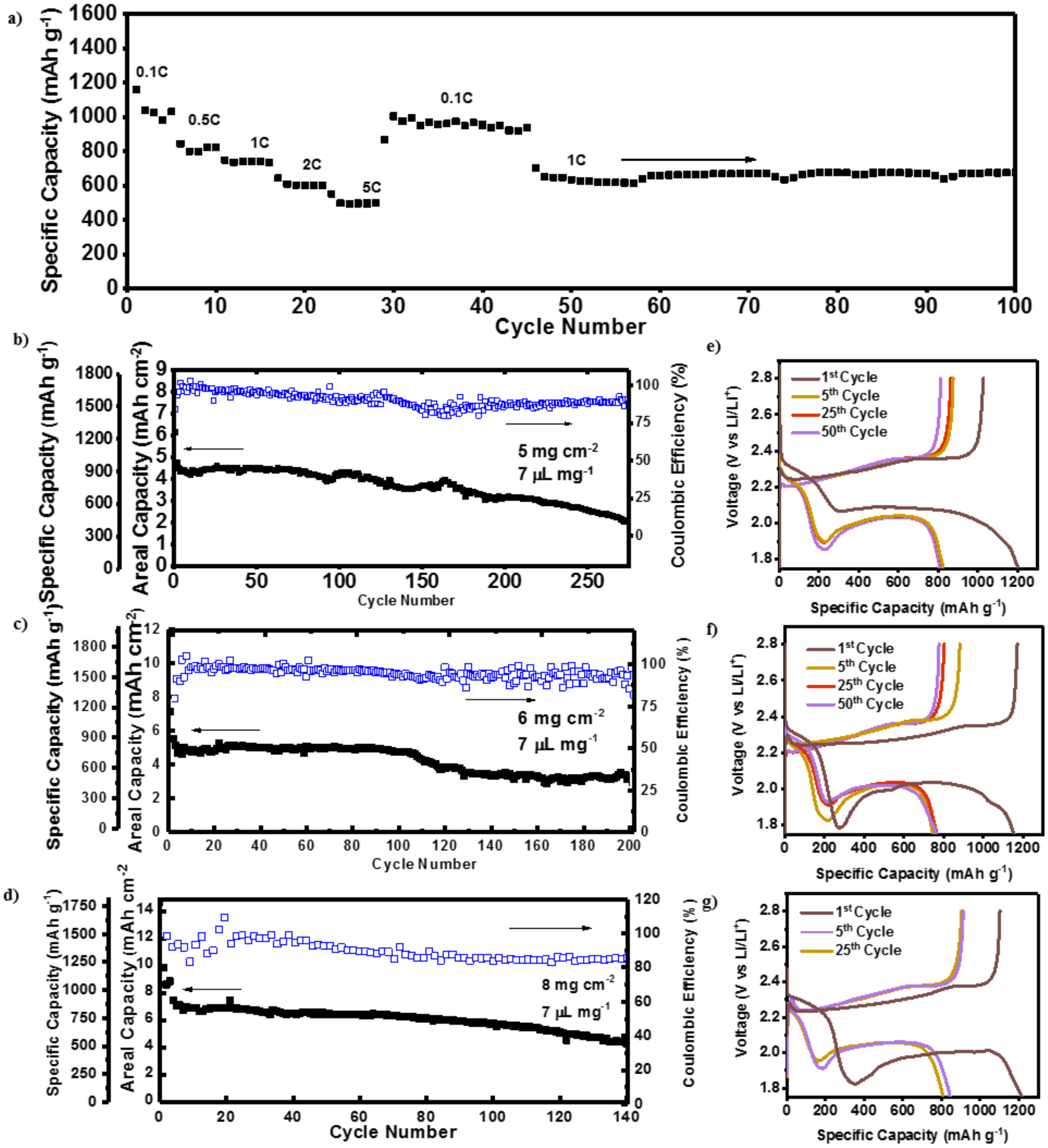

Figure 4- 6: a) Rate performance of SDHPC at 2.5 mg cm^{-2} with 7 µL mg^{-1} of electrolyte, b-d) specific capacity with Coulombic efficiency versus cycle life of SDHPC at 5, 6 and 8 mg cm^{-2} respectively and e-g) charge/discharge profiles of SDHPC at 5, 6 and 8 mg cm^{-2} respectively. Note that 5 and 6 mg cm^{-2} cells were cycled at 0.05C for four activation cycles

before cycling at 0.1 C for the cycle life measurements while the 8 mg cm^{-2} cell was cycled at 0.05C.

The combined benefits of the macroporous internal electrode structure in addition to the high PS limiting capabilities of SDHPC is reflected in its electrochemical performances. **Figure 4-5a** shows the rate performance of this SDHPC from 0.1 C to 5 C, demonstrating exceptional electrochemical activity with a discharge capacity of ~500 mAh g^{-1} at 5 C even at an appreciable sulfur loading (2.5 mg cm^{-2}). SDHPC is found to be able to recover the majority of its original 0.1 C capacity in addition stable cycling until the 100th cycles at 1 C. **Figure 4-6b-c** displays the cycle stability of electrodes at 5 mg cm^{-2} and 6 mg cm^{-2} with 7 µL mg^{-1} of electrolyte at 0.05 C for the first 5 cycles followed by 0.1 C. **Figure 4-6d** presents the cycle stability of 8 mg cm^{-2} electrodes also with 7 µL mg^{-1} of electrolyte but cycled at 0.05 C. The corresponding voltage profiles for the 5, 6 and 8 mg cm^{-2} cells is shown in **Figure 4-6e-g** respectively. Both cells achieved a first cycle discharge of about ~1200 mAh g^{-1}.

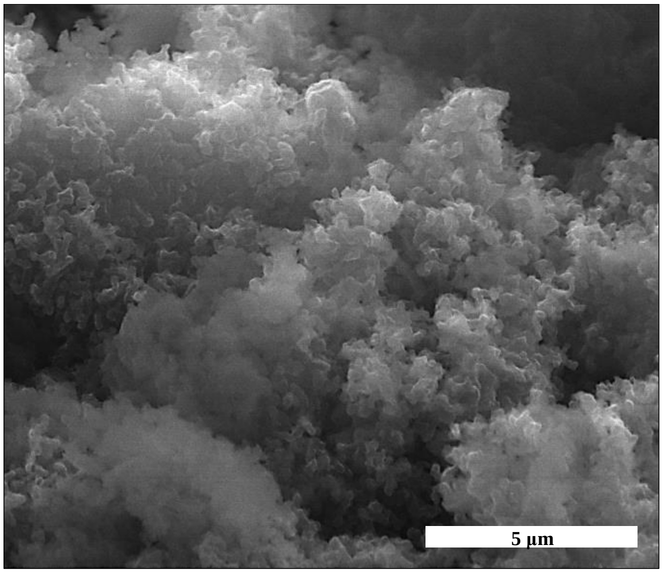

Figure 4- 7: SEM image of the corroded Li anode after cycling at high sulfur content at low electrolyte levels (same cell of Figure 4-6c)

While the 5 mg cm^{-2} cells were able to maintain relatively stable cycling upwards of 280 cycles, the 6 mg cm^{-2} experienced a significant decrease in capacity at about the 105th cycle but remained stable afterwards upwards of 200 cycles. We believe the sudden drop in capacity is related to the serious corrosion of the Li anode (post cycling SEM shown in **Figure 4-7**). It should be noted that no sudden drop in capacity is observed for the 8 mg cm^{-2} cell, which is most likely due to the lower current density's effect on the anode.[194] In terms of 2-D blade casted electrode, at this areal loading and lean electrolyte conditions, this performance is quite exceptional in terms of both capacity and cyclability compared to works published at the time of publication of this work.[40,105,170,177,182,195]

When the E/S ratio is further lowered to 2.8 µL mg^{-1}, it is found that the cell was able to cycle at a C-rate of 0.025. The voltage profile (**Figure 4-8a**) reveals a very high discharge overpotential, dropping to nearly ~1.4 V on the 1st cycle and ~1.75 V on the 2nd discharge process. However, if the C-rate is increased to 0.05 C the cell cannot discharge (voltage profile shown in **Figure 4-8c**). This is often attributed to the enormous increase in overpotential from either electrolyte viscosity (highly concentration polysulfide solution) or deposition kinetics. Work presented by Fan *et al*, have also reported similar results at lean electrolyte conditions.[196] The cycle life decreased rapidly compared to its excess electrolyte counterpart. This has been an intriguing phenomenon throughout the literature. Although the cycle performance is only for 20 cycles (**Figure 4-8b**), we have demonstrated here a material and design that can be cycled at a commercially viable electrolyte content. When compared to other high loading works, an electrolyte content of 2.8 µL mg^{-1} for an 8 mg cm^{-2} 2-D blade-cased electrode has, to the best of our knowledge, never been published. Furthermore, the composite content is >90% in the slurry formulation with very low binder content (5%) and a S content of ~70% in SDHPC, indicating that the, total sulfur content in the electrode is well over 60%.

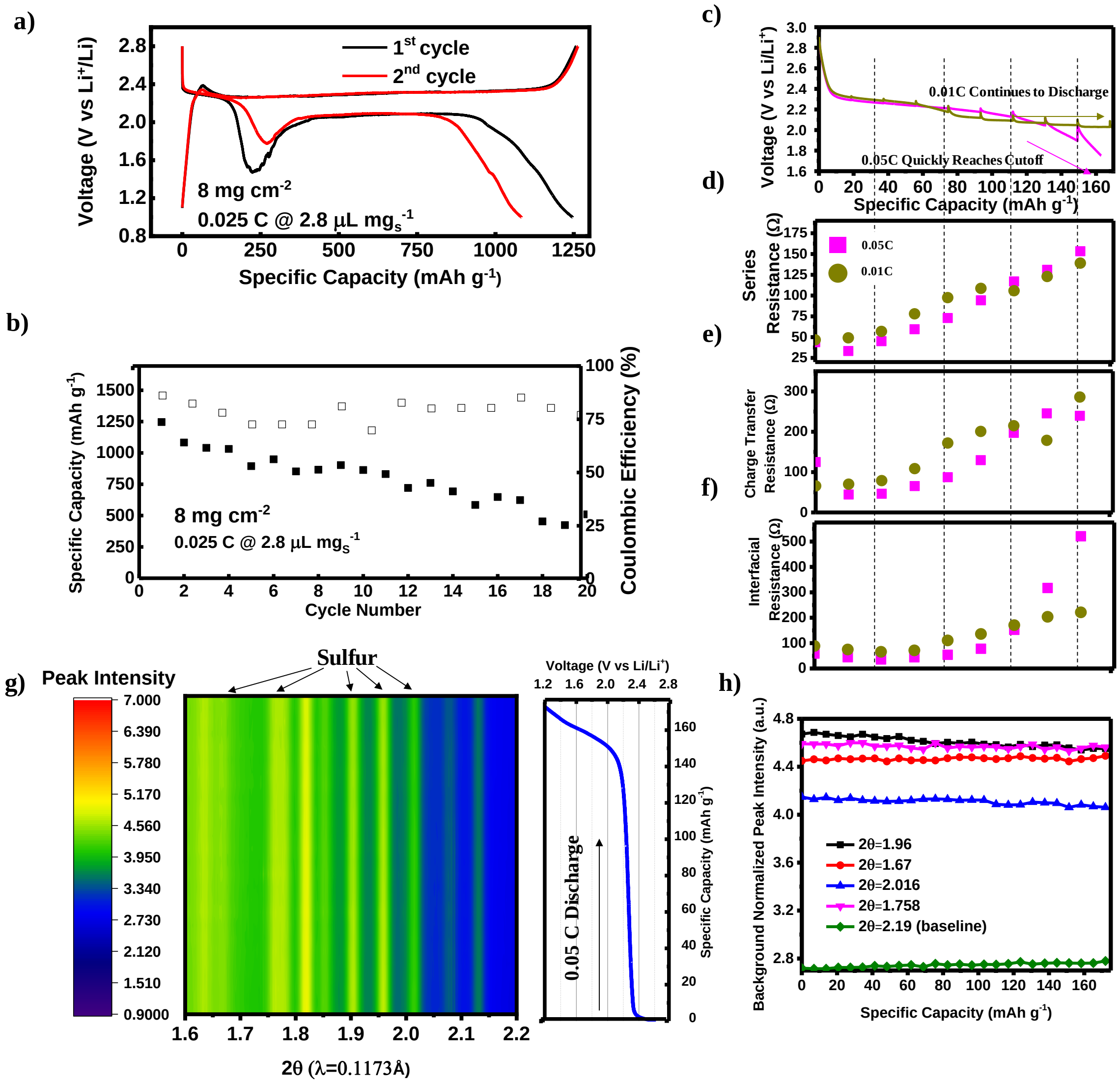

Figure 4- 8: a) Charge/discharge voltage profile and b) cycling performance at 0.025 C of SDHPC. c) Voltage profile of 8 mg cm^{-2} electrode with 2.8 µL mg^{-1} at 0.05 and 0.01C. Impedance data plotted as a function of specific capacity of SDHPC discharged at 0.05C and 0.01 C: d) series resistance, e) charge transfer resistance, f) interfacial resistance. g) In Situ

XRD contour plot of the first plateau followed by the onset of a large overpotential to 1.2 V (λ = 0.1173 Å) and h) various peak height plotted versus discharge capacity.

Unfortunately, a discharge rate of 0.025 C is hardly practical and poses a serious question as to why there is such a high overpotential. Surprisingly, there has been little work done on understanding why high loading sulfur cathode have difficulty in discharging under lean electrolyte content. To understand the cause and mechanism of the observed large overpotential prior to the 2nd plateau, we once again performed *in situ* EIS on a fresh 8 mg cm^{-2} electrode (2.8 µL mg^{-1}) discharged under two different current densities (1st at 0.05C then at 0.01C). Specifically, the cell was first discharged at 0.05C, where the voltage quickly reaches the cut off limits (**Figure 4-8c**) with the details of the overpotential build-up recorded by EIS. After charging back to 2.8V, the same cell was discharged at a significantly decreased current density (0.01C) which allowed the cell to enter readily into the 2nd plateau region without obstruction of an overpotential dip (Figure 4-5c). The results were fitted according to circuit diagram validated by Deng *et al* (same as the one used in Figure 4-5f).[97] The fitted values are presented in **Table 4-4.**

Table 4- 4: Fitted Equivalent Circuit Values for ElS for SDHPC at 8 mg cm^{-2} & 2.8 µL mg^{-1}

0.01C Discharge Current											
Voltage	**Specific Capacity**	**R_e**	**R_{int}**	**Y_{int}**	**N_{int}**	**R_{ct}**	**Y_{ct}**	**N_{int}**	**Y_{War}**	**N_{War}**	**Fval**
2.89	18.4	47	89	3E-06	0.726	65.7	1E-02	0.460	2E-03	0.5	0.24
2.31	37.7	49	75	2E-06	0.802	70.1	4E-02	0.481	1E-03	0.5	0.19
2.28	56	57	66	3E-06	0.791	78.9	5E-02	0.507	1E-03	0.5	0.23

2.27	75	78	71	6E-07	0.899	108.5	3E-02	0.478	8E-04	0.5	0.47
2.24	93.5	98	110	3E-06	0.734	171.9	2E-02	0.550	7E-04	0.5	0.15
2.18	112	109	136	9E-06	0.627	200.7	2E-02	0.574	6E-04	0.5	0.44
2.16	130	106	171	1E-05	0.580	214.9	7E-03	0.293	2E-04	0.5	0.20
2.16	150	123	204	3E-05	0.490	178.7	4E-03	0.208	8E-05	0.5	0.28

0.05C Discharge Current

Voltage	**Specific Capacity**	**R_e**	**R_{int}**	**Y_{int}**	**N_{int}**	**R_{ct}**	**Y_{ct}**	**N_{int}**	**Y_{War}**	**N_{War}**	**Fval**
2.9166	0	39	62	9E-06	0.65	16	6E-03	0.32	7E-03	0.5	0.98
2.3	18.4	29	86	3E-04	0.37	16	3E-02	0.42	3E-02	0.5	2.56
2.27	37.7	38	74	5E-04	0.33	23	7E-02	0.55	1E-02	0.5	2.64
2.25	56	50	49	6E-06	0.71	65	9E-02	0.63	2E-03	0.5	0.41
2.23	75	62	51	3E-06	0.76	33	2E-02	0.16	1E-03	0.5	2.00
2.2	93.5	78	89	1E-05	0.60	132	1E-01	0.72	2E-03	0.5	0.20
2.18	112	105	160	8E-06	0.60	198	6E-02	0.68	2E-03	0.5	0.13
2.12	130	140	298	5E-06	0.58	226	2E-02	0.39	1E-03	0.5	0.42
2.06	150	176	461	2E-06	0.65	184	4E-03	0.22	3E-04	0.5	0.52

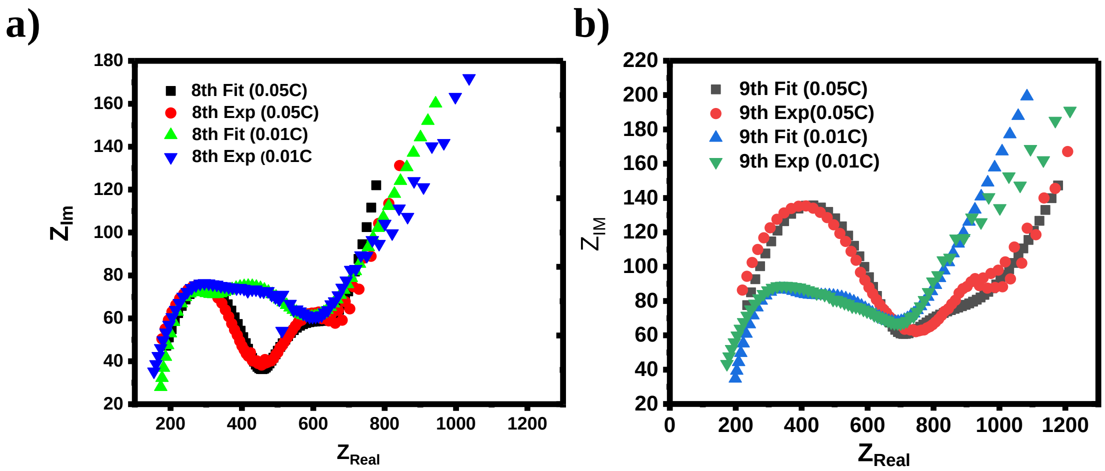

Figure 4- 9: Nyquist plot 0.05 and 0.01C for the a) 8th and b) 9th fitted and experimental impedance spectrum. Attention should be drawn in the large increase in the first semi-circle (high frequency semi-circle) at 0.05C, and the only slight change in the second semi-circle (mid frequency regime).

In general, the fitted circuit parameters (experimental spectrums can be found in **Figure 4-9**) remained quite similar between the two currents during the initial stages of discharge with variation only occurring near the end of the first plateau (onset of the large overpotential). It should be expected that when increasing the current density, the PS concentration should be much higher locally (most likely completely saturated) due to the increased rate of PS generation over PS diffusion. Although our results indicate (**Figure 4-8d**) that the series resistance of 0.01 C discharge was lower than the 0.05 C, the overall difference was not large. A similar observation is found for the charge transfer resistance (mid frequency semi-circle,[97] **Figure 4-8e**). Interestingly, the interfacial resistance (high frequency semi-circle, **Figure 4-8f** with Nyquist plots shown in **Figure 4-9a-b**) is found to increase drastically prior to the onset of the large overpotential for the higher current discharge. This indicates that of the three circuit elements, only interfacial resistance appears to change significantly near the high overpotential region of the discharge voltage profile.

Interfacial resistance is associated to the contact resistance between electron conductors within the electrode.[97,197,198] It is unclear whether solely S_8, Li_2S or even solid-state PS[199] is responsible for the large overpotential. While one might argue that the lack of capacity in the 2nd plateau should eliminate appreciable Li_2S seeding, Li_2S can still form due to disproportionation reaction or direct reduction of PS onto Li (increasing interfacial resistance on Li). To differentiate between Li_2S, S and solid-state PS, we performed *in situ* XRD in an attempt to monitor the crystal phase changes during the large overpotential (**Figure 4-8g**). Throughout the discharge of the first plateau and ending with a large overpotential, there are strong sulfur XRD signals with no indication of Li_2S peaks. Upon closer inspection of the 2θ=1.960, 2.016, 1.758 and 1.670 peak heights (**Figure 4-8h**), we concluded that there is only a minor decrease in peak intensity with slight oscillations throughout cycling. This is in stark contrast with other reports, where a steady decrease in the sulfur diffraction pattern was observed prior to the end of the 1st plateau where the peaks completely disappear.[200,201] Due to the lack of any observable Li_2S peaks, we suspect that the increase in interfacial resistance is not due to the deposition of Li_2S. As for the case of solid-state polysulfide, a recent publication has shown that the XRD patterns of polysulfides can be detected even if they were just adsorbed onto a silica surface,[201] and another work presenting electrochemical data that leads to a similar conclusion.[202] However, no such observation was made in this work, possibly excluding the existence of solid-state polysulfide. Therefore, we believe the high interfacial resistance is largely related to sulfur precipitation (S_8) and most likely not related to solid-state polysulfide or Li_2S.

Low E/S promotes solid sulfur precipitation through disproportionation reaction of concentrated high order PS. The constant regeneration of elemental sulfur deposits on already present sulfur location buffers the XRD sulfur signal, resulting in a relatively constant value. The disproportionation reaction most likely distributed sulfur locally throughout the SDHPC composite causing the observed increase in interfacial resistance. This phenomenon might be inherent to 2-D current collector designs. In contrast to the BFE designs,[173] 2-D current collectors are not composed of long ranged continuous conductive networks and will inevitably create multiple contact points between conductors. However, due to the need for large internal macropores, the number of these contact points are quite low simply due to the larger particle sizes. Due to the relatively fewer contact points between the large macroporous carbons within SDHPC and between SDHPC, we believe our material and 2-D current collector designs in general are more susceptible to interfacial resistance increases. Although we have shown that a macroporous 2-D electrodes can achieve some cyclability at extremely low electrolyte content, its performance is still inferior to that of BFEs and therefore is not a complete solution. While this might be discouraging for 2-D electrode researchers, we would like also note the enormous turnkey advantage of 2-D electrodes over BFEs when time comes for prototyping (not in the scope of this thesis).[176]

4.4. Conclusion

In this chapter, we have presented a high areal loading lithium sulfur battery (>60 wt.% S in electrode) operated under lean electrolyte content (7 and 2.8 µL mg^{-1}), well into the strict condition regime. By designing a large sized sulfur host with large intrinsic macropores encapsulated within its structure, we have enabled the stable cycling of a blade-casted electrodes of 5, 6 and 8 mg cm^{-2}. Even at 2.8 µL mg^{-1}, the 8 mg cm^{-2} electrodes demonstrated relatively stable cycling for up to 20 cycles. Furthermore, our *in situ* EIS and XRD analysis revealed intriguing properties pertaining to the mechanism of lean electrolyte operation and has for the first time identified that the interfacial resistance is the key impedance responsible for the electrodes to successfully entering into the 2nd discharge plateau for high loading/lean electrolyte cells. In terms of performance, this work significantly outperformed a large majority of the work of Li-S batteries operated at high loading and low electrolyte content. **Table 4-6** displays just how effective our design strategies was in comparison to other works.

Table 4- 5: Performance comparison between SDHPC and other similar work.

Literature Title	3D or 2D electrode?	Journal Name/Year	Areal Capacity [mAh cm^{-2}]	Areal S-loading [mg cm^{-2}]	%S in electrode [%]	E/S [µL mg^{-1}]	Rate [C-rate]	Cycle Life [#cycle]
High Energy Density Lithium-Sulfur Batteries: Challenges of Thick Sulfur Cathodes[40]	2D	Advanced Energy Materials/2015	3.5	3.5	64	N/A	0.1C	100
Long-Life and High-Areal Capacity Li-S Batteries Enabled by a Light-Weight Polar Host with Intrinsic Polysulfide Adsorption[177]	2D	ACS Nano/2016	3.5	5	60	N/A	0.2C	50
A Comprehensive Approach toward Stable Lithium-Sulfur Batteries with High Volumetric Energy Density[170]	3D	Advanced Energy Materials/2016	14.7	14.9	65.45	3.5	0.05C	50
A High-Volumetric-Capacity Cathode Based on Interconnected Close-Packed N-Doped Porous Carbon Nanospheres for Long-Life Lithium–Sulfur Batteries[178]	2D	Advanced Energy Materials/2017	~6.5	5	59.5	6	0.2C	200
Cathode materials based on carbon nanotubes for high-energy-density lithium–sulfur batteries[179]	2D	Carbon/2014	3.21	3.72	49	N/A	0.2C	100
Compact high volumetric and areal capacity lithium sulfur batteries through rock salt induced nano-architectured sulfur hosts[51]	2D	Journal of Materials Chemistry A/2017	5.4	4	60.9	4	0.1C	100

Foldable interpenetrated metal-organic frameworks/carbon nanotubes thin film for lithium–sulfur batteries[180]	3D	Nature Communications/2017	~6.9	11.33	70	50	0.2C	50
Strings of Porous Carbon Polyhedrons as Self-Standing Cathode Host for High-Energy-Density Lithium-Sulfur Batteries[44]	3D	Angewandte Chemie/2017	6.23	8	63	N/A	N/A	50
Stringed "tube on cube" nanohybrids as compact cathode matrix for high-loading and lean-electrolyte lithium–sulfur batteries[175]	3D	Energy & Environmental Science /2018	~4.8	5.1	N/A	6	0.2C	300
Rational Design of Statically and Dynamically Stable Lithium–Sulfur Batteries with High Sulfur Loading and Low Electrolyte/Sulfur Ratio[173]	3D	Advanced Materials/2018	~41.4	46	70	5	0.1C	25
TiS$_2$−Polysulfide Hybrid Cathode with High Sulfur Loading and Low Electrolyte Consumption for Lithium−Sulfur Batteries[174]	3D	ACS Energy Letters/2018	10	12	65	5	0.2C	200
Designing Lithium-Sulfur Cells with Practically Necessary Parameters[203]	3D	Joule/2018	31	57.6	75	4.2	0.1C	200
Addressing Passivation in Lithium–Sulfur Battery Under Lean Electrolyte Condition[49]	2D	Advanced Functional Materials/2018	~2.76-3.68	3-4	64	5	0.1C	100
			6	5	63	7	0.05 then 0.1C	280
This work	2D	Advanced Materials/ 2018	7.2	6	63	7	0.05 then 0.1C	200
			9.6	8	63	7	0.05 then 0.1C	150

10	8	63	2.8	0.025 C	20

Operating at strict conditions appears to have been only partially mitigated by the design of SDHPC. Further design could incorporate stronger polysulfide adsorption capabilities and higher tortuosity. From our data, it appears that the lithium anode is an overarching problem in LSB that needs to be addressed. Many reports have been made on the problems and mitigation strategies of LMB.[53] However at strict conditions, the performance is very poor and in fact only a slightly superior/similar to the performance presented here but with commercially available (and ideally more stable/reliable) cathodes such as $LiCoO_2$.[62,204] Based on these research trends and our own data, we believe that it would be attractive to substitute the Li metal with another anode and eliminate the problem at the source.

Chapter 5: Li_2S sulfide cathode electrochemical activation *via* redox mediator generators

This chapter is reprinted in adopted form from a manuscript that has been published, with permission from Nature Communications under the Creative Commons Attribution 4.0 International License

M. Li, Z. Bai, Y. Li, L. Ma, A. Dai, X. Wang, D. Luo, T. Wu, P. Liu, L. Yang, K. Amine, Z. Chen, J. Lu, Electrochemically primed functional redox mediator generator from the decomposition of solid state electrolyte, 2019, 10, 1890.

5.1. Introduction

Metallic Li as an anode has been well established as a very challenging system to achieve good cyclability.[205] Since Li-S battery is in fact a Li metal battery, its commercialization is not only hindered by the challenges of the sulfur (oxidation state of zero, S_8) cathode, but also the challenging task of solving the Li metal anode, which is often overlooked. Recent work in the Li metal battery field have begun to appreciate the severity and complexity of the problem.[60] From these literature sources, it is clear that even if the problems of the cathode were to be solved, the Li metal anode for Li-S will likely become a new key bottleneck. Therefore, a natural solution is to enable alternative anodes possible for sulfur-based battery systems, effectively removing the associated problems of a Li metal anode cycled at strict testing conditions. With the Li metal removed, this type of battery will no longer be a Li-S battery but will be a Li-ion sulfur-based battery. Specifically, in sulfur-based, battery chemistries (with Li-ions as the main charge carrier), there two major subgroups configuration[64]:

1. *Lithium-sulfur battery:* Lithium-anode/S_8-cathode
2. *Sulfur-based Li-ion battery:*
    a. Pre-lithiated Non-Li-metal anode/S_8-cathode
    b. Non-Li-metal anode/pre-lithiated sulfur (Li_2S)-cathode

Without a Li metal as the anode, Li-ion must be sourced at either the alternative anode (Si, graphite, etc.[64]) or the cathode prior to the cell assembly. In this chapter, we chose Li_2S as the Li-ion source over prelithiating an anode material due to a few main reasons.

Firstly, there are many 3 main problems associated with prelithiating an anode: 1) Prelithiation, that is, the act of lithiating an electrode either chemically or electrochemically is non-trivial for many anode materials. As described in Chapter 1, chemical prelithiation typically involve mixing of what is known as stabilized lithium metal powder (SLMP). SLMP are polymer-wrapped Li-metal nanoparticles that are employed in powdered form over the un-lithiated anode. When pressure is applied (during the end of cell assembly), the SLMP are broken, exposing reactive Li nanoparticles surface area, which readily react (lithiate) with anode material.[206] However, this method offer no control over the rate of lithiation, which is critical to preventing the stress generation involved in the lithiation-induced volume expansion of many delicately designed high energy anode candidate (Si, Ge, etc.)[53] 2) Electrochemical prelithiation of anodes will require assembly of some sort of initial Li metal/Li-free anode "Lithiation cell". Li can then be controllably inserted into the anode based on current control. While this method yields more desirable stress management of high energy density anodes, the lithiated anode will have to be extracted from the "Lithiation cell" before assembly into the true usable cell with a sulfur-base cathode. Practically, this is very unlikely. 3) The electrochemical potential and as such the chemical potential of a lithiated non-lithium metal anode will be akin to that of metallic lithium. Therefore, lithiated anodes will hold logistical problems (compared to Li_2S) during manufacturing as it will be nearly as prone to spontaneous oxidation as metallic lithium.

Secondly, there are 2 main benefits of using Li_2S over S_8 as starting cathode material: 1) S_8 is prone to sublimation (at temperature as low as 70°C with a medium vacuum) due to its low intermolecular force, rendering it very difficult to completely dry a S_8-based electrode from its slurry state (removal of NMP-solvent). Furthermore, most S_8 hosts are required to possess some dipole throughout its surface area to promote adsorption of polysulfides (as described in Chapter 3), rendering them rather hygroscopic in nature. Together, the stray solvent and water molecule will react with any lithiated anode and will cause compromise cell performance in terms of Coulombic efficiency, cycle life and capacity 2) Li_2S can mitigate the volume expansion concerns of the S_8 electrodes.

With a specific Li-ion capacity of over 1100 mAh g^{-1}, Li_2S has drawn much recent attention in the research. While the benefits towards both achieving higher performance sulfur-based cathode and replacing Li metal as an anode are clear,[64] Li_2S presents a very high initial charge-activation barrier, which stems from the strong ionic bonds within its crystal, low Li-ion and electron transport properties and the nucleation barrier of forming solvated polysulfide species.[75] Such a hurdle (often reaching >4.0 V vs Li^+/Li) typically results in low specific capacity and electrolyte decomposition leading to poor cycle stability. Strategies used to solve these problems typically fall into two categories: carefully designed nano-sized Li_2S composite material [63,65] or electrolyte additive in the form of pre-solvated redox mediators.[75,207] While both of these strategies have shown significant progress in reducing the charge overpotential and achieving good overall performance, they also introduce significant disadvantages. Novel Li_2S composite materials typically require exotic synthesis environments composing of high temperatures or toxicity, while soluble redox mediators often introduced pre-solvated into the electrolyte will contribute to severe internal shuttling and inevitably depend on the volume of electrolyte used. Moreover, the commonly used excess amounts of high oxidation state polysulfides as redox mediators will result in an overall low amount of starting Li-ion from the cathode (for a full cell Li_2S-based LIB). An ideal solution to these challenges is the use of an initially dormant redox mediator that remains inactive during the electrolyte wetting process, effective at low mass ratios, separate from the electrolyte to decouple from the effect of electrolyte volume, and only activates when the first charge is initiated.

The class of sulfide-type solid electrolyte (STSSE) materials have gained significant interest among the solid state electrolyte community.[208-211] Their tendency to possess higher Li-ion conduction and possibilities of low temperature synthesis when compared to the next leading solid electrolyte material (garnet-type),[212] makes them one of the most promising candidate for solid-state batteries.[213] Recent research into the STSSE have placed a spotlight on the electrochemical stability of STSEE. Thermodynamically, STSSE are known to be unstable at the voltage range of interest for both cathode and anode electrodes.[214,215] Specifically, the nature of the interface layer (i.e. the degree and type of passivation) between the STSSE and active material strongly dictates the longevity of a solid state cell.[216,217] With so much knowledge gained on the decomposition process of STSSE, it is timely to examine cross-field applications of this phenomenon. Some of the thermodynamically predicted oxidation decomposition products (particularly in the case of redox active products[215,218,219]) of P and S containing STSSE can be useful for liquid battery systems where redox mediators are needed.[220] Furthermore, as these products are only produced when the STSSE is oxidized, it can present itself as an *in situ* generator of chemical species that can be “switched-on” at specific oxidation voltages. A highly applicable area for these functional redox mediators is the sulfur-based battery chemistries.[221,222]

In this chapter, we demonstrate that the oxidative decomposition of solid Li_3PS_4 (LPS), a solid-state electrolyte material, can be leveraged as an electrochemically “switched-on” redox mediator generator for lowering the 1st charge overpotential of commercial Li_2S. Crucially, the observed enhancements in performance was achieved with only the direct simple mixing of LPS into the slurry formulation at 10 wt. %. This is the first reported use of a solid material as a redox mediator source. We have shown that this material will not dissolve into the electrolyte unless activated and as such, less dependent on the volume of electrolyte used.

5.2 Experimental methods

5.2.1. Materials

All chemicals and molecular sieves (0.3 nm, rod shapes of 1/16 inch) were purchased from Sigma Aldrich. Molecular sieves were activated under vacuum at 120°C for 48 hours before use. 1,3 dioxolane (DOL) and dimethoxyethane (DME) was first dried with molecular sieves for 2 days. Lithium bis(trifluoromethanesulfonyl)imide (LiTFSI) and $LiNO_3$ was dried in a vacuum oven at ~120°C overnight prior to electrolyte mixing. All other chemicals were used as received if not otherwise stated.

5.2.2. Synthesis of Materials.

The synthesis of Li_3PS_4 (LPS) powder was conducted in a glove box with Ar atmosphere. High purity precursors of Li_2S (99.98%) (Aldrich) and P_2S_5 (99%) (Aldrich) were used as received, and anhydrous THF solvent (99.9%) (Aldrich) was pre-treated with molecular sieves to remove residual water before use. Li_2S (0.244 g) and P_2S_5 (0.394 g) powders were mixed in the dried-THF solution under stirring for 24 hours. The prepared solution was pre-dried in the furnace for 24 hours at 140 ℃ and then further dried in the vacuum oven for 24 hours at 140 ℃. The β-Li_3PS_4 phase of our sample was confirmed by Raman spectroscopy (**Figure 1a**),[223] X-ray diffraction (**Figure 1b-c**)[209] and X-ray photoelectron spectroscopy (**Figure 1d-e**).[224] Various amount of Li_2S and S were mixed at a constant relative ratio (always forming Li_2S_8) at various absolute amounts in a solution consisting of DOL/DME at 1 v/v at ~50 °C overnight, forming a dark colored solution of Li_2S_8 at different concentrations.

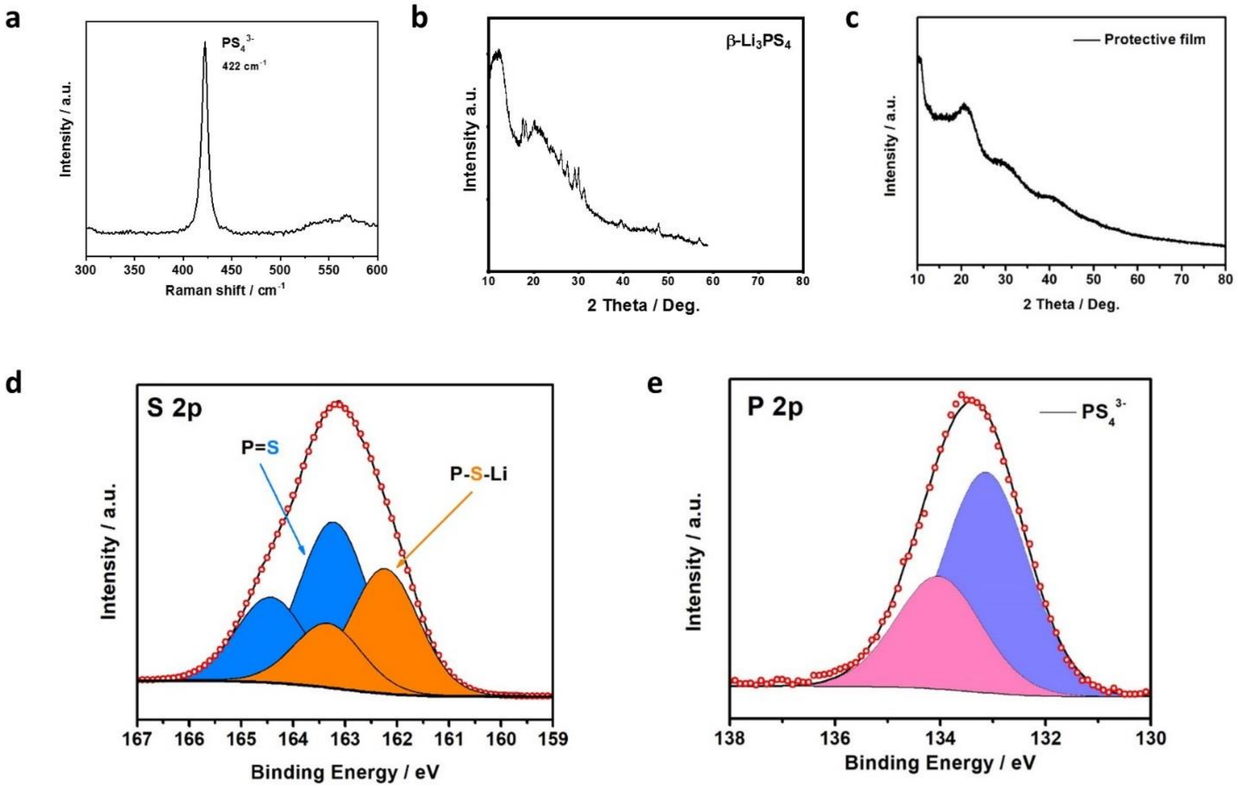

Figure 5- 1: Physical characterization of as-synthesized Li_3PS_4 a) Raman spectrum, b) X-ray diffraction of as-synthesized Li_3PS_4 protected with glass based air-tight sample holder, c) X-ray diffraction of the protective film without any samples, X-ray photoelectron spectroscopy at d) S 2p and e) P 2p of synthesized Li_3PS_4.

5.2.3. Electrochemical Characterization

First polyvinylidene fluoride (PVDF, dried in vacuum oven at 60°C overnight) in N-Methyl-2-pyrrolidone solution (NMP, dried with molecular sieves for two days and measured to be at ~5.1 ppm H_2O by Karl Fischer titration) was mixed with solid LPS, Li_2S and finally Super C45 carbon black (C45, from Timical) with a final solid content of ~15%. Typical ratios of Li_2S: LPS: C45: PVDF were 70:10:10:10 (10% LPS), 70:1:19:10 (1% LPS) and 60:10:20:10 (10% LPS with 60% Li_2S). For the control sample without LPS, the slurry composition was 60: 25: 15: for Li_2S: C45: PVDF respectively. All slurries were hand-mixed thoroughly in a mortar and pestle and blade casted to the desired thickness on an Al current collector. The electrode laminates were dried in a vacuum oven at 60°C overnight and punched into 16 mm diameter disks. The entire electrode fabrication process was conducted inside of an Ar-filled glove box with H_2O at <0.6 ppm and O_2 <0.5 ppm. CR2032 type coin cells were used for all electrochemical measurements with a Li chip as the counter and reference electrode. For *ex situ* X-ray absorption spectroscopy experiment, 0.5 $LiNO_3$ in DME/DOL (1:1 v/v) was used as electrolyte to prevent signal convolution from the sulfur present in LiTFSI. For the LiPS baseline experiments, 30 µL of 1M LiTFSI + 0.5 $LiNO_3$ in DME/DOL (1:1 v/v) electrolyte was first injected onto the side anode and the separator followed by the injection of 10µL of electrolyte pre-blended with predetermined amount/concentration of LiPS directly onto the cathode. This was done to ensure the proper contact of polysulfide with Li_2S and limit anode corrosion prior to 1st charge (providing the cells with the best chance for better higher performance). For all other electrochemical test, 1 M LiTFSI + 0.5 M $LiNO_3$ in DME/DOL (1:1 v/v) was used as the electrolyte. An 18 mm diameter 2320 Celgard membrane was used as the separator in all experiments. All galvanostatic cycling and rate performance tests were conducted with a Neware battery testing station. A 1400 CellTest System from Solartron was used to conduct cyclic voltammetry and electrochemical impedance spectroscopy (EIS). EIS was conducted at 40 minute constant current intervals followed by a 5 minute rest time prior to the EIS data collection.

5.2.4. Physical and Chemical Characterization

X-ray absorption spectroscopy experiments (operated under fluorescence mode) were conducted at the 9-BM of the Advanced Photon Source (APS) at Argonne National Laboratory (ANL). Cells were charged to their respective state of charge (electrolyte only containing 0.5 M $LiNO_3$ and without LiTFSI, to prevent signal convolution from the sulfur atoms in the TFSI anion) and quickly decrimped in an Ar filled glove box. The harvested electrodes were dried without rinsing and sealed with a Kapton film-based sample holder to prevent air contamination. The X-ray absorption spectroscopy experiment was conducted under He atmosphere. P_2O_5 and $Na_2S_2O_3$ were used as the calibration sample for the P and S K-edge respectively. Using different segments of the same harvested electrodes, Raman spectroscopy was performed on a Renishaw In-Via Raman spectrometer with a 785 nm wavelength laser. Samples were sealed in and measured through a polyethylene bag. X-ray diffraction was performed at the 11 ID-C (λ=0.01173 nm) of the APS at ANL. Samples were sealed in Kapton tape to prevent air contamination. To prevent electrolyte leakage/evaporation, electrodes submerged in electrolyte were sealed in a coin cell with holes bored through the center of the top and bottom coin cell cap and covered with Kapton to allow for X-ray penetration (nearly identical to the *operando* coin cells used in Chapter 4.

5.3. Results and discussion

5.3.1. Disadvantage of pre-solvated redox mediator: Lithium polysulfide.

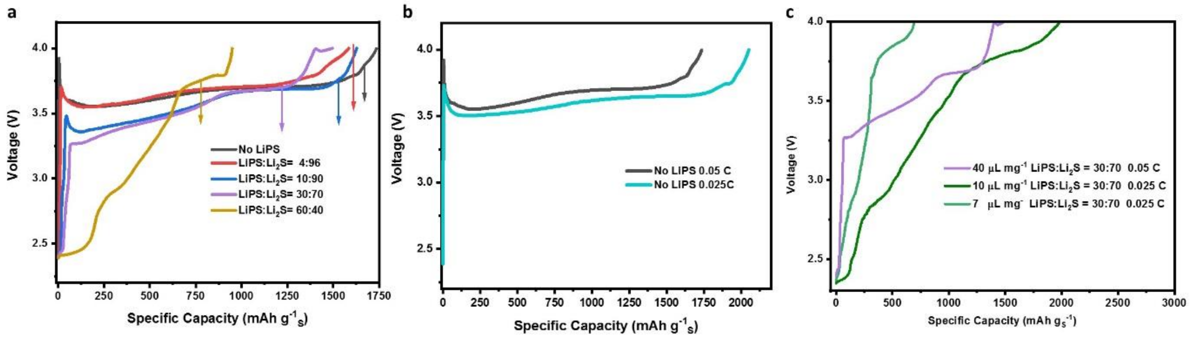

Figure 5- 2: Effectiveness of Li_2S_8 as Li_2S activation agent at various operating condition a) 1st charge voltage profile of 60% Comm-Li_2S loaded with varying amounts of Li_2S_8 in the electrolyte. Specific capacity is normalized to the total sulfur mass in both solid Li_2S and solvated Li_2S_8 mixture. Arrows indicate the theoretical delithiation capacity associated with each ratio of Li_2S_8:Li_2S. b) 1st charge voltage profile of pure 60% Comm-Li_2S electrode at 0.05 and 0.025 C. c) 1st charge voltage profile of commercial Li_2S at 30% Li_2S_8 and 40, 10 and 7 µL mg^{-1} electrolyte to equivalent S content at 0.05, 0.025 and 0.025C respectively.

Electrolytes preloaded with soluble redox mediators have been widely used as Li_2S activators throughout literature.[75,92,207] Taking lithium polysulfide (LiPS) as the representative additive, it is clear that the use of Li_2S_8 as redox mediator is only applicable when significant amounts of Li_2S_8 are added (**Figure 1a**, arrows indicates the theoretical amount of Li-ion that is extractable from each specific ratio of Li_2S to Li_2S_8). This in direct conflict with achieving high sulfur areal loading and low electrolyte content. For a 60% commercial Li_2S electrode, it was found that the ratio of Li_2S_8 to Li_2S must be raised to a relatively high (30-60 wt %) to achieve significant improvements to the charge voltage profile. It should be noted that this is not the result of a decreased current density (normalized to loaded Li_2S mass) as experiments at half the current still maintains a very high charge voltage (**Figure 1b**). It is important to remember that one of the most advantageous aspect of using Li_2S over S is its ability to serve as a source of Li-ions i.e. pairing with a Li-ion free anode and eliminating the need of using Li-metal. It is then foreseeable that the use of significant amounts of LiPS to activate Li_2S will result in a delithiated cathode with excess amounts of sulfur that cannot be lithiated in the subsequent cycle. Additionally, every sample with soluble polysulfide species experienced higher than theoretical charge specific capacity (theoretical indicated by arrow heads) likely suggesting shuttling.[184] This is particularly evident in cells (LiPS: Li_2S= 30:70) cycled at decreased current density (**Figure 1c**), yielding a 1st charge capacity of well over 2500 mAh g^{-1} normalized to the sulfur content even with 0.5 M $LiNO_3$. Finally, and most importantly, changes to the electrolyte to sulfur ratio also dramatically influences the chargeability of the electrode. When the total electrolyte content was tuned down to ~7 µL mg^{-1}_{Li2S} (10 µL mg^{-1}_{S}, maintaining a constant LiPS: Li_2S ratio), there is a dramatic decrease in specific capacity and increase in charge potential. Therefore, a Li_2S based LIB that utilizes polysulfide in amounts such that it serves as an efficient Li_2S activator at “strict” testing conditions such as low electrolyte conditions, will be unlikely.

5.3.2. Electrochemical properties of LPS and its application in commercial Li_2S cathodes.

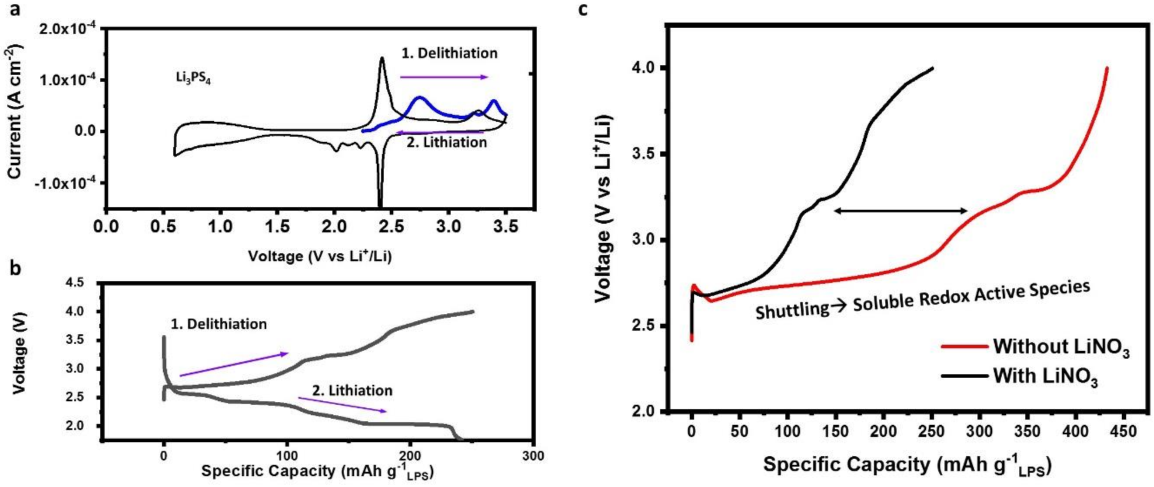

Figure 5- 3: Electrochemical Data of LPS Cycled in Liquid Ether Based Electrolyte a) Cyclic voltammetry of LPS with an initial anodic sweep (blue) and subsequent cycling in black, b) galvanostatic charge/discharge of LPS with $LiNO_3$ in electrolyte and c) 1st charge of LPS with and without $LiNO_3$ in electrolyte suggesting shuttling.

The specific LPS solid electrolyte composition have drawn a lot of interest due to its high ionic conductivity at room temperature and ease of synthesis.[209,225] The stability of LPS has been a topic of great concern in the field of solid electrolyte.[226-228] It is often considered that the electrochemical decomposition of LPS complicates its application as a solid-state Li-ion conductor. Due to its redox activity at a potential window similar to that of Li_2S,[215] it would be interesting to revisit the stability of LPS but in a liquid electrolyte setting. With a similar but slightly higher oxidation voltage than Li_2S, it could be a perfect source of redox mediators for Li_2S activation. However, this is only true of the decomposition products of LPS is redox active and reversible. **Figure 5-3a** displays the cyclic voltammograms of LPS in common 1,3 dioxolane/dimethoxymethane based Li-S electrolyte. A pronounced anodic peak is found at ~2.7

V and then at ~3.4 V during its initial delithiation sweep (in blue). The following cathodic and subsequent anodic sweep (in black) further demonstrated its redox activity in Li-S electrolyte. Corroborating this data, constant current delithiation of LPS at 0.1 mA mg^{-1} produces a sloped plateau from ~2.7-3.1 V (**Figure 5-3b**) followed by another plateau at ~3.2 V and 3.6- 4.0 V. While these results are intriguing and produced apparently more pronounced voltage profiles from traditional solid-states studies of LPS,[229] the most important phenomenon of LPS oxidative decomposition can only be revealed when charged without $LiNO_3$ present in the electrolyte. Cells charged with $LiNO_3$ yielded ~250 mAh $g^{-1}{}_{LPS}$ whereas cells without $LiNO_3$ (commonly used to prevent shuttling[230]) required more than 430 mAh g^{-1} (**Figure 5-3 c**) with a prolonged ~2.7-3.1 V sloped plateau. Furthermore, post cycling imaging (scanning electron microscopy, **Figure 5-4 a**) and elemental analysis (energy dispersive spectroscopy, Figure **5-4 b**) of the cycled Li metal counter electrode revealed a surface layer composed of both phosphorus and sulfur. Taken together, this provides strong evidence that the longer voltage plateau of the cell charged without $LiNO_3$ is due to shuttling of a soluble redox active species that are generated by LPS upon oxidative decomposition.

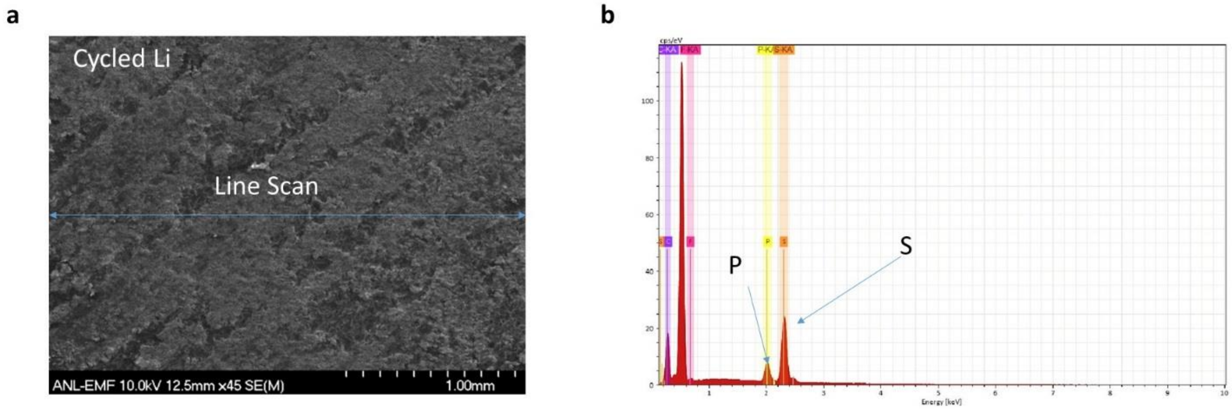

Figure 5- 4: Analysis of post cycling Li metal anode a) Scanning electron microscope image of cycled Li metal anode and b) the corresponding electron dispersive spectroscopy spectrum of the line-scan indicated in a).

With the generation of redox active species starting at 2.7 V (close to, but higher than the oxidation potential of Li_2S), LPS is an good candidate as a solid-sourced redox mediator generator that can be electrochemically "switch-on," dissolving into the electrolyte in parallel to Li_2S charging. We now demonstrate here that these decomposition products can be leveraged to enhance the electrochemical performance of cathodes based on even commercial micron-sized Li_2S (Comm-Li_2S) powder. By simply blending bulk LPS into the slurry formulation of Comm-Li_2S electrode, significant enhancements in the electrochemical properties were achieved. XRD of the casted and dried electrode (**Figure 5-5a-b**) indicates that the Li_2S is very much crystalline, producing pronounced diffraction peaks. Furthermore, the small peaks at the lower 2θ, persisted even while submerged in electrolyte (1M LiTFSI + 0.5 LiNO3 in DME/DOL (1:1 v/v)), indicating that LPS does not dissolve into anhydrous electrolyte formulations. However, it should be noted that the crystal structure of Li_3PS_4 changed after electrode fabrication as the XRD peaks have changed.

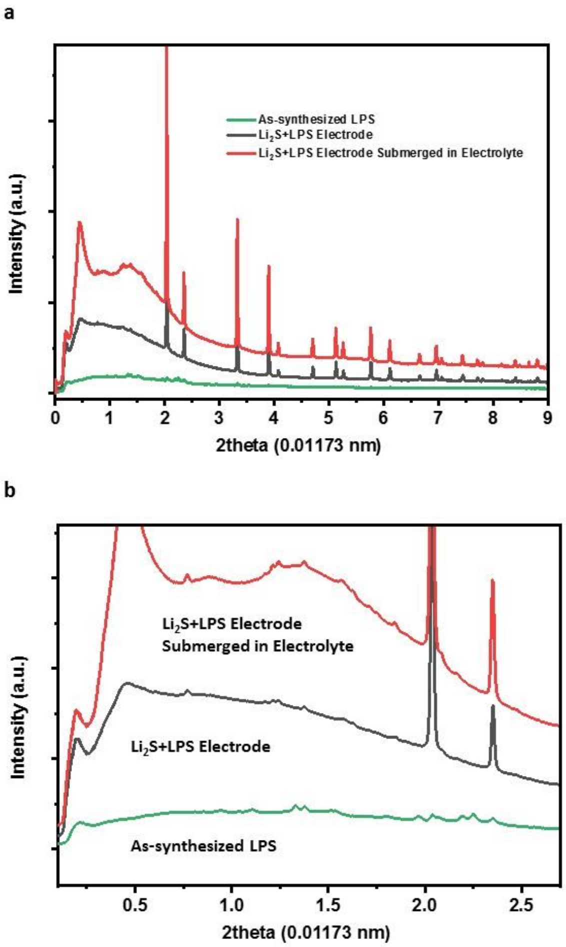

Figure 5- 5: Synchrotron high energy X-ray diffraction (λ=0.01173 nm) study of Li_3PS_4 at various stage of testing a) from $2\theta = 1$ to 9 and b) $2\theta = 0.1$ to 2.7 of as-synthesized LPS, Li_2S+LPS electrode (scraped off from Al current collector) and Li_2S+Li_3PS_4 electrode scraped off from current collector and submerged in electrolyte for 2 hours and remained submerged during XRD testing.

Figure 5-6a displays the cyclic voltammetry of fresh Comm-Li_2S electrode prepared with 1 and 10 wt. % LPS. Compared to the pure Comm-Li_2S, the charge overpotential was observed to decrease with increasing LPS ratio. Even at a minimal LPS ratio of 1 wt. %, an initial anodic peak was found at 3.5 V with a subsequent peak at 3.8 V which is lower than the ~4.0 required to obtain an oxidative peak for the pure Comm-Li_2S electrode. At 0.05 C, the charge voltage of Comm-Li_2S was dramatically decreased (**Figure 5-6b**) even with an increased Li_2S content. It is also worth mentioning that there appears to be a double activation peak as shown in **Figure 5-6c**. We believe the first is the initial "switching-on" process of LPS (which we will explain in the following part of this chapter) followed by its activation (2nd peak) of the bulk Li_2S assisted by the oxidation products of LPS. After the initial activation process, there is an initial plateau followed by a sloped second plateau and a third plateau at the higher voltage region. The segregation of these plateaus is likely related to the different activation processes of Li_2S with LPS. For example, the initial plateau could be due to the higher concentration of redox mediators while the second sloped plateau could be an indication of a gradual decline in redox mediator concentration.

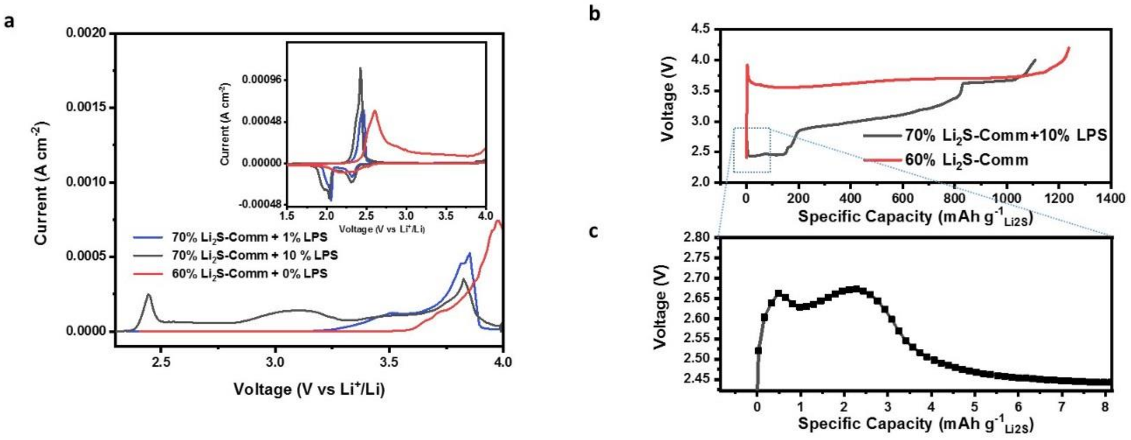

Figure 5- 6: First charge electrochemical properties of LPS blended into commercial Li_2S as an electrochemically "switched-on" redox mediator generator. a) Cyclic voltammetry of various combination of LPS and Li_2S-Comm, inset shows the subsequent cathodic→anodic sweep cycle after the initial anodic activation sweep, b) 1st charge voltage profile of electrode using 10% LPS with 70% Li_2S-Comm at C/20 with c) magnified view showing double peak.

5.3.4. The role of LPS in Li_2S activation.

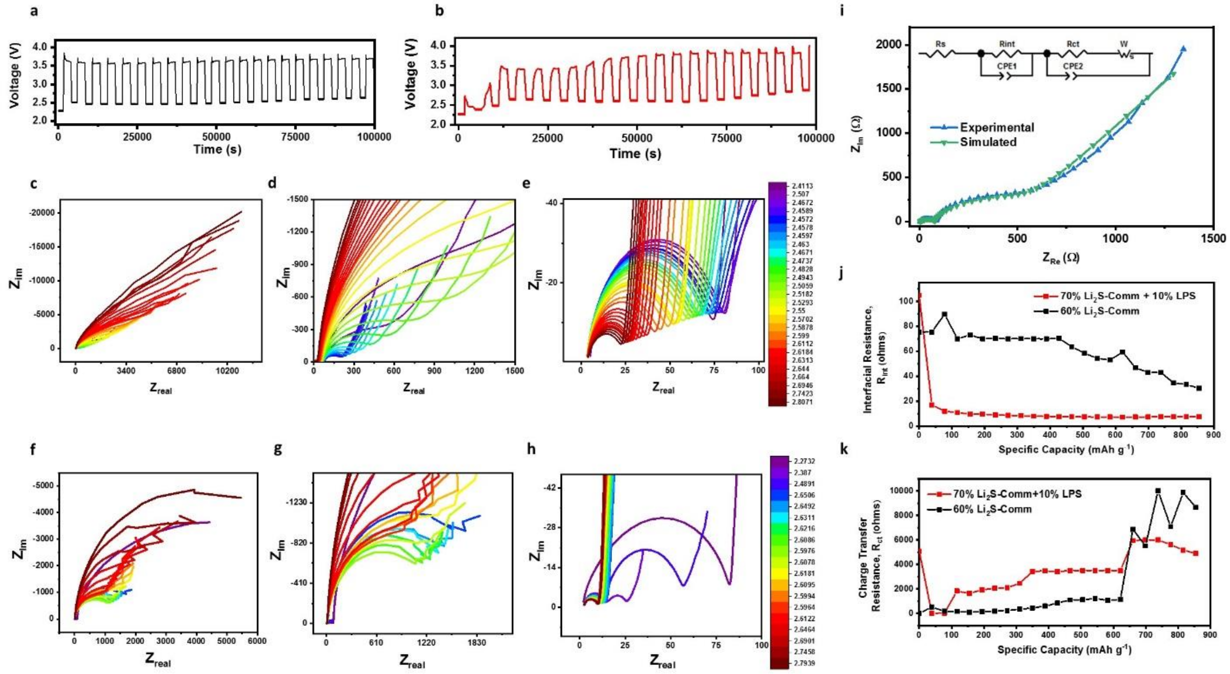

Figure 5- 7: Electrochemical Impedance Spectroscopy Study. Voltage profile of electrochemical impedance spectroscopy (EIS) experiment of a) the Li_2S-Comm electrode and b) the 70% Li_2S-Comm blended with 10% LPS electrode. c-d) Corresponding Nyquist plot of the Li_2S-Comm electrode and f-h) 70% Li_2S-Comm blended with 10% LPS electrode at different axis ranges. The color legend is labeled in volts. i) Example of experimental and simulated Nyquist plot j) interfacial resistance (high frequency semicircle) and k) plot of charge transfer resistance (mid frequency semicircle) of Comm-Li_2S (black) and with LPS (red).

Electrochemical impedance spectroscopy (EIS) reveals substantial differences between electrode with and without LPS. **Figure 5-7a-b** shows the voltage profile during the *operando* EIS experiment of Comm-Li_2S at 60% in black and Comm-Li_2S at 70% with 10% LPS in red, respectively. It should be noted that the voltage profile of the EIS process varies from the pure galvanostatic charge process likely due to the dynamic nature of soluble species created. Although EIS processes have been considered mostly non-invasive in most studies, this result reveals a clear reduction in effectiveness in LPS's activation of Li_2S. Furthermore, there also appears to be an apparent requirement of the pure Comm-Li_2S cells to reinitiate its activation process with a sharp peak after each EIS data collection session (Figure **5-7**a). This shows that the activation process of Li_2S is very time dependent likely with concurrent processes competing for polysulfide (out-of-cathode diffusion and anode corrosion).[231]

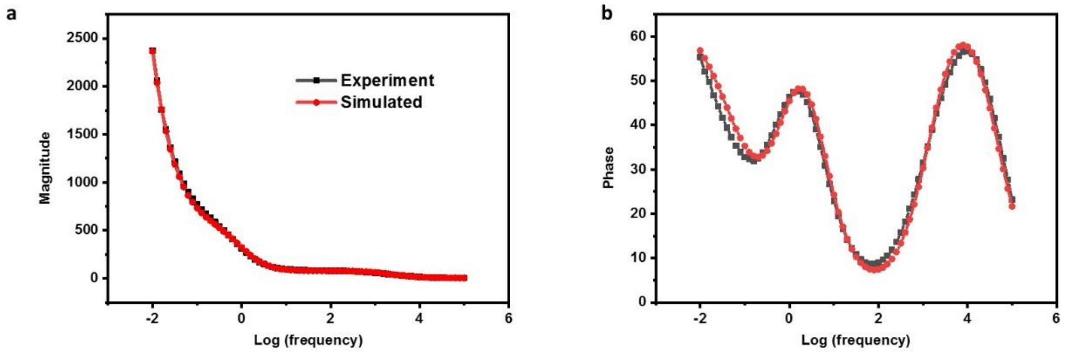

Figure 5- 8: Example of experimental and simulated electrochemical impedance spectroscopy plots a) magnitude and b) phase bode plot of Li_2S 60% commercial electrode with simulated and experimental data points in red and black respectively. c-d) Experimental EIS spectrums of Comm-Li_2S electrodes and f-h) of Comm-Li_2S electrodes blended with 10% Li_3PS_4 at different axis ranges. Unit of color legend is in volts.

Regardless, important differences in impedance are still observed. The Nyquist plot of the collected EIS data of pure Li_2S-Comm electrode is shown in **Figure 5-7c-e** and of the 70% Li_2S-Comm blended with 10% LPS electrode in **Figure 5-7f-h**. As the impedance features of this material varies significantly with frequency, different axis range/magnifications are shown for clarity. Consistently throughout the 1st charge, a small semi-circle was found at the high frequency range followed by a very large mid frequency semi-circle which we allocated to interfacial and charge transfer resistance respectively according to previous temperature based studies.[97] Based on this, all Nyquist plots were fitted as shown in **Figure 5-7i** (corresponding representative simulated and experimental Bode plot can be found in **Figure 5-8a-b** respectively**.** Each impedance spectrum was fitted to the circuit shown in inset of Figure 2i.[46,63,192,232] Initially, the interfacial resistance appeared to be higher for the cells with LPS (**Figure 5-7j**). This could be attributed to the higher ratio of non-conductive material (LPS and Li_2S) to carbon as the Li_2S content is 70% in the electrode containing LPS whereas the electrode without LPS has only 60%. Interestingly after the initial activation process, the interfacial resistance of the LPS containing electrode dropped drastically from ~105 Ω to ~10 Ω. This is in contrast to the pure 60% Li_2S electrode where it exhibited only a modest decrease throughout the course of charge. Additionally, the charge transfer resistance (mid frequency semi-circle) initially started higher once again for the LPS containing electrode but was exceeded by the pure Li_2S electrode near the end of the charge period (~650 mAh g^{-1}) as shown in **Figure 5-7k**. This is intriguing because the enormous charge transfer resistance of the LPS containing electrode is not reflected in the charging voltage profile. This contradiction can be explain the dynamic nature of the Li_2S activation process. As the impedance spectroscopy was taken at potentiostatic conditions after a rest period (i.e. spectrum collection voltage is close to OCV at each specific state of charge), the resulting current response oscillates around near 0 mA. This suggest that there is a very strong dependence of the charge voltage on the presence of an applied current. It is further intriguing that for the pure Li_2S electrode, after each rest period and subsequent EIS spectrum analysis, there is a reactivation process indicating a depletion of polysulfide from the previous current-halt period (rest time and EIS analysis). This is not present in the first ~400 mAh g^{-1} of charge for the electrodes with LPS. Accordingly, the contradiction between the higher charge voltage and lower apparent impedance of the LPS containing electrode is likely due to good charge transfer kinetics of polysulfide and its role in the comproportionation reaction with Li_2S.[233] However, because there is a constant need of the pure Comm-Li_2S electrode to generate polysulfide species that are quickly consumed (by other polysulfide competing processes[231]). This creates a situation where the polysulfides cannot properly react with the remaining Li_2S and as such, the voltage remains high. Whereas in the case of the LPS containing electrode, the lack of an activation process after each EIS analysis indicates significantly higher amounts of soluble mediators that are generated with longer lifetime, serving a more prolonged role in mediating the charge process of the bulk Li_2S particles.

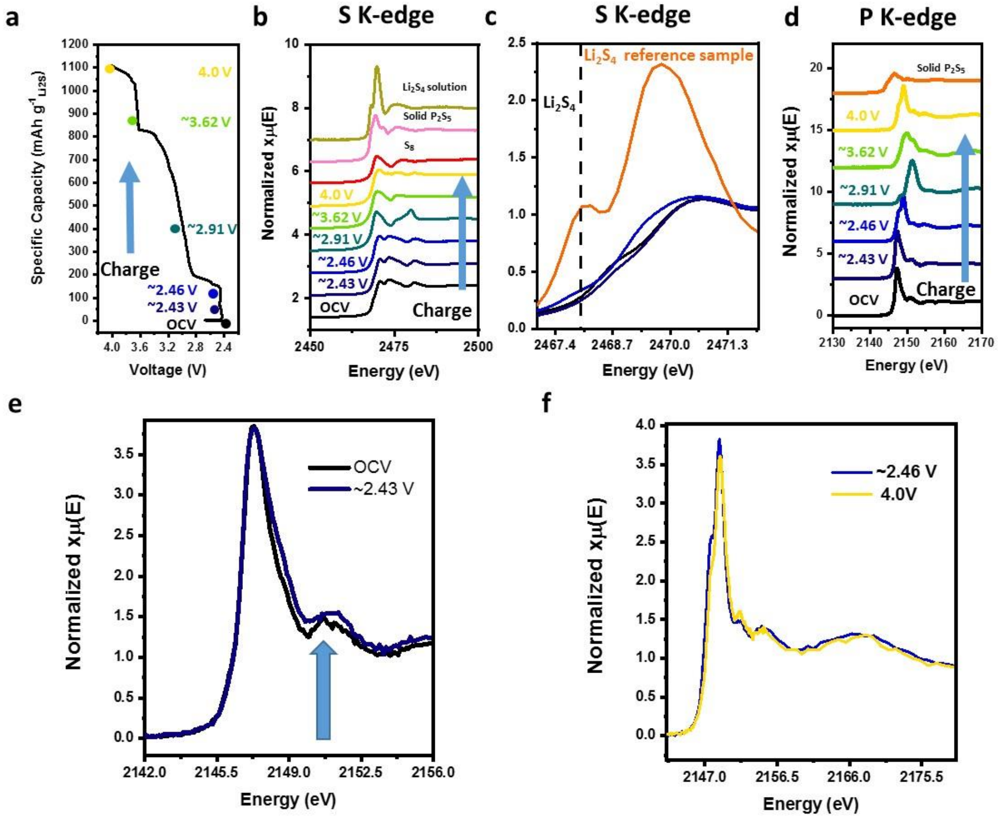

Figure 5- 9: Ex situ X-ray Absorption Near Edge Spectroscopy study of LPS containing Li_2S electrodes at various voltage throughout the first charge. a) Voltage profile of the 1st charge (0.05 C) of 70% Li_2S-Comm+10%LPS where the circles indicates the specific capacity/voltage at which each Ex situ XAS measurement was conducted. b) S K-edge of electrode taken at different state of charge with spectra of homemade Li_2S_4 solution, commercial P_2S_5 and commercial S_8 as reference. c) Magnified S K-edge of electrode opened at: fresh and ~2.46 V. d) P K-edge of electrodes taken at different state of charged in addition to commercial P_2S_5 as reference. e) Overlay of P K-edge at OCV and ~2.43 with the arrow indicating the increase in near edge features and f) ~2.46 V and 4.0 V displaying highly similar features at the beginning (~2.46 V) and end of charge (4.0 V).

In an attempt to clarify the mechanism of LPS on the charging process of Li_2S, *ex situ* XANES was conducted. As indicated on **Figure 5-9a**, 6 spectra were measured at different state of charges. Specifically, cells were disassembled and analyzed at open circuit voltage (OCV= ~2.42 V), ~2.43 V, ~2.46 V, ~2.91 V, ~3.62 V and 4.0 V. Overall, the S K-edge was found to change considerably over the course of the first charge (**Figure 5-9b**). From OCV to ~2.46 V, the overall characteristics of the S K-edge remained relatively the same where the convex shape of the Li_2S align well with literature.[234] However, in the magnified view (**Figure 5-9c**), it can be seen that the polysulfide shoulder (~2468 eV, matching our polysulfide standard measurement) increases from the fresh cell at OCV (Figure 8c, black curve) to the cell at ~2.46 V (Figure 5-9c, blue). Interestingly, the polysulfide species were not detected at the lower state of charge of ~2.43 V (Figure 5-9c, dark blue), whereas a change in the P K-edge was detected early in the charge process (~2.43 V, **Figure 5-9d-e**). This strongly suggests that the initial activation process of Li_2S is not due to the formation of polysulfide[234] At higher voltages (~3.62 V), the spectrum largely resembles that of the sulfur standard sample (Figure 5-9b) where the convex shape of Li_2S changes to concave at ~2474 eV as previously reported.[234] In fact, the convex shape of Li_2S cannot be found even at ~2.91 V, suggesting that a large majority of it has been consumed i.e. likely successfully charged.

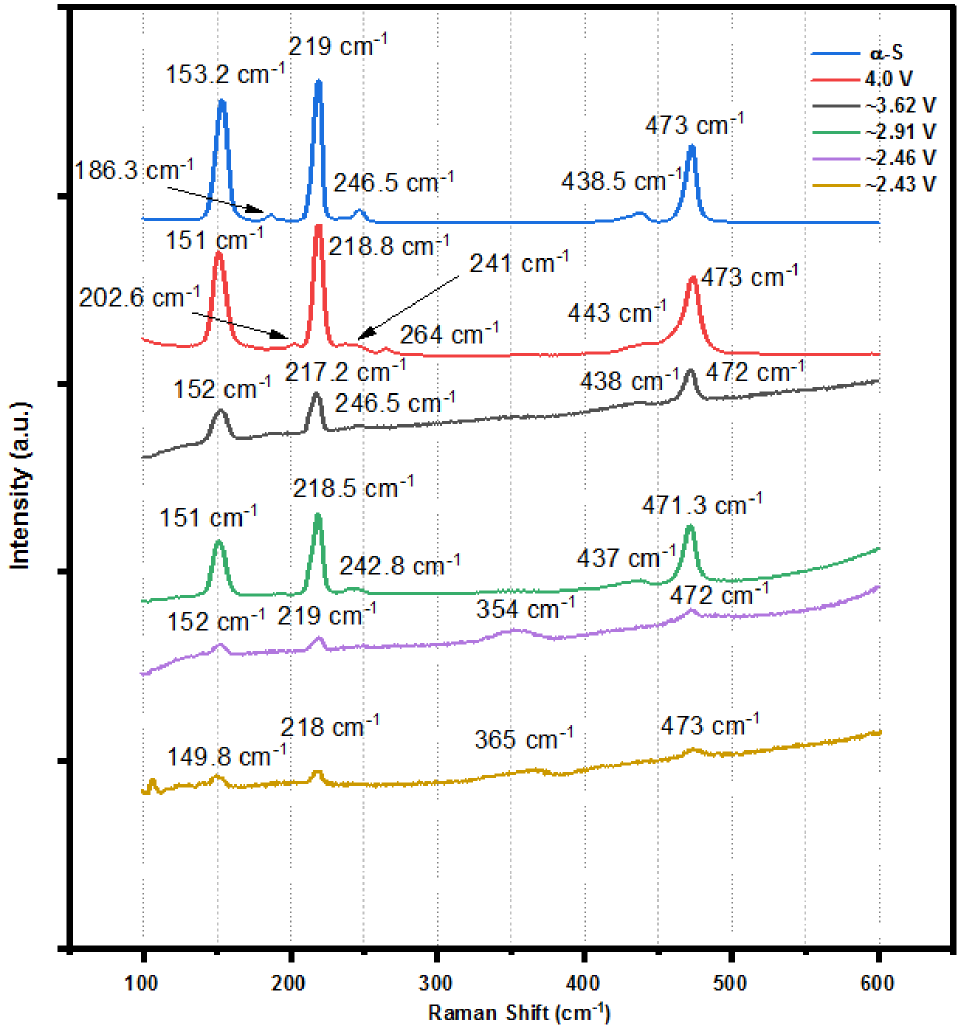

Figure 5- 10: Normalized Raman spectrum of Commercial S standard powder and Li$_3$PS$_4$+Li$_2$S electrodes charged to different voltages.

This is also seen in the *ex situ* Raman spectroscopy (**Figure 5-10**) of the same electrodes where the peak at ~365 cm^{-1} (likely Li$_2$S) shifts to 354 cm^{-1} from ~2.43 V to ~2.46 V whereupon it completely disappears at voltages above ~2.46 V. At 4.0 V, the spectrum further evolves into a shape different to that of the S$_8$ standard sample. The origin of this pattern is however unclear but we believe it might be some phosphorus based sulfur species superimposed by elemental sulfur signals as theoretically predicted by the high voltage decomposition of Li_3PS_4.[215] Surprisingly, the P K-edge of the sample at 4.0 V did not exhibit features similar to the P_2S_5 standard (Figure 5-9d). This is also seen in the Raman data where the originally formed ~246.5 cm^{-1} at the ~3.62 V transforms into a double peak centered at ~241 and 264 cm^{-1} at 4.0 V (Figure 5-10), not present in the commercial orthorhombic sulfur sample.[235] It is worth noting that P_2S_5 is one of the thermodynamically predicted oxidation products of LPS at high voltage.[215]

It is important to point out the difference between our XANES data and other previous reports on the delithiation of LPS in a solid-state configuration.[229] While the initial P K-edge features of our original OCV samples are near identical (Figure 5-9e) to literature, the XANES feature differed quite drastically upon delithiation in our work. In the more conventionally tested solid-state configuration, the P K-edge was reported to remain mostly constant throughout delithiation with only decrease in the edge-peak height coupled with a general increase of the broad peaks at higher energy levels. Interestingly, an analogous process of decreasing the synthesis molar ratio of Li_2S:P_2S_5 (LPS, molar equivalent of 75 Li_2S: 25 P_2S_5) i.e. decreasing the proportion of Li, have also been reported to yield a similar decrease in peak height.[236] In contrast to these works, the P K-edges in this work (Figure 5-9d) exhibited a complete edge shift towards a higher energy level of electrodes harvested from OCV to ~2.91 V and then an edge shift back to a lower energy level from ~2.91 V to 4.0 V, in addition to significant changes in the spectrum’s shape at the near edge. Only in the initial stage of charging did the P K-edge exhibits a slight increase in the near edge features and decrease in edge height (Figure 5-9e) similar to the aforementioned literature. The spectrum taken at ~2.46 V already reveals a major change in shape, suggesting changes to the bonding environment of P have occurred.

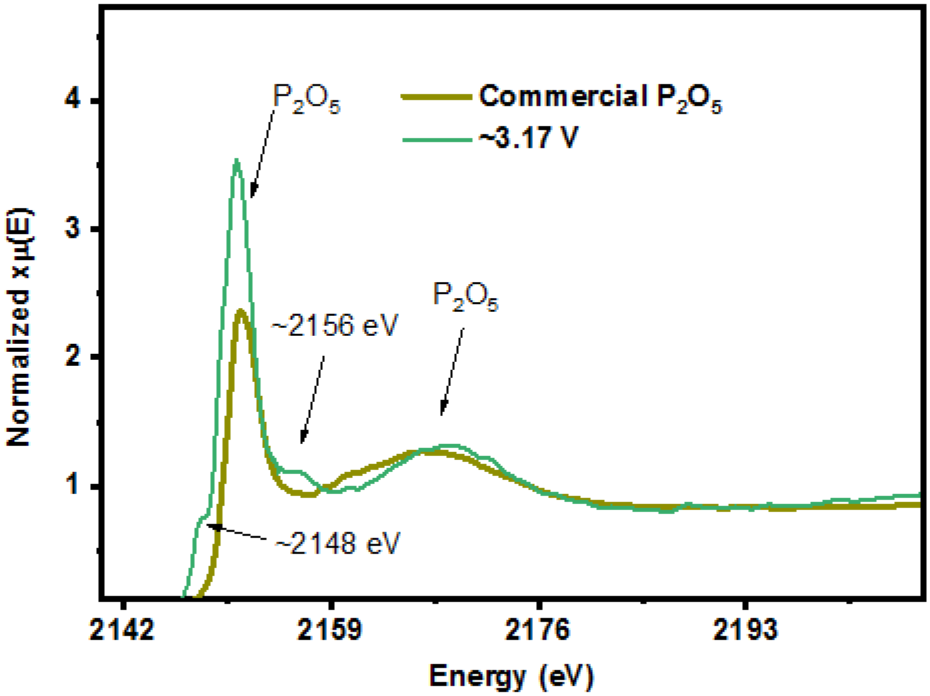

Figure 5- 11: Comparison of P K-edge spectrum of ex situ cell taken at ~2.91 V and the P_2O_5 standard sample.

Subsequent sample measurements at higher charge voltages continued to produce pronounced changes to both the edge position and shape. The peak features at ~2151 and ~2167 eV might be related P_2O_5 present in the sample as shown in the comparison with commercial P_2O_5 experimental data (**Figure 5-11**). As both peaks are consistently present among all the P K-edge spectrum, one might claim it is due to air contamination during measurement. However, the complete dominance of these higher energy peaks at ~3.17 V and its shift back towards lower energy levels for spectra taken at ~3.62 V and ~4.0 V might indicate that this is not solely due to air contamination. Conversely, we believe the peak at ~3.17 V is related to the voltage and charging process of Li_2S with LPS. Since chemical reactions between Li_3PS_4 and S_8 have been reported in literature, where the physical mixing of LPS with S_8 have yielded Li polysulfidophosphates.[237] We propose that the higher energy levels observed from electrodes harvested at ~2.91 to ~3.62 V is due to some bonding of P with long-chained S species. With more sulfur species attached to each P atom, the electron density should shift away from P, subsequently increasing the excitation energy required for the P 1s core level. It should be noted that this is only our interpretation of our data and another chemical process could be occurring. Regardless of the true chemical interaction mechanism of LPS, even more interesting is that at the end of charge i.e. spectrum taken at 4.0 V, the XANES almost reverts completely back to the features of at ~2.46 V (**Figure 5-9f**). This suggests that the decomposed LPS performed a catalytic role. Because it does not revert to the same form as the spectrum taken at OCV or ~2.43V, we believe the observed edge shifts toward a higher energy level for electrodes harvested from OCV to ~2.43 V could be an indication of an initial priming ("switching-on") process of the LPS.

5.3.5. Proposed Mechanism.

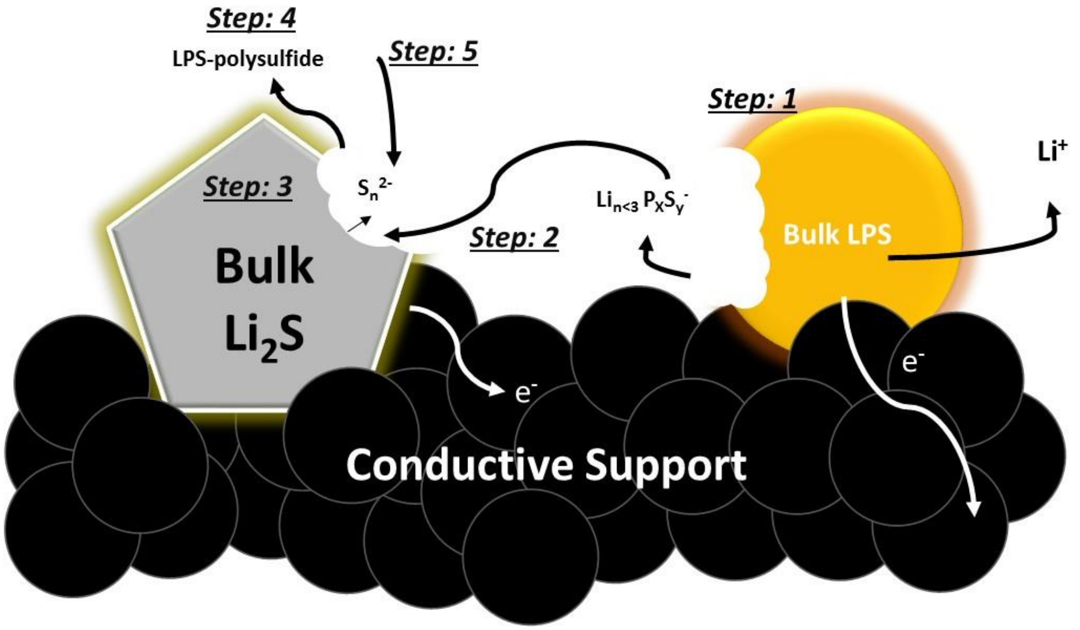

Figure 5- 12: Schematic of proposed Li_2S activation mechanism. Step 1: LPS is delithiated generated soluble redox active P,S-based species. Step 2: These species diffuse to the surface of bulk Li_2S where it (Step 3) reacts via comproportionation. Step 4: The delithiated LPS form some of reversible compound with polysulfide. Step 5: The LPS-polysulfide compound is then used to further comproportionation with Li_2S.

From our experiments, it appears that overall, the LPS initially delithiated, i.e. "switched-on", producing soluble redox active products and activating Li_2S as shown in *Step 1* of the schematic drawn on **Figure 5-12**. The soluble redox active products then migrated to the bulk crystalline Li_2S (*Step 2*) where it helped generate polysulfide species (*Step 3*). This is also supported by the double activation peak shown in Figure 5-6c. To follow, we believe the P from the delithiated LPS bonded with sulfur based species (likely high ordered polysulfides, *Step 4*), stabilizing the polysulfides for subsequent use in comproportionation reactions with the remaining Li_2S particles

(*Step 5*). When taken together with the differences in the EIS voltage profiles, we believe some of the formed delithiated LPS-polysulfide is likely to offer a longer redox-active lifetime over the typical polysulfide species as there is no need for the reactivation of any species after each EIS data collection period. At higher voltages, the long chained polysulfide species detach from the LPS *via* the oxidation of high order polysulfide to elemental S_8 (Figure 5-7b at ~3.62 and 4.0 V), where the P K-edge begins to shift back to the lower energy level and finally back to the same edge energy level and features as the ~2.46 V spectrum at the end of charge (Figure 5-9e). This indicates some form of catalytic role of the LPS generated species in the charging process of Li_2S.

5.3.6. Electrochemical performance at strict conditions

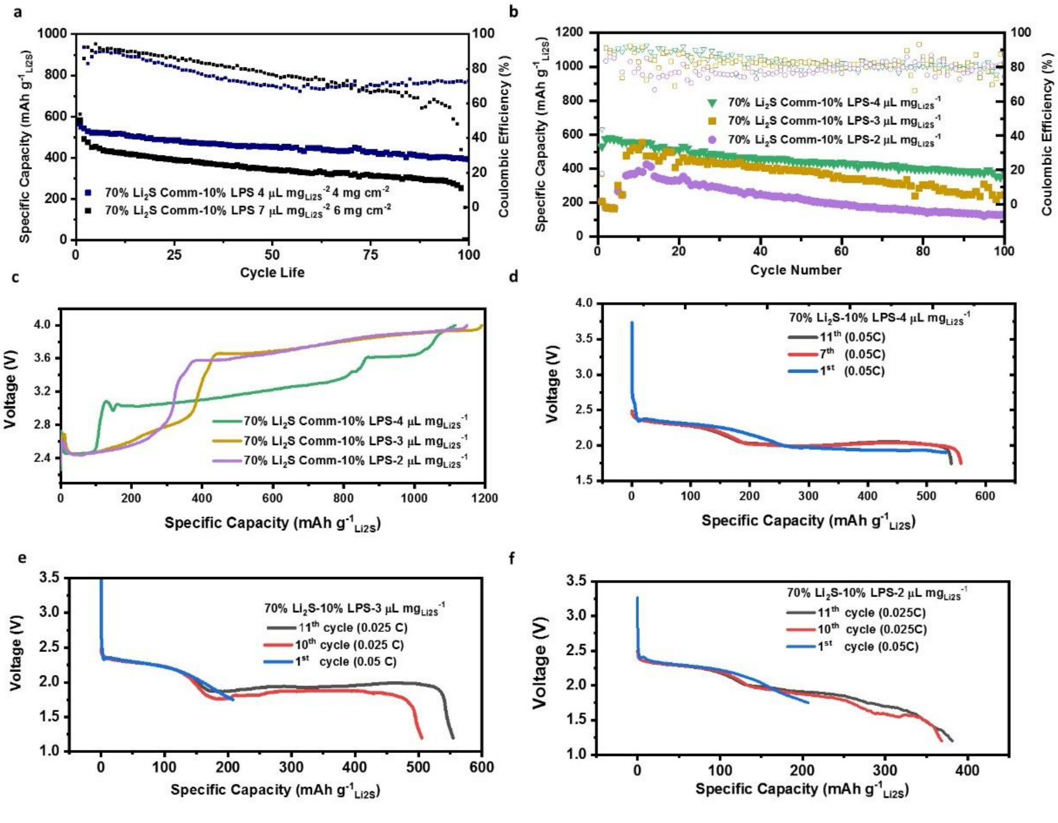

Figure 5- 13: Electrochemical performance with LPS added as an electrochemically "switched-on" redox mediator generator a) Cycle performance of 70% Li_2S-10% LPS at, 4

mg cm^{-2} (4 µL mg^{-1}) and 6 mg cm^{-2} (7 µL mg^{-1}), b) cycle performance and c) charging voltage profile of 70% Li_2S-10% LPS electrode at 1.5 mg cm^{-2} at various electrolyte content (4-2 µL mg^{-1}), and d-f) discharge voltage profile of 70% Li_2S-10% LPS electrode at 1.5 mg cm^{-2} at 4, 3 and 2 µL mg^{-1} respectively.

Half-cell cycling performance of LPS containing electrodes exhibited reasonably good performance at strict conditions (low electrolyte ratio and high mass loadings)especially for an electrode mainly based on only commercial bulk Li_2S. **Figure 5-13a** shows the cycle stability of 70% Li_2S -10% LPS electrode at various mass loading and **Figure 5-13b** shows the cycle stability at various electrolyte content. With decreasing electrolyte content from 4 to 2 µL mg_{Li2S}^{-1} (5.72 to 2.86 µL mg_{Li2S}^{-1}) an obvious and expected increase in charge potential is observed (**Figure 5-13c**) with corresponding decreases in the discharge potential and capacity as shown in **Figure 5-13d-f**. Cells at particularity low electrolyte content (3-2 µL mg_{Li2S}) required lower current density (0.025 C) to achieve discharge.

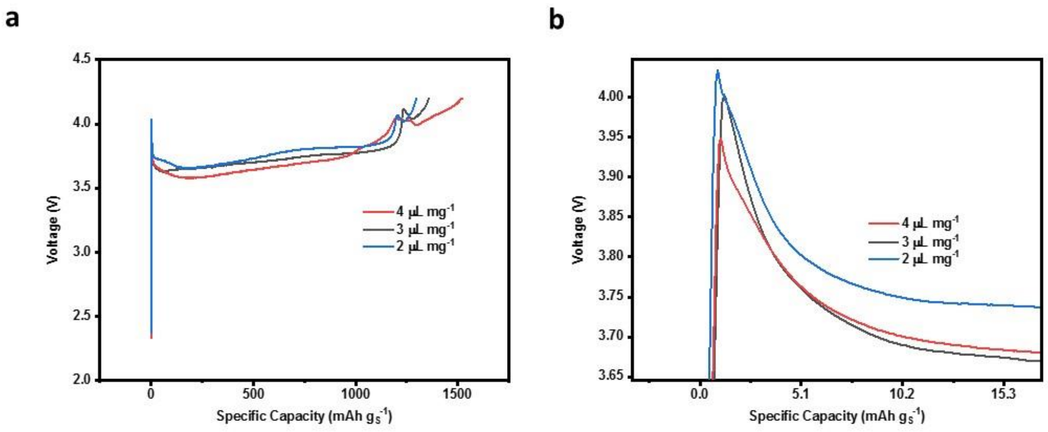

Figure 5- 14: Electrochemical properties of commercial Li_2S without Li_3PS_4 a) 1st charge voltage profile of 60% Comm-Li_2S at 4-2 μL mg^{-1} at 1.5 mg cm^{-2} and b) enlarged figure to show initial activation process.

We would also like to emphasize the particularly high Li_2S content in the electrode (70%) in comparison to other works of elaborate material structural design.[238] [239,240] In contrast, pure Comm-Li_2S cells even with 60% Li_2S were only able to charge when activated past 4.0 V (0.025C) at such low electrolyte ratios as shown in **Figure 5-14a-b**. Furthermore, as demonstrated in Figure 5-1b, polysulfide-based activators demonstrate a similar problem, with significant increases in voltage and simultaneous decrease in charge capacity. This demonstrate the importance of our solid-sourced redox mediator as a direction for future research. It is expected that with enhancements in the field of anode protection or separator/interlayer engineering[231,241] beginning to build traction, the performance can be significantly enhanced in subsequent work. Furthermore, future research into the direction of solid-sourced redox mediators based on other well-established solid-state electrolyte systems[242-244] coupled with a deeper mechanistic understanding via *in situ* experiments[245,246] will likely further increase the performance. Future improvements in capacity, reduction in 1st charge potential (related to the oxidative decomposition potential of the specific STSSE) while offering additional decoupling from the effects of low electrolyte content can be expected.

5.4. Conclusion

In summary, we have demonstrated here a method to leverage the commonly known oxidative decomposition of P, S based solid state electrolyte material in Li_2S batteries. As an electrochemically “switched-on” redox mediator generator, we have introduced the first ever solid-sourced redox mediator for the activation of commercial bulk Li_2S without the need for ball milling or high energy treatment for electrode fabrication. By simply hand mortaring Li_2S with LPS, substantial decrease in the charging potential is observed. Results from electrochemical impedance spectroscopy and X-ray absorption spectroscopy indicates a disappearance in LPS material during the beginning of charge, followed by the formation of high resistance material likely to be sulfur. Furthermore, we believe there exist some bonding between the P and polysulfide species leading to the creation of redox active species that have a longer life time during operation, allowing more opportunity for comproportionating with Li_2S. Good cycle performance was also demonstrated at low electrolyte content and reasonable Li_2S mass loading with electrodes at 70% Li_2S.

However, the activation of Li_2S at low electrolyte (3-2 $\mu L\ mg^{-1}{}_{Li2S}$) did not yield desirable voltage characteristics. Most of the charging profile was above 3.6 V vs Li^+/Li, which might cause electrolyte decomposition. In the next chapter, to further decrease the charge overpotential, we continued with the concept of a redox mediator generator but instead looked towards Na_2S.

Chapter 6: Na_2S as redox mediator generator for activating bulk Li_2S

This chapter includes content from the following draft in preparation

M. Li, J. Shi, Q. Li, X. Bi, S. Son, D. Luo, I. Bloom, K. Amine, Z. Chen, J. Lu, In situ polysulfide injector for the activation of bulk lithium sulfide. (2020) In preparation

6.1. Introduction

As mentioned in the previous Chapter, Li_2S sulfide as an alternative Li-ion source for sulfur-based batteries have received considerable attention in the past years.[247,248] While LPS was an insightful initial step towards Li_2S cycled at strict conditions, it is very much a foreign chemical with the fate of its phosphorus-based oxidation product unknown after first charge. This can lead to further complication later in development. Moreover, as LPS is only effective down to 10 wt.% with 60 wt.% Li_2S, its application is still limited as it compromises capacity. In Chapter 6, we look to apply a solid-sourced redox mediator generator that functions at lower proportions and has redox mediating species that are more native to sulfur-based electrochemistry. That is, a polysulfide generator at lower voltages. To properly select this material, we return to discuss the charge process of bulk Li_2S.

Fundamentally, the 1st charge mechanism of bulk-Li_2S involves the delithiation of its outer particle surfaces and the subsequent generation/nucleation of high order polysulfide species. [75,249] It has been identified that these polysulfide species likely perform comproportionation reactions with the remaining Li_2S, essentially acting as redox mediators (RM). Accordingly, the use of pre-solvated polysulfide solution and foreign RMs was demonstrated to decouple the poor bulk conductivity (both ionic and electronic) of Li_2S from its delithiation process.[92,250] However, adding pre-solvated RM will not only complicate the electrolyte formulating process, but also the mandates a certain RM concentration. The concentration of the RM will determine its effectiveness in Li_2S activation. Unfortunately, because pre-solvated RMs are homogenous in nature, the majority of the added RMs are essentially useless as they are spatially much too far from the bulk Li_2S to be functional. The use and effectiveness of pre-solvated RMs are limited when tested under strict electrolyte conditions.[251]

In this chapter, we propose the use of commercial Na_2S as an *in situ* electrochemical polysulfide injector. As shown in **Figure 6-1,** this entity injects polysulfide species at a reduced voltage during the charge process and facilitates the low charging of bulk Li_2S. By taking advantage of the naturally lower thermodynamic redox potential of Na_2S (Na_2S at <1.5 V vs Na^+/Na[252] against Li_2S at 2.1 V vs Li^+/Li). We demonstrate that the direct bulk mixing of Na_2S (at 1-3 wt. % in electrode) into a 70 wt. % commercial bulk-Li_2S can serve as an efficient solid-sourced redox mediator generator.

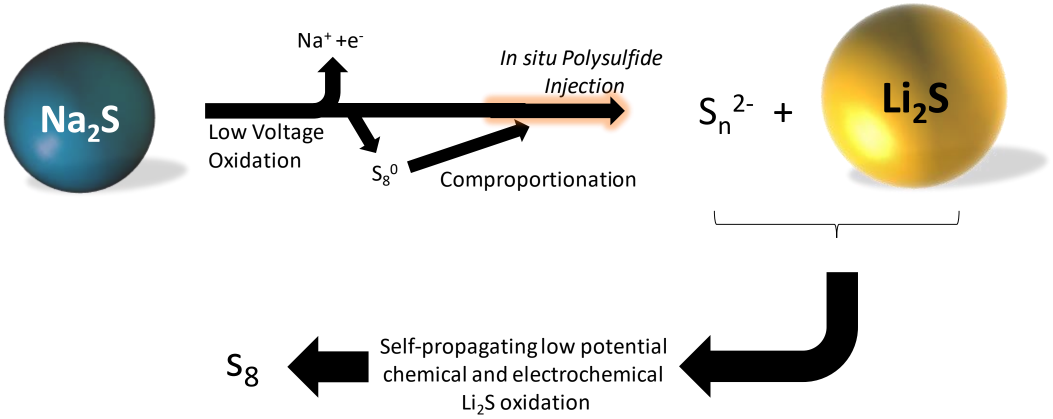

Figure 6- 1: Proposed mechanism of *in situ* electrochemical polysulfides injection

6.2. Experimental methods

6.2.1. Materials:

All chemicals and molecular sieves (0.3 nm, rod shapes of 1/16 inch) were purchased from Sigma Aldrich. Molecular sieves were activated under vacuum at 120°C for 48 hours before use. 1,3 dioxolane (DOL) and dimethoxyethane (DME) was first dried with molecular sieves for 2 days. Lithium bis(trifluoromethanesulfonyl)imide (LiTFSI) and $LiNO_3$ was dried in a vacuum oven at ~120°C overnight prior to electrolyte mixing. All other chemicals were used as received if not otherwise stated.

6.2.2. Electrochemical characterization:

First polyvinylidene fluoride (PVDF, dried in vacuum oven at 60°C) in N-Methyl-2-pyrrolidone (NMP, dried with molecular sieves for two days) solution was mixed with solid Na_2S, Li_2S, mesoporous carbon (MC) from Sigma Aldrich (SKU: 699632) and finally C45 carbon black (purchased from Timcal) with a final solid content of ~15%. The purchased Na_2S came in large centimeter-sized particles, which were dry-grinded with a mortar and pestle prior to slurry formulation. The slurry ratio was Li_2S: Na_2S: C45: MC: PVDF were 70: x: 2(20-x)/3: (20-x)/3:10 where x =1 or 3. For the control sample without Na_2S, the slurry composition was 70: 40/3: 20/3: 10: for Li_2S: C45: MC: PVDF respectively. The mass ratio of C45: MC was kept at 2:1. The solid mixture of Li_2S, Na_2S, C45 and MC were thoroughly hand-grinded with a mortar and pestle without any solvent. This powdered mixture was then added to an appropriate amount of PVDF dissolved NMP and further mixed with a planetary mixer and blade casted on carbon paper (areal mass of carbon paper is ~5.5 mg cm^{-2}, similar to that of a 20 µm Al foil at ~5.4 mg cm^{-2}). Al current collector was used for in situ XRD. The electrode laminate was dried in a vacuum oven inside of the same glove box at 60°C overnight and cut in 14 mm discs. The entire electrode fabrication process was conducted inside in an Ar-filled glove box with H_2O at ~0.6 ppm and

O_2<0.5 ppm. CR2032 type coin cells were used for all electrochemical measurements with a Li chip as the counter and reference electrode. For all other electrochemical test, 1 M LiTFSI + 0.5 M $LiNO_3$ in DME/DOL (1:1 v/v) was used as the electrolyte. Two pieces of 18 mm diameter 2320 Celgard membrane was used as the separators in all experiments. All galvanostatic cycling and rate performance tests were conducted with a Neware battery testing station. A 1400 CellTest System from Solartron was used to conduct cyclic voltammetry.

6.2.3. Physical and chemical characterization:

Cells with equal mass loadings were charged to their respective state of charge and quickly decrimped in an Ar filled glove box. The harvested electrodes were then submerged in 1 mL of fresh electrolyte as the rinsing solution. UV-Vis spectroscopy was then performed on the rinsing solution after overnight soaking. In situ X-ray diffraction was conducted at the 11 ID-C beamline at the Advanced Photon Source at Argonne National Laboratories. The wavelength of the beam was 0.1173 Å. 2θ experimentally based on a wavelength of 0.1173 Å was converted to Cu Kα-based 2θ *via* Bragg's Law for the reader's convenience. A Hitachi S-4700 Scanning Electron Microscope (SEM) was used for SEM imaging with a Bruker XFlash 6160 for Energy dispersive spectroscopy. Li-anode with deposited Na species were decrimped, not rinsed to prevent any mechanical or solvation-based removal of Na-species and transferred from the Ar glove box into a seal contained. This container was then transferred into an Ar purged glovebag attached to the SEM to reduce air contamination of samples. Similarly, X-ray photoelectron spectroscopy was conducted without rinsing the samples to avoid removing any Na polysulfide species. A XPS loading chamber was directly fitted and connected to the glove box *via* transfer chamber. Using this specialized equipment, the coin cells could be decrimped and loaded into the XPS all in an inert Ar atmosphere without exposure to ambient atmosphere.

6.3. Results and discussion

6.3.1. Confirmation of polysulfide generation in charging bulk Na_2S

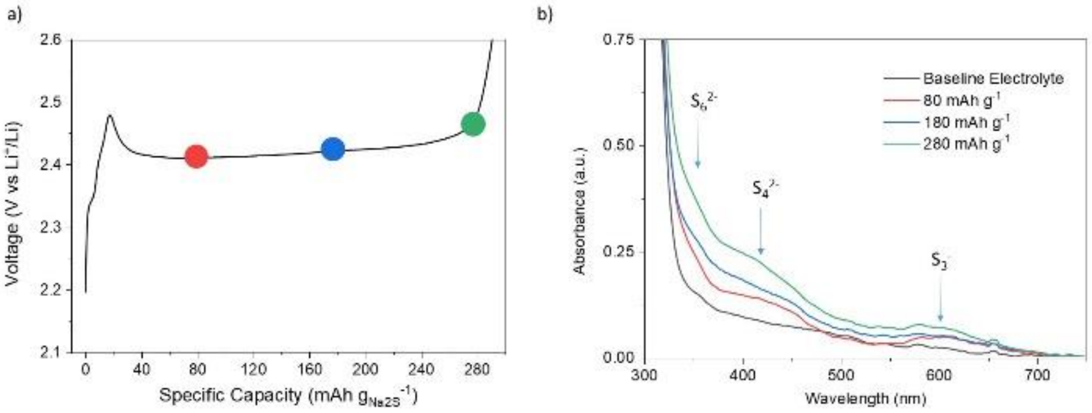

Figure 6- 2: a) Charging profile of commercial Na_2S electrode with specific capacity at which cells were decrimped for rinsing labeled with color circles b) UV-Vis absorption spectrum of baseline blank electrolyte relative to quartz sample holder and rinsing solution of Na_2S electrode charged to 80, 180 and 280 mAh g^{-1} with the blank electrolyte solution as background.

Like Li_2S, Na_2S is difficult to oxidize and will yield large overpotentials due to its poor ionic and electron conducitivity.[253,254] While it is unclear, the 1st charge mechanism of Na_2S is likely to be very similar to that of Bulk-Li_2S, producing high order polysulfide after its initial charge overpotential spike. With the overpotential experienced by Na_2S, the practical potential required for Na polysulfide generation from Na_2S aligns naturally near the equilibrium charging potential of Li_2S. Therefore, even with a large overpotential stemming from its poor ionic and electron conductivity, Na_2S will generate polysulfide anions at voltages much lower than that of bulk Li_2S and produce polysulfides spatially close to Li_2S. To take advantage of the lower practical-charging voltage of Na_2S, we must first demonstrate that Na_2S does indeed charge in a similar fashion as Li_2S even in a Li^+-based electrolyte. In a typical Li_2S electrode, the initial overpotential peak is associated to the initial formation of high order polysulfides. Based on this understanding, we charged a Na_2S electrode just past its initial overpotential peak with a specific capacity of only 80,180 and 280 mAh g^{-1}_{Na2S} (**Figure 6-2a**). The Na_2S electrode cells at various state of charge were then extracted from the coin cell and submerged in a fresh electrolyte solution to solvate any generated polysulfides. It should be noted that under an ideal sequential charging mechanism (that is, the highest oxidization of any S charges from an oxidation state of -2 to -1 and eventually to 0, in that order) a specific capacity of 80, 180 or even 280 mAh g^{-1}_{Na2S} is not enough to charge Na_2S to even Na_2S_2 (based on a theoretical specific capacity of 687 mAh g^{-1}_{Na2S}), let alone polysulfides. Yet, the Na_2S-electrode rinsing solutions exhibited a slight yellow-orange discoloration. Confirmed by our UV-Vis absorption spectroscopy (**Figure 6-2b**), there is a clear indication that there exist a distribution of polysulfide species in these rinsing solution from 300-600 nm.[255,256] In fact, the further the cell is charged from 80 to 280 mAh g^{-1}, the greater the concentration and corresponding absorbance of S_6^{2-} (350 nm[25]), S_4^{2-} (420 nm[25,257]), and S_3^- (~617 nm[25]) rinsed off from the *ex situ* electrodes. Taken together, this confirms that the charging mechanism of Na_2S is likely to be similar, if not identical to that of bulk Li_2S.[63,258] That is, the charging of Na_2S does not occur in a sequential (in terms of oxidation state) manner, but does indeed form polysulfides early in the charging process as redox mediators to assist subsequent charging of the Na_2S particles.

6.3.2. Effect of Na_2S on the 1st charge of Li_2S

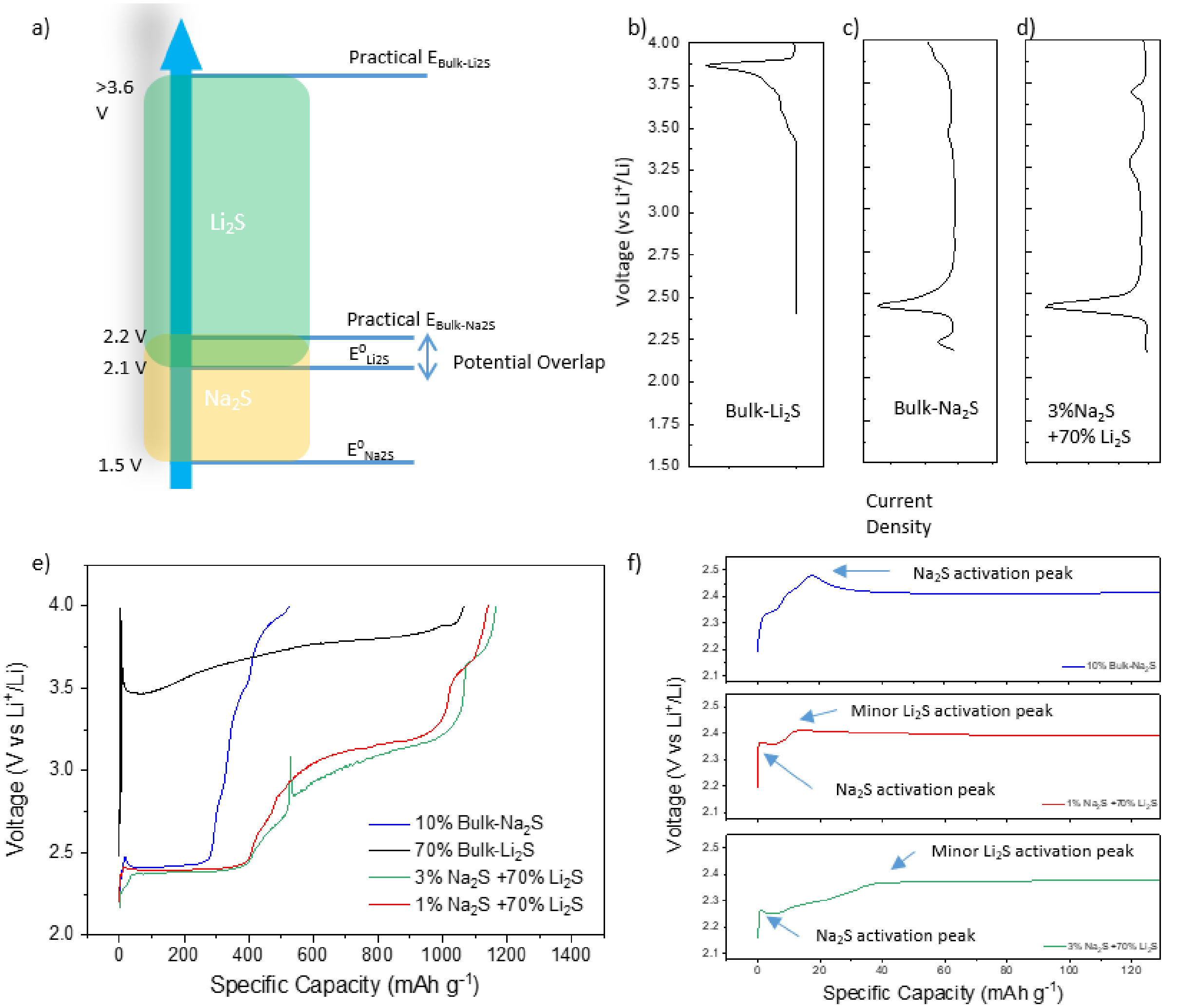

Figure 6- 3 Linear sweep voltammetry of Li_2S electrode a) without Na_2S (percentage refers to proportion of active material), b) Na_2S electrode without Li_2S (percentage refers to proportion of active material) and c) a blend of Na_2S and Li_2S (percentage refers to proportion in electrode). Schematic illustrating the overlap in the practical charging voltage of Na_2S and the equilibrium Li_2S charge voltage. e) 1st charge profile of Na_2S, Bulk-Li_2S, 1% and 3% Na_2S + 70% Li_2S at 0.05C. f) Expanded view of 1st activation peaks.

The most important and convenient difference between Na_2S versus Li_2S oxidation is its naturally lower voltage versus lithium. Linear sweep voltammetry (LSV) data of a Li_2S electrode (70 wt. % Li_2S in slurry formulation, herein denoted as Bulk-Li_2S) indicates that the potential required to activate the Bulk-Li_2S without any additives is about 3.5-3.8 V as shown in **Figure 6-3a**. This is well above the thermodynamic potential of 2.1-2.3 V. Similarly, the charging potential of a Na_2S electrode (herein denoted as Na_2S) requires a charging potential of about 2.25-2.5 V vs Li^+/Li (**Figure 6-3b**) to activate, which is significantly higher than the equilibrium potential of 1.5 V vs Na^+/Na (~1.8 V vs Li^+/Li) for Na_2S.

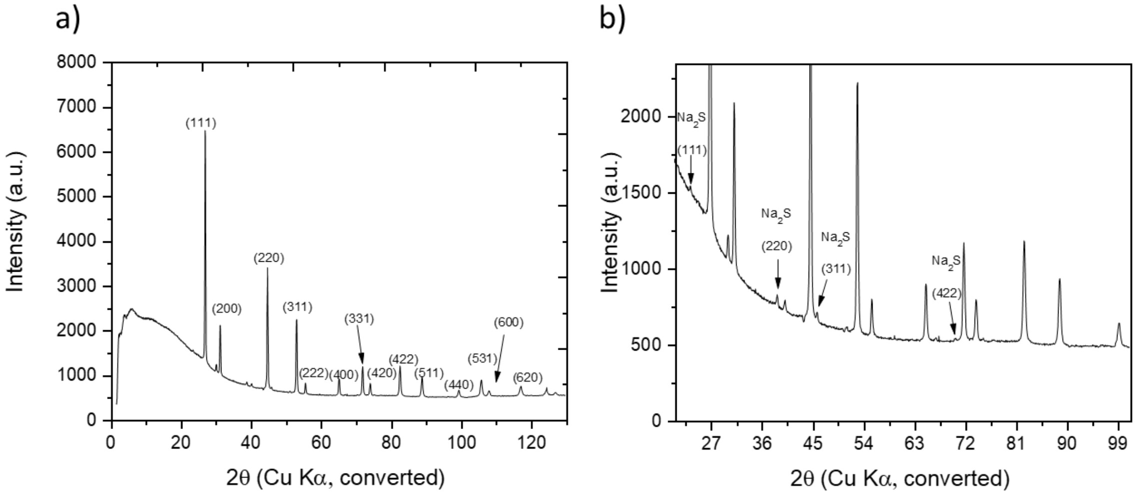

Figure 6- 4: Synchrotron high energy X-ray diffraction pattern of 1% Na_2S + 70% Li_2S electrode at with a) Li_2S pattern labelled and with b) Na_2S labelled. Because the mass fraction of Na_2S was so low, the materials was scrapped off from the current collector and pack into a thicker sample to obtain observable Na_2S diffraction pattern. Data collected at λ=0.01173 nm and converted to 0.1504 nm.

By simply blending 1-3 wt. % Na_2S into a 70 wt. % Li_2S electrode slurry formulation (Na_2S maintained its crystal structure as shown from X-ray diffraction pattern, as shown in **Figure 6-4a-b**), a LSV profile similar to that of pure Na_2S is observed (**Figure 6-3c**). Specifically, the oxidation peak was reduced from 3.5-3.8 V to about ~2.42 V with smaller peaks at ~3.28 and ~3.7 V. The LSV of Na_2S indicates that the practical activation potential of Na_2S (and as such the production of polysulfides) occurs at a voltage that well overlaps the equilibrium potential of Li_2S. This convenient phenomenon (as depicted on **Figure 6-3d**) allows for the observed decreased LSV oxidation peak of the 3%Na_2S+70%Li_2S electrode. Perhaps more practically relevant is the impact of this bulk mixing on the galvanostatic charging (**Figure 6-3e**). It is clear that even without any modifications to the electrode or material, Na_2S produces an initial charging overpotential peak of ~2.5 V vs Li^+/Li. Though this is significantly higher than the thermodynamic potential of Na_2S, it is still substantially lower than the practical bulk-Li_2S (high wt. %) activation process which occurs around 3.6 V vs Li^+/Li. Corroborating well with the LSV, the incorporation of Na_2S at only 1 and 3 wt.% (with a full desodiation capacity of only ~27.5 mAh $g^{-1}{}_{Na2S+Li2S}$) resulted in a significant drop in the Galvanostatic charging potential and effectively decreased the energy required to activate Li_2S. **Figure 6-3f** reveals that there is still an initial oxidation peak for both 1% and 3% Na_2S containing electrodes. This is followed by a second minor oxidation peak likely due to the Li_2S as observed in our previous work.[251] Interestingly, the peak potential of the blended system dropped below that of pure Na_2S. This could be due to some synergistic effect where the Na_2S-sourced polysulfides activated Li_2S, generating more polysulfides in a more efficient manner.

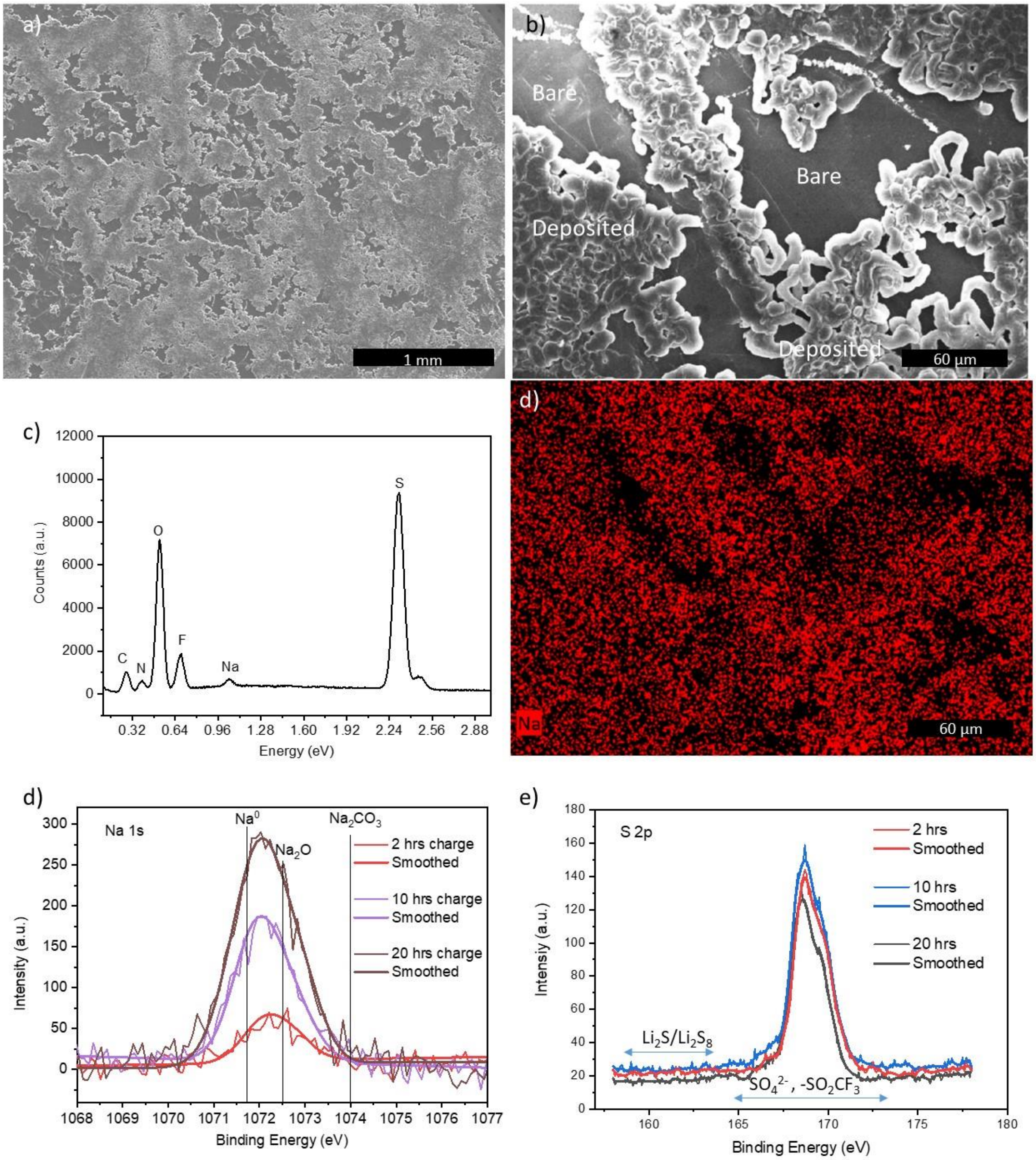

Figure 6- 5: SEM of reference/counter electrode of coin cell after 1st charge of Na_2S+Li_2S working electrode at a) low magnification, b) high magnification. c) Energy dispersive spectroscopy spectrum and d) Na elemental mapping of (b). X-ray photoelectron

spectroscopy of reference/counter electrode of d) Na 1s and e) S 2p at different state of 1st charge (0.05C).

Interestingly, SEM of the counter/reference electrode (Li metal, **Figure 6-5a-b**) shows deposited Li metal. This is to be expected with or without Na_2S. However, the energy dispersive spectroscopy (EDS) analysis (**Figure 6-5c)** reveals significant amount of Na signal on the anode. EDS-elemental mapping of Na also reveals quite a uniform distribution of Na over the deposited Li metal, which indicates at least the dissolution of Na_2S into Na-ions into the electrode. Whether Na was deposited in its metallic form on the counter electrode is unclear. XPS of the counter/reference electrode was conducted at different state of 1st charge (of the Na_2S+Li_2S cathode) in an attempt to identify the nature of the Na atoms. Unfortunately, from the XPS spectra (shown on **Figure 6-5d**) of Na 1s, it is very difficult to confidently determine any proportion of elemental Na or oxidized Na. It is worth pointing out that the signal of Na 1s increases with increasing charging time. Even more interesting is the overall absence of polysulfide/Li_2S signal usually present at a binding energy of <164 eV as shown in **Figure 6-5e**.[259] All of the observed S 2p signal originate from the sulfur in LiTFSI electrolyte salt.

6.3.3. Operando X-ray diffraction study

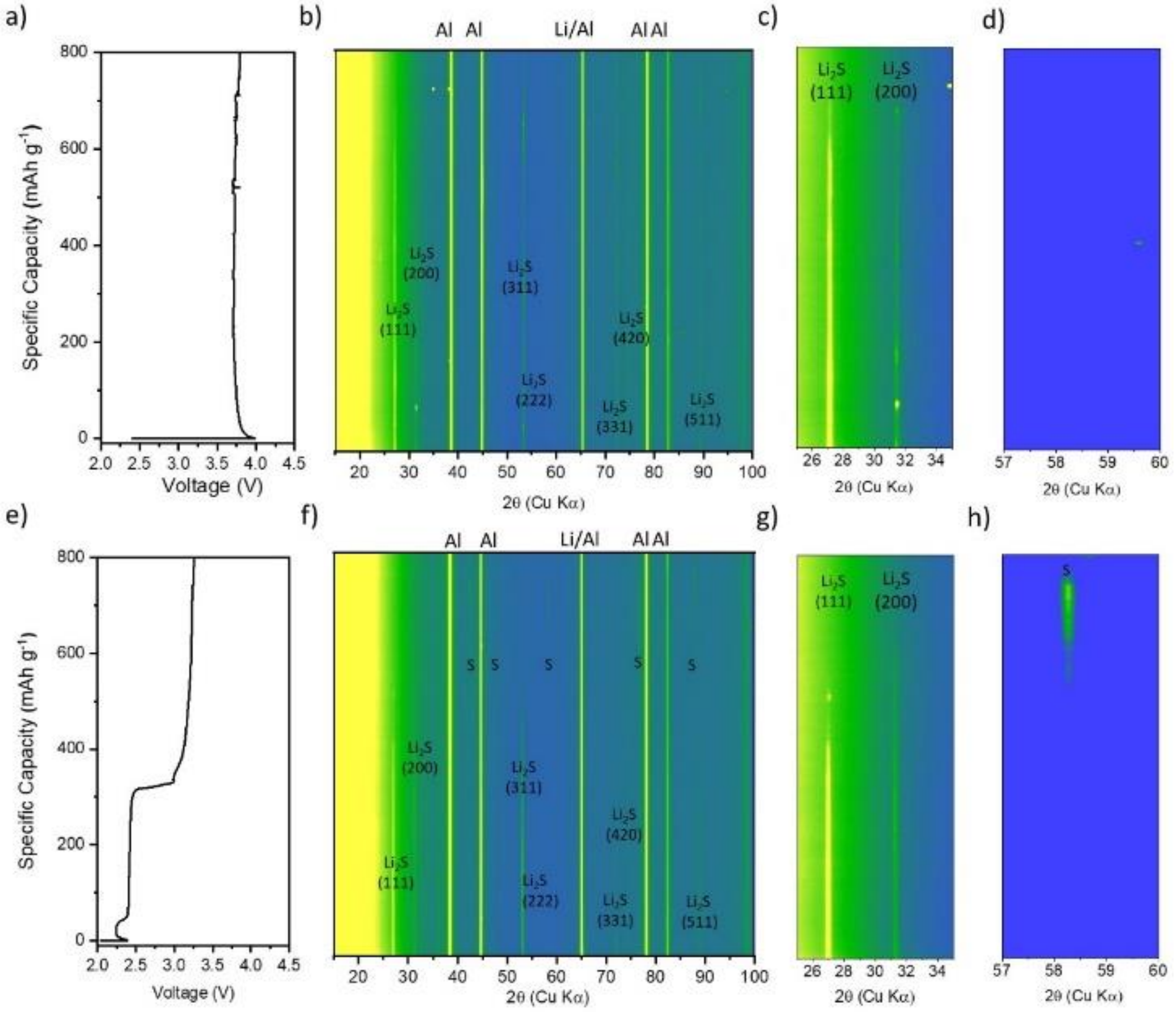

Figure 6- 6:a, e) First charge voltage profile of Li_2S electrode without Na_2S and with 1wt% Na_2S respectively. Corresponding *operando* X-ray diffraction from b, f) 2θ =15-100, c, g) 2θ =25-35 and d, h) 2θ =57-60 of electrode without and with Na_2S respectively.

Operando X-ray diffraction (XRD) revealed that the electrode without Na_2S (**Figure 6-6a**) exhibited a high 1st charge voltage (>3.6 V). Diffraction peaks corresponding to Li_2S persisted well towards 800 mAh g^{-1}_{Li2S} as shown in **Figure 6-6b-c**. No elemental sulfur peaks were found even well into the charge process (**Figure 6-6d**). Interestingly, the 1 wt.% Na_2S containing electrode exhibited quite different diffraction pattern profile as a function of state of charge. With the decreased voltage profile shown in **Figure 6-5e**, the diffraction in **Figure 6-6f** clearly reveals that the Li_2S peaks disappears after ~520 mAh g^{-1}_{Li2S}. More importantly, the diffraction peak at 27° (111) decreases and vanishes at ~450 mAh g^{-1}_{Li2S} followed by the disappearance of the ~31.3° (200) peak at ~600 mAh g^{-1}_{Li2S} (**Figure 6-6g**). The exact reason for the different rate of disappearance between the 111 and 200 diffraction peaks remains to be unclear. This observation is in contrast to our pure Li_2S baseline electrode and previous *operando* XRD literature of Li_2S cells.[260,261] As the oxidation of Li_2S is ultimately a dissolution process, it is reasonable to assume there is some resemblance to other dissolution systems.[262] We believe this is indicative that the reaction between polysulfide and Li_2S has a directional preference, where certain facets (111) are more reactive than others (200). Extrapolating from our observation, the quicker loss of the (111) plane suggests higher reactivity of the vertex-atom of each Li_2S grain. Once these vertex-atoms are cleaved, more vertex-atoms of the crystal grains will be exposed. Each set of newly exposed vertex-atoms represents a unit cell's (111) plane, resulting in the directional loss of the cubic structure. This could be related to the relatively low overpotential offered by the Na_2S-generated polysulfide, enabling oxidation at a lower voltage i.e. milder reaction driving force, and ultimately the more selective charging of vertex-atoms over the less exposed edge-atoms. Near the end of charge, elemental sulfur diffraction peaks were found to appear at around a charge capacity of 580 mAh g^{-1}_{Li2S} for the electrode tested with 1 wt.% Na_2S as shown in **Figure 6-6h**. In contrast, no sulfur peak can be observed in the electrode without Na_2S.

6.3.4. Electrochemical performance at strict conditions

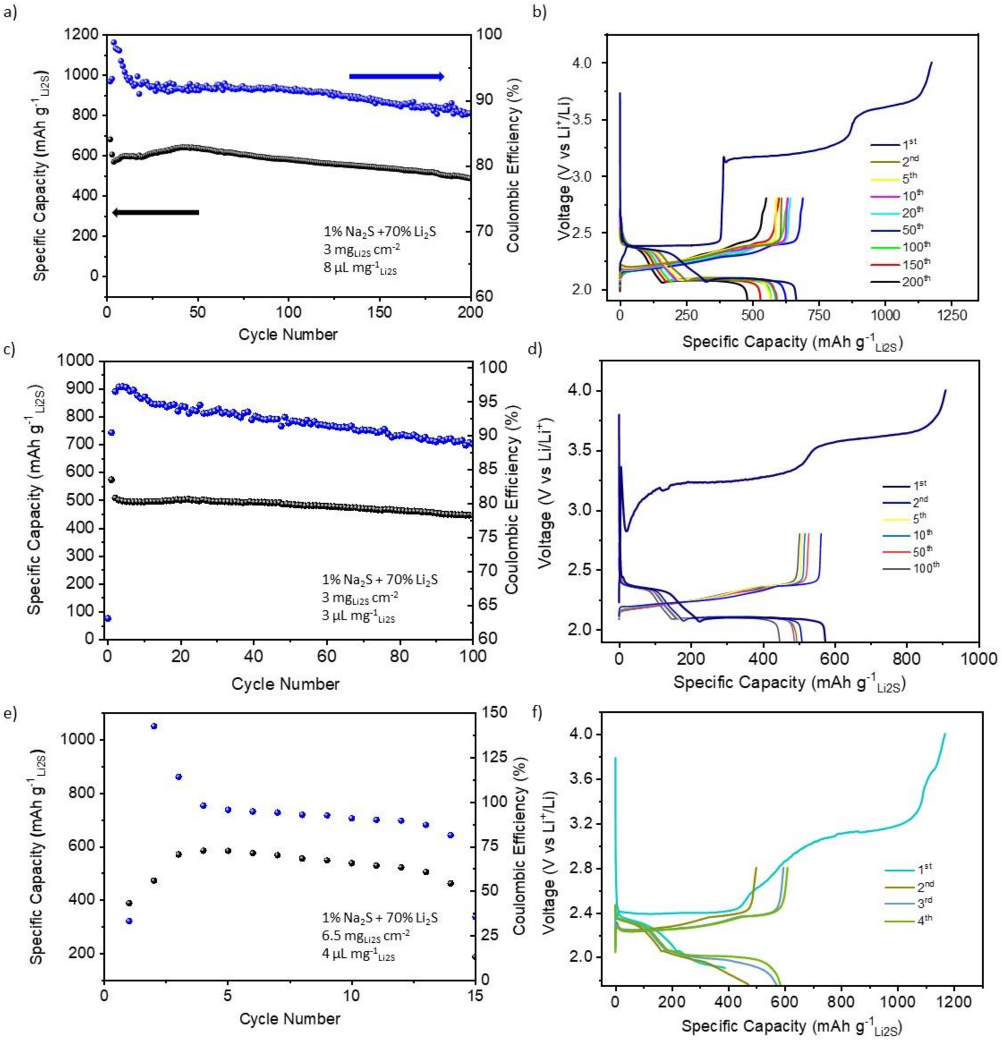

Figure 6- 7: Cycling performance and corresponding charge/discharge voltage profiles of 1% Na_2S + 70% Li_2S at a-b) 2 mg_{Li2S} cm^{-2}/8 µL mg^{-1}_{Li2S} (1st charge at 0.05C and then cycled at 0.1C). c-d) 3 mg_{Li2S} cm^{-2}/3 µL mg^{-1}_{Li2S} (1st charge at 0.05C and then cycled at 0.05C) and e-f) 6.5 mg_{Li2S} cm^{-2}/4 µL mg^{-1}_{Li2S} (1st charge at 0.05 C and then cycled at 0.1C).

The cycling performance and charge/discharge voltage profiles of the 1% Na_2S +70% Li_2S electrodes at 2 mg_{Li2S} cm^{-2} and 8 µL mg^{-1}_{Li2S} and 3 µL mg^{-1}_{Li2S} are shown in **Figure 6-7a-b** and **Figure 6-7c-d** respectively. At these strict conditions, a high initial discharge of ~700 mAh g^{-1}_{Li2S}

(converting to about 1000 mAh $g^{-1}{}_{S}$) was achieved at 8 µL $mg^{-1}{}_{Li2S}$. After 200 cycles, the capacity dropped to about 490 mAh $g^{-1}{}_{Li2S}$. With the electrolyte tuned down to 3 µL $mg^{-1}{}_{Li2S}$ (lean electrolyte conditions), the first discharge decreased to about 580 mAh $g^{-1}{}_{Li2S}$ (829.4 mAh $g^{-1}{}_{S}$) and maintained stable cycling up to 100 cycles (~450 mAh $g^{-1}{}_{Li2S}$). **Figure 6-7e-f** shows the cycling and charge/discharge voltage profile for cells ran at 6.5 mg_{Li2S} cm^{-2} and 4 µL $mg^{-1}{}_{Li2S}$. Notably, the impact of increasing mass loading on the overpotential is less than that of decreasing the electrolyte content to 3 µL $mg^{-1}{}_{Li2S}$. It is important to note the lack of overall cell engineering in obtaining these performances, demonstrating the effectiveness of using Na_2S as a low-content electrode additive.

6.4. Conclusion

Overall, we have shown that just 1 wt% of commercial Na_2S can *in situ* inject polysulfide into the system at significantly lowered voltages (in comparison to bulk Li_2S) for activating commercially available Li_2S. In contrast to pre-solvated polysulfide in the electrolyte, this source of polysulfide will remain dormant unless electrochemically activated. When compared to the last iteration of the use of a redox mediator generator, that is, Li_3PS_4 (Chapter 5), we found that Na_2S exhibited superior electrochemical characteristics. This include lower first charge potential even at decrease electrolyte conditions (3 µL $mg^{-1}{}_{Li2S}$) and increased Li_2S loading of 3 mg_{Li2S} cm^{-2} versus 1.5 mg_{Li2S} cm^{-2} of the Li_3PS_4 electrodes. Notably this was achieved also without significant modification to the battery and in fact required even less amounts of additive, decreasing from 10 wt.% of Li_3PS_4 to only 1 wt.% of Na_2S. More importantly, future work in material engineering composites of Na_2S and Li_2S will likely yield electrodes with higher performance metrics with less restrictions on particle size control.

Chapter 7: Conclusion and future work

7.1. Summary of Conclusions

The objectives of this thesis are to deliver methods that can enable cyclability in sulfur-based cathode at strict conditions (high areal sulfur loadings and low electrolyte to sulfur ratios). This goal is critical as only by testing at operating conditions that emulate real-world application can the field of sulfur-based cathode move closer to commercialization. The hypothesis is that by developing macroporous carbon structures, we will be able to facilitate electrolyte infiltration and offer a more efficient distribution of electrolyte, while the development of advanced Li_2S-based cathodes offers an alternative strategy through the replacement of the arguably more problematic Li metal anode.

Specifically, in Chapter 3, we present the development of a hollow carbon structure with porous shells. This material has a large void at its core (~500-1000nm) and demonstrated excellent rate performance and cycle stability. This material was first developed at relaxed testing conditions (low area sulfur loading and high electrolyte content). In Chapter 4, this material was further developed by spray draying with graphene oxide and heated treated to yield a reduced graphene oxide wrapped agglomerated hollow carbons particles. Exceptional performance was observed at strict conditions. An extremely low electrolyte content of 2.8 $\mu L\ mg^{-1}_{S}$ was achieved through this design. Furthermore, *operando* electrochemical impedance spectroscopy and *operando* X-ray diffraction revealed that sulfur is likely passivating certain conductive components of the cathode, preventing further discharge at strict conditions.

Chapter 5 present our second major direction in solving the problems of strict condition cycling. As the problem of a Li metallic is arguably more problematic than even the sulfur-cathode, this thesis looked to switch the Li-ion source from the Li metal to the prelithiated Li_2S. Although Li_2S has many promising advantages such as serving as an Li-ion source, higher thermal stability (advantageous for electrolyte drying) and Li_2S is already volumetrically expanded allowing for electrode designs that contract rather than expand first, micron-sized commercial Li_2S unfortunately is also very difficult to electrochemically activate.

To solve this problem, redox mediators have been employed throughout literature, as they can alleviate the dependency of the Li_2S oxidation process on Li_2S's ionic and electronic conductivity. Chapter 5 revealed that the direct use of redox mediator cannot function at strict testing conditions. An introduction of the first every reported use of what we call a solid-sourced redox mediator generator was then presented. This class of electrode additive remains solid and only produces redox mediators that is only generated at the appropriate voltage. Li_3PS_4 was presented to demonstrate the efficacy of this strategy with exceptional reduction in charge overpotential and increased specific capacity at strict testing conditions. Chapter 6 present Na_2S as another solid-sourced redox mediator generator. This additive was able to achieve sufficient activation of Li_2S at lower overpotentials with lower weight proportion in the electrode. Furthermore, the generator redox mediators are polysulfide species and can serve as active material in later cycles.

Together, both research directions presented in this thesis (sulfur host engineering and Li_2S-activiating additive) were able to achieve cyclability at low electrolyte content and high sulfur loading. The electrolyte content (<8 µL $mg^{-1}{}_{s}$) and sulfur loading (>4 mg_s cm^{-2}) targets have been met.

7.2. Future Works

The current research into Li-S batteries have met a very severe roadblock that must be resolved before the field can move any further. The lack of acceptable performance metrics at high loading and low electrolyte content remains to be the most difficult problem to be resolved. Although this work has demonstrated improved performance at these strict testing conditions, they are still far from any commercial benchmark. Based on the conclusions of this thesis, recommended future research directions are as follows:

1. Spray drying is a promising technique to further the performance of Li-S operated at strict conditions. Future work might include inclusion of additional materials with stronger polysulfide adsorption capabilities such as various metal oxides and sulfide. The recent trends in defect engineering of these metal chalcogenides i.e. anion deficient metal chalcogenide with enhanced electronic conductivities will likely be enhanced in performance (at strict conditions) if spray dried.
2. Performance enhancement any materials at low electrolyte conditions should be benefit from the inclusion of macropores. As such, the development of a macroporous framework with anion deficient metal chalcogenides materials will also likely benefit performance at strict conditions.
3. Based on this work and reports in literature, it appears that further significant progress will be unlikely unless a deeper fundamental understanding of the problem can be made. Therefore, future works should include advanced characterization techniques that probe exactly the difference in cycling mechanism between low and high electrolyte content. Such work has been seldom performed in the literature. Specifically, *operando*-based techniques such as X-ray diffraction, X-ray

adsorption, Raman, UV-VIS, Small angle X-ray scattering among others, will likely begin to play a very large if not pivotal role in any further development of Li-S batteries. However, this is rather difficult due to the dynamic nature of polysulfide reduction, likely requiring relatively high temporal resolution.

4. Anode pairing with the developed Li_2S cathode is a crucial next step. Future work should include performance testing of anode such as Si, graphite, or metal oxides in a full cell prototype. Optimization in the electrolyte composition and engineering of the anode would be crucial.
5. While the work presented on decreasing the 1st charge overpotential of Li_2S has demonstrated that complex cell engineering is not necessarily required. Future work might include integration of solid-sourced redox mediator generated identified in this thesis into other material design.
6. Lastly, because Li_2S is less dense than sulfur, the volume expansion-associated problems of sulfur lithiation might be mitigated. Specifically, this property is advantageous because it allows for the calendaring of Li_2S electrode without having to take into the account the volume required for the transformation of S to Li_2S. This advantage of Li_2S should not be overlooked and might in the end, be a critical determining factor to the packing of the electrode when sulfur-based systems reach closer to commercial levels. Similar importance can be rationalized for the currently more popular solid-state battery systems.
7. Negative and positive capacity pairing (N/P ratio) should be carefully measured in any future work of sulfur-based battery systems. This metric in addition to the strict conditions defined in this thesis is very key towards achieving high energy density.

Currently throughout literature and admittedly also in this thesis, lithium metal used has areal-capacities significantly beyond any significant commercial significance. Even with the cycling at strict conditions, the energy density of sulfur-based cells will be very low due to the extremely high excess of lithium metal. Therefore, a major future direction is to further improve performance at high sulfur loading, low electrolyte to sulfur ratio and decrease the N/P ratio to below 3.

References

(1) Park, J. K.: Introduction. In *Principles and Applications of Lithium Secondary Batteries*; Wiley-VCH: Germany, 2012; pp 1-4.

(2) Li, M.; Lu, J.; Chen, Z. W.; Amine, K. 30 Years of Lithium-Ion Batteries. *Adv. Mater.* **2018**, *30*, 1800561.

(3) Whittingham, M. S. Lithium Batteries and Cathode Materials. *Chem. Rev.* **2004**, *104*, 4271-4301.

(4) Ren, H.; Huang, Y.; Wang, Y.; Li, Z.; Cai, P.; Peng, Z.; Zhou, Y. Effects of different carbonate precipitators on LiNi1/3Co1/3Mn1/3O2 morphology and electrochemical performance. *Mater. Chem. Phys.* **2009**, *117*, 41-45.

(5) Hwang, B. J.; Tsai, Y. W.; Carlier, D.; Ceder, G. A Combined Computational/Experimental Study on LiNi1/3Co1/3Mn1/3O2. *Chemistry of Materials* **2003**, *15*, 3676-3682.

(6) Paulsen, J. M.; Thomas, C. L.; Dahn, J. R. O2 Structure Li2 / 3 [Ni 1 / 3 Mn 2 / 3] O 2: A New Layered Cathode Material for Rechargeable Lithium Batteries. I. Electrochemical Properties. *J. Electrochem. Soc.* **2000**, *147*, 861-868.

(7) Assat, G.; Foix, D.; Delacourt, C.; Iadecola, A.; Dedryvère, R.; Tarascon, J.-M. Fundamental interplay between anionic/cationic redox governing the kinetics and thermodynamics of lithium-rich cathodes. *Nat. Commun.* **2017**, *8*, 2219.

(8) Grimaud, A.; Hong, W. T.; Shao-Horn, Y.; Tarascon, J. M. Anionic redox processes for electrochemical devices. *Nature Materials* **2016**, *15*, 121.

(9) Li, M.; Lu, J.; Chen, Z.; Amine, K. 30 Years of Lithium-Ion Batteries. *Adv. Mater.* **2018**, 1800561.

(10) Liu, T.; Dai, A.; Lu, J.; Yuan, Y.; Xiao, Y.; Yu, L.; Li, M.; Gim, J.; Ma, L.; Liu, J.; Zhan, C.; Li, L.; Zheng, J.; Ren, Y.; Wu, T.; Shahbazian-Yassar, R.; Wen, J.; Pan, F.; Amine, K. Correlation between manganese dissolution and dynamic phase stability in spinel-based lithium-ion battery. *Nat. Commun.* **2019**, *10*, 4721.

(11) Fotouhi, A.; Auger, D. J.; Propp, K.; Longo, S.; Wild, M. A review on electric vehicle battery modelling: From Lithium-ion toward Lithium–Sulphur. *Renewable and Sustainable Energy Reviews* **2016**, *56*, 1008-1021.

(12) M. Wild , L. O. N., T. Zhang , R. Purkayastha , G. Minton , M. Marinescu and G. J. Offer. Lithium sulfur batteries, a mechanistic review. *Energy Environ. Science* **2015**.

(13) Ritchie, A. G.; Giwa, C. O.; Lee, J. C.; Bowles, P.; Gilmour, A.; Allan, J.; Rice, D. A.; Brady, F.; Tsang, S. C. E. Future cathode materials for lithium rechargeable batteries. *J. Power Sources* **1999**, *80*, 98-102.

(14) Lin, J.; Mu, D.; Jin, Y.; Wu, B.; Ma, Y.; Wu, F. Li-rich layered composite $Li[Li_{0.2}Ni_{0.2}Mn_{0.6}]O_2$ synthesized by a novel approach as cathode material for lithium ion battery. *J. Power Sources* **2013**, *230*, 76-80.

(15) Chen, R.; Ren, S.; Knapp, M.; Wang, D.; Witter, R.; Fichtner, M.; Hahn, H. Disordered Lithium-Rich Oxyfluoride as a Stable Host for Enhanced Li^+ Intercalation Storage. *Adv. Energy Mater.* **2015**, *5*, 1401814.

(16) Sathiya, M.; Rousse, G.; Ramesha, K.; Laisa, C. P.; Vezin, H.; Sougrati, M. T.; Doublet, M. L.; Foix, D.; Gonbeau, D.; Walker, W.; Prakash, A. S.; Ben Hassine, M.; Dupont, L.; Tarascon, J. M. Reversible anionic redox chemistry in high-capacity layered-oxide electrodes. *Nature Materials* **2013**, *12*, 827-835.

(17) Perez, A. J.; Jacquet, Q.; Batuk, D.; Iadecola, A.; Saubanère, M.; Rousse, G.; Larcher, D.; Vezin, H.; Doublet, M.-L.; Tarascon, J.-M. Approaching the limits of cationic and anionic electrochemical activity with the Li-rich layered rocksalt Li_3IrO_4. *Nat. Energy* **2017**, *2*, 954-962.

(18) Liu, C.; Neale, Z. G.; Cao, G. Understanding electrochemical potentials of cathode materials in rechargeable batteries. *Mater. Today* **2016**, *19*, 109-123.

(19) Pope, M. A.; Aksay, I. A. Structural Design of Cathodes for Li-S Batteries. *Adv. Energy Mater.* **2015**, *5*, 1500124.

(20) Barchasz, C.; Molton, F.; Duboc, C.; Lepretre, J. C.; Patoux, S.; Alloin, F. Lithium/sulfur cell discharge mechanism: an original approach for intermediate species identification. *Analytical chemistry* **2012**, *84*, 3973-3980.

(21) Ji, X.; Nazar, L. F. Advances in Li–S batteries. *Journal of Materials Chemistry* **2010**, *20*, 9821.

(22) Wang, Q.; Zheng, J.; Walter, E.; Pan, H.; Lv, D.; Zuo, P.; Chen, H.; Deng, Z. D.; Liaw, B. Y.; Yu, X.; Yang, X.; Zhang, J.-G.; Liu, J.; Xiao, J. Direct Observation of Sulfur Radicals as Reaction Media in Lithium Sulfur Batteries. *J. Electrochem. Soc.* **2015**, *162*, A474-A478.

(23) Cuisinier, M.; Hart, C.; Balasubramanian, M.; Garsuch, A.; Nazar, L. F. Radical or Not Radical: Revisiting Lithium–Sulfur Electrochemistry in Nonaqueous Electrolytes. *Adv. Energy Mater.* **2015**, *5*, 1401801.

(24) Vijayakumar, M.; Govind, N.; Walter, E.; Burton, S. D.; Shukla, A.; Devaraj, A.; Xiao, J.; Liu, J.; Wang, C.; Karim, A.; Thevuthasan, S. Molecular structure and stability of dissolved lithium polysulfide species. *Physical Chemistry Chemical Physics* **2014**, *16*, 10923-10932.

(25) Barchasz, C.; Molton, F.; Duboc, C.; Leprêtre, J.-C.; Patoux, S.; Alloin, F. Lithium/Sulfur Cell Discharge Mechanism: An Original Approach for Intermediate Species Identification. *Analytical Chemistry* **2012**, *84*, 3973-3980.

(26) Liang, X.; Wen, Z.; Liu, Y.; Wu, M.; Jin, J.; Zhang, H.; Wu, X. Improved cycling performances of lithium sulfur batteries with $LiNO_3$-modified electrolyte. *J. Power Sources* **2011**, *196*, 9839-9843.

(27) Ji, X.; Lee, K. T.; Nazar, L. F. A highly ordered nanostructured carbon-sulphur cathode for lithium-sulphur batteries. *Nat Mater* **2009**, *8*, 500-506.

(28) Balach, J.; Jaumann, T.; Klose, M.; Oswald, S.; Eckert, J.; Giebeler, L. Functional Mesoporous Carbon-Coated Separator for Long-Life, High-Energy Lithium-Sulfur Batteries. *Adv. Func. Mater.* **2015**, *25*, 5285-5291.

(29) Ahn, W.; Lim, S.; Lee, D.; Kim, K.; Chen, Z.; Yeon, S. Interaction mechanism between a functionalized protective layer and dissolved polysulfide for extended cycle life of lithium sulfur batteries. *Journal of Material Chemistry A* **2015**, *3*, 9461-9467.

(30) Agostini, M.; Xiong, S.; Matic, A.; Hassoun, J. Polysulfide-containing Glyme-based Electrolytes for Lithium Sulfur Battery. *Chemistry of Materials* **2015**, *27*, 4604-4611.

(31) Wu, F.; Lee, J. T.; Nitta, N.; Kim, H.; Borodin, O.; Yushin, G. Lithium iodide as a promising electrolyte additive for lithium-sulfur batteries: mechanisms of performance enhancement. *Adv Mater* **2015**, *27*, 101-108.

(32) Ahn, W.; Seo, M. H.; Jun, Y. S.; Lee, D. U.; Hassan, F. M.; Wang, X.; Yu, A.; Chen, Z. Sulfur nano-granular film coated three-dimensional graphene sponge based high power lithium sulfur battery. *ACS Appl Mater Interfaces* **2016**, *8*, 1984-1991.

(33) Zhou, G.; Paek, E.; Hwang, G. S.; Manthiram, A. Long-life Li/polysulphide batteries with high sulphur loading enabled by lightweight three-dimensional nitrogen/sulphur-codoped graphene sponge. *Nat Commun* **2015**, *6*, 7760.

(34) Guo, J.; Xu, Y.; Wang, C. Sulfur-impregnated disordered carbon nanotubes cathode for lithium-sulfur batteries. *Nano Lett* **2011**, *11*, 4288-4294.

(35) Xiulei Ji, K. T. L. a. L. F. N. A highly ordered nanostructured carbon–sulphur cathode for lithium–sulphur batteries. *Nature Materials* **2009**, *8*.

(36) Jayaprakash, N.; Shen, J.; Moganty, S. S.; Corona, A.; Archer, L. A. Porous hollow carbon@sulfur composites for high-power lithium-sulfur batteries. *Angewandte Chemie International Edition* **2011**, *50*, 5904-5908.

(37) Song, J.; Xu, T.; Gordin, M. L.; Zhu, P.; Lv, D.; Jiang, Y.-B.; Chen, Y.; Duan, Y.; Wang, D. Nitrogen-Doped Mesoporous Carbon Promoted Chemical Adsorption of Sulfur and Fabrication of High-Areal-Capacity Sulfur Cathode with Exceptional Cycling Stability for Lithium-Sulfur Batteries. *Adv. Funct. Mater.* **2014**, *24*, 1243-1250.

(38) Song, J.; Gordin, M. L.; Xu, T.; Chen, S.; Yu, Z.; Sohn, H.; Lu, J.; Ren, Y.; Duan, Y.; Wang, D. Strong lithium polysulfide chemisorption on electroactive sites of nitrogen-doped carbon composites for high-performance lithium-sulfur battery cathodes. *Angewandte Chemie International Edition* **2015**, *54*, 4325-4329.

(39) Xiao, J. Understanding the Lithium Sulfur Battery System at Relevant Scales. *Adv. Energy Mater.* **2015**, *5*, 1501102.

(40) Lv, D.; Zheng, J.; Li, Q.; Xie, X.; Ferrara, S.; Nie, Z.; Mehdi, L. B.; Browning, N. D.; Zhang, J.-G.; Graff, G. L.; Liu, J.; Xiao, J. High Energy Density Lithium-Sulfur Batteries: Challenges of Thick Sulfur Cathodes. *Adv. Energy Mater.* **2015**, *5*, 1402290.

(41) Yi, R.; Chen, S.; Song, J.; Gordin, M. L.; Manivannan, A.; Wang, D. High-Performance Hybrid Supercapacitor Enabled by a High-Rate Si-based Anode. *Adv. Func. Mater.* **2014**, *24*, 7433-7439.

(42) Xu, T.; Song, J.; Gordin, M. L.; Sohn, H.; Yu, Z.; Chen, S.; Wang, D. Mesoporous carbon-carbon nanotube-sulfur composite microspheres for high-areal-capacity lithium-sulfur battery cathodes. *ACS Appl. Mater. Interfaces* **2013**, *5*, 11355-11362.

(43) Liang, X.; Hart, C.; Pang, Q.; Garsuch, A.; Weiss, T.; Nazar, L. F. A highly efficient polysulfide mediator for lithium–sulfur batteries. *Nat Commun* **2015**, *6*, 5682

(44) Liu, Y.; Li, G.; Fu, J.; Chen, Z.; Peng, X. Strings of Porous Carbon Polyhedrons as Self-Standing Cathode Host for High-Energy-Density Lithium-Sulfur Batteries. *Angew Chem Int Ed Engl* **2017**, *56*, 1-6.

(45) Hagen, M.; Hanselmann, D.; Ahlbrecht, K.; Maça, R.; Gerber, D.; Tübke, J. Lithium-Sulfur Cells: The Gap between the State-of-the-Art and the Requirements for High Energy Battery Cells. *Adv. Energy Mater.* **2015**, *5*, 1401986.

(46) Li, M.; Zhang, Y.; Wang, X.; Ahn, W.; Jiang, G.; Feng, K.; Lui, G.; Chen, Z. Gas Pickering Emulsion Templated Hollow Carbon for High Rate Performance Lithium Sulfur Batteries. *Adv. Funct. Mater.* **2016**, *26*, 8408-8417.

(47) Li, G.; Lei, W.; Luo, D.; Deng, Y. P.; Wang, D.; Chen, Z. 3D Porous Carbon Sheets with Multidirectional Ion Pathways for Fast and Durable Lithium–Sulfur Batteries. *Adv. Energy Mater.* **2018**, *8*, 1702381.

(48) Chen, J.; Henderson, W. A.; Pan, H.; Perdue, B. R.; Cao, R.; Hu, J. Z.; Wan, C.; Han, K. S.; Mueller, K. T.; Zhang, J.-G. Improving Lithium–Sulfur Battery Performance under Lean Electrolyte through Nanoscale Confinement in Soft Swellable Gels. *Nano Lett.* **2017**, *17*, 3061-3067.

(49) Pan, H.; Han, K. S.; Engelhard, M. H.; Cao, R.; Chen, J.; Zhang, J. G.; Mueller, K. T.; Shao, Y.; Liu, J. Addressing Passivation in Lithium–Sulfur Battery Under Lean Electrolyte Condition. *Adv. Funct. Mater.* **2018**.

(50) Cheng, L.; Curtiss, L. A.; Zavadil, K. R.; Gewirth, A. A.; Shao, Y.; Gallagher, K. G. Sparingly Solvating Electrolytes for High Energy Density Lithium–Sulfur Batteries. *ACS Energy Lett.* **2016**, *1*, 503-509.

(51) Li, M.; Zhang, Y.; Hassan, F.; Ahn, W.; Wang, X.; Liu, W. W.; Jiang, G.; Chen, Z. Compact high volumetric and areal capacity lithium sulfur batteries through rock salt induced nano-architectured sulfur hosts. *Journal of Materials Chemistry A* **2017**, *5*, 21435-21441.

(52) Smith, A. J.; Burns, J. C.; Zhao, X.; Xiong, D.; Dahn, J. R. A High Precision Coulometry Study of the SEI Growth in Li/Graphite Cells. *J. Electrochem. Soc.* **2011**, *158*, A447.

(53) Li, M.; Lu, J.; Ji, X.; Li, Y.; Shao, Y.; Chen, Z.; Zhong, C.; Amine, K. Design strategies for nonaqueous multivalent-ion and monovalent-ion battery anodes. *Nature Reviews Materials* **2020**.

(54) Tu, Z. Y.; Kambe, Y.; Lu, Y. Y.; Archer, L. A. Nanoporous Polymer-Ceramic Composite Electrolytes for Lithium Metal Batteries. *Adv. Energy Mater.* **2014**, *4*.

(55) Khurana, R.; Schaefer, J. L.; Archer, L. A.; Coates, G. W. Suppression of Lithium Dendrite Growth Using Cross-Linked Polyethylene/Poly(ethylene oxide) Electrolytes: A New Approach for Practical Lithium-Metal Polymer Batteries. *Journal of the American Chemical Society* **2014**, *136*, 7395-7402.

(56) Zheng, G. Y.; Lee, S. W.; Liang, Z.; Lee, H. W.; Yan, K.; Yao, H. B.; Wang, H. T.; Li, W. Y.; Chu, S.; Cui, Y. Interconnected hollow carbon nanospheres for stable lithium metal anodes. *Nat Nanotechnol* **2014**, *9*, 618-623.

(57) Lu, Y. Y.; Das, S. K.; Moganty, S. S.; Archer, L. A. Ionic Liquid-Nanoparticle Hybrid Electrolytes and their Application in Secondary Lithium-Metal Batteries. *Adv. Mater.* **2012**, *24*, 4430-4435.

(58) Kim, J.-S.; Yoo, D.-J.; Min, J.; Shakoor, R. A.; Kahraman, R.; Choi, J. W. Poreless Separator and Electrolyte Additive for Lithium-Sulfur Batteries with High Areal Energy Densities. *ChemNanoMat* **2015**, *1*, 240-245.

(59) He, Y.; Ren, X.; Xu, Y.; Engelhard, M. H.; Li, X.; Xiao, J.; Liu, J.; Zhang, J. G.; Xu, W.; Wang, C. Origin of lithium whisker formation and growth under stress. *Nat. Nanotechnol.* **2019**.

(60) Niu, C.; Lee, H.; Chen, S.; Li, Q.; Du, J.; Xu, W.; Zhang, J.-G.; Whittingham, M. S.; Xiao, J.; Liu, J. High-energy lithium metal pouch cells with limited anode swelling and long stable cycles. *Nat. Energy* **2019**, *4*, 551-559.

(61) Ren, X.; Zou, L.; Cao, X.; Engelhard, M. H.; Liu, W.; Burton, S. D.; Lee, H.; Niu, C.; Matthews, B. E.; Zhu, Z.; Wang, C.; Arey, B. W.; Xiao, J.; Liu, J.; Zhang, J.-G.; Xu, W. Enabling High-Voltage Lithium-Metal Batteries under Practical Conditions. *Joule* **2019**, *3*, 1662-1676.

(62) Niu, C.; Pan, H.; Xu, W.; Xiao, J.; Zhang, J.-G.; Luo, L.; Wang, C.; Mei, D.; Meng, J.; Wang, X.; Liu, Z.; Mai, L.; Liu, J. Self-smoothing anode for achieving high-energy lithium metal batteries under realistic conditions. *Nature Nanotechnology* **2019**, *14*, 594-601.

(63) Tan, G.; Xu, R.; Xing, Z.; Yuan, Y.; Lu, J.; Wen, J.; Liu, C.; Ma, L.; Zhan, C.; Liu, Q.; Wu, T.; Jian, Z.; Shahbazian-Yassar, R.; Ren, Y.; Miller, D. J.; Curtiss, L. A.; Ji, X.; Amine, K. Burning lithium in CS_2 for high-performing compact Li_2S–graphene nanocapsules for Li–S batteries. *Nat. Energy* **2017**, *2*, 17090.

(64) Li, M.; Chen, Z.; Wu, T.; Lu, J. Li_2S- or S-Based Lithium-Ion Batteries. *Adv. Mater.* **2018**, *30*, 1801190.

(65) Son, Y.; Lee, J.-S.; Son, Y.; Jang, J.-H.; Cho, J. Recent Advances in Lithium Sulfide Cathode Materials and Their Use in Lithium Sulfur Batteries. *Adv. Energy Mater.* **2015**, *5*, 1500110.

(66) Agostini, M.; Hassoun, J.; Liu, J.; Jeong, M.; Nara, H.; Momma, T.; Osaka, T.; Sun, Y.-K.; Scrosati, B. A lithium-ion sulfur battery based on a carbon-coated lithium-sulfide cathode and an electrodeposited silicon-based anode. *ACS Appl. Mater. Interfaces* **2014**, *6*, 10924-10928.

(67) Brückner, J.; Thieme, S.; Böttger-Hiller, F.; Bauer, I.; Grossmann, H. T.; Strubel, P.; Althues, H.; Spange, S.; Kaskel, S. Carbon-Based Anodes for Lithium Sulfur Full Cells with High Cycle Stability. *Adv. Funct. Mater.* **2014**, *24*, 1284-1289.

(68) Elazari, R.; Salitra, G.; Gershinsky, G.; Garsuch, A.; Panchenko, A.; Aurbach, D. Rechargeable lithiated silicon–sulfur (SLS) battery prototypes. *Electrochem. commun.* **2012**, *14*, 21-24.

(69) Hassoun, J.; Kim, J.; Lee, D.-J.; Jung, H.-G.; Lee, S.-M.; Sun, Y.-K.; Scrosati, B. A contribution to the progress of high energy batteries: A metal-free, lithium-ion, silicon–sulfur battery. *J. Power Sources* **2012**, *202*, 308-313.

(70) Lee, S.-K.; Oh, S.-M.; Park, E.; Scrosati, B.; Hassoun, J.; Park, M.-S.; Kim, Y.-J.; Kim, H.; Belharouak, I.; Sun, Y.-K. Highly Cyclable Lithium–Sulfur Batteries With a Dual-Type Sulfur Cathode and a Lithiated Si/SiO x Nanosphere Anode. *Nano Lett.* **2015**, *15*, 2863-2868.

(71) Li, B.; Li, S.; Xu, J.; Yang, S. A new configured lithiated silicon–sulfur battery built on 3D graphene with superior electrochemical performances. *Energy & Environmental Science* **2016**, *9*, 2025-2030.

(72) Yang, Y.; McDowell, M. T.; Jackson, A.; Cha, J. J.; Hong, S. S.; Cui, Y. New nanostructured Li2S/silicon rechargeable battery with high specific energy. *Nano Lett.* **2010**, *10*, 1486-1491.

(73) Yan, Y.; Yin, Y.-X.; Xin, S.; Su, J.; Guo, Y.-G.; Wan, L.-J. High-safety lithium-sulfur battery with prelithiated Si/C anode and ionic liquid electrolyte. *Electrochim. Acta* **2013**, *91*, 58-61.

(74) Wang, L.; Wang, Y.; Xia, Y. A high performance lithium-ion sulfur battery based on a Li 2 S cathode using a dual-phase electrolyte. *Energy & Environmental Science* **2015**, *8*, 1551-1558.

(75) Yang, Y.; Zheng, G.; Misra, S.; Nelson, J.; Toney, M. F.; Cui, Y. High-Capacity Micrometer-Sized Li_2S Particles as Cathode Materials for Advanced Rechargeable Lithium-Ion Batteries. *J. Am. Chem. Soc.* **2012**, *134*, 15387-15394.

(76) Hassoun, J.; Scrosati, B. A High-Performance Polymer Tin Sulfur Lithium Ion Battery. *Angewandte Chemie International Edition* **2010**, *49*, 2371-2374.

(77) Zheng, S.; Chen, Y.; Xu, Y.; Yi, F.; Zhu, Y.; Liu, Y.; Yang, J.; Wang, C. In Situ Formed Lithium Sulfide/Microporous Carbon Cathodes for Lithium-Ion Batteries. *ACS Nano* **2013**, *7*, 10995-11003.

(78) Takeuchi, T.; Kageyama, H.; Nakanishi, K.; Ohta, T.; Sakuda, A.; Sakai, T.; Kobayashi, H.; Sakaebe, H.; Tatsumi, K.; Ogumi, Z. Application of graphite–solid electrolyte composite anode in all-solid-state lithium secondary battery with Li2S positive electrode. *Solid State Ionics* **2014**, *262*, 138-142.

(79) Zhang, K.; Wang, L.; Hu, Z.; Cheng, F.; Chen, J. Ultrasmall Li2S Nanoparticles Anchored in Graphene Nanosheets for High-Energy Lithium-Ion Batteries. *Scientific Reports* **2014**, *4*, 6467.

(80) Liu, Y.; Zhou, G.; Liu, K.; Cui, Y. Design of Complex Nanomaterials for Energy Storage: Past Success and Future Opportunity. *Acc. Chem. Res.* **2017**, *50*, 2895-2905.

(81) Wang, Z.; Fu, Y.; Zhang, Z.; Yuan, S.; Amine, K.; Battaglia, V.; Liu, G. Application of Stabilized Lithium Metal Powder (SLMP®) in graphite anode – A high efficient prelithiation method for lithium-ion batteries. *J. Power Sources* **2014**, *260*, 57-61.

(82) Jarvis, C.; Lain, M.; Gao, Y.; Yakovleva, M. A lithium ion cell containing a non-lithiated cathode. *J. Power Sources* **2005**, *146*, 331-334.

(83) Meyer, B.: Elemental sulphur. In *Inorganic Sulphur Chemistry*; Pegamon Press, 1966; pp 6.

(84) Villevieille, C.; Novak, P. A metastable [small beta]-sulfur phase stabilized at room temperature during cycling of high efficiency carbon fibre-sulfur composites for Li-S batteries. *Journal of Materials Chemistry A* **2013**, *1*, 13089-13092.

(85) Ferreira, A. G. M.; Lobo, L. Q. The low-pressure phase diagram of sulfur. *The Journal of Chemical Thermodynamics* **2011**, *43*, 95-104.

(86) Lv, D.; Zheng, J.; Li, Q.; Xie, X.; Ferrara, S.; Nie, Z.; Mehdi, L. B.; Browning, N. D.; Zhang, J. G.; Graff, G. L. High energy density lithium–sulfur batteries: challenges of thick sulfur cathodes. *Adv. Energy Mater.* **2015**, *5*, 1402290

(87) Meyer, B. Elemental sulfur. *Chem. Rev.* **1976**, *76*, 367-388.

(88) Shi, J.; Zhang, J.; Zhao, Y.; Yan, Z.; Hart, N.; Guo, J. Synthesis of Li_2S-Carbon Cathode Materials via Carbothermic Reduction of Li_2SO_4. **2019**, *7*.

(89) Hart, N.; Shi, J.; Zhang, J.; Fu, C.; Guo, J. Lithium Sulfide–Carbon Composites via Aerosol Spray Pyrolysis as Cathode Materials for Lithium–Sulfur Batteries. *Frontiers in Chemistry* **2018**, *6*.

(90) Su, D.; Zhou, D.; Wang, C.; Wang, G. Toward High Performance Lithium–Sulfur Batteries Based on Li2S Cathodes and Beyond: Status, Challenges, and Perspectives. *Adv. Funct. Mater.* **2018**, *28*, 1800154.

(91) Gerber, L. C.; Frischmann, P. D.; Fan, F. Y.; Doris, S. E.; Qu, X.; Scheuermann, A. M.; Persson, K.; Chiang, Y.-M.; Helms, B. A. Three-dimensional growth of Li_2S in lithium–sulfur batteries promoted by a redox mediator. *Nano Lett.* **2015**, *16*, 549-554.

(92) Liu, M.; Ren, Y. X.; Jiang, H. R.; Luo, C.; Kang, F. Y.; Zhao, T. S. An efficient Li_2S-based lithium-ion sulfur battery realized by a bifunctional electrolyte additive. *Nano Energy* **2017**, *40*, 240-247.

(93) Tsao, Y.; Lee, M.; Miller, E. C.; Gao, G.; Park, J.; Chen, S.; Katsumata, T.; Tran, H.; Wang, L.-W.; Toney, M. F.; Cui, Y.; Bao, Z. Designing a Quinone-Based Redox Mediator to Facilitate Li2S Oxidation in Li-S Batteries. *Joule* **2019**.

(94) Brügemann, L.; Gerndt, E. K. E. Detectors for X-ray diffraction and scattering: a user's overview. *Nuclear Instruments and Methods in Physics Research Section A: Accelerators, Spectrometers, Detectors and Associated Equipment* **2004**, *531*, 292-301.

(95) Baskaran, S. Structure and regulation of yeast glycogen synthase. Indiana University, 2010.

(96) Cao, Y.; Li, M.; Lu, J.; Liu, J.; Amine, K. Bridging the academic and industrial metrics for next-generation practical batteries. *Nature Nanotechnology* **2019**, *14*, 200-207.

(97) Deng, Z.; Zhang, Z.; Lai, Y.; Liu, J.; Li, J.; Liu, Y. Electrochemical Impedance Spectroscopy Study of a Lithium/Sulfur Battery: Modeling and Analysis of Capacity Fading. *J. Electrochem. Soc.* **2013**, *160*, A553-A558.

(98) Yuan, L.; Qiu, X.; Chen, L.; Zhu, W. New insight into the discharge process of sulfur cathode by electrochemical impedance spectroscopy. *J. Power Sources* **2009**, *189*, 127-132.

(99) Cañas, N. A.; Hirose, K.; Pascucci, B.; Wagner, N.; Friedrich, K. A.; Hiesgen, R. Investigations of lithium–sulfur batteries using electrochemical impedance spectroscopy. *Electrochim. Acta* **2013**, *97*, 42-51.

(100) Moy, D.; Manivannan, A.; Narayanan, S. R. Direct Measurement of Polysulfide Shuttle Current: A Window into Understanding the Performance of Lithium-Sulfur Cells. *J. Electrochem. Soc.* **2014**, *162*, A1-A7.

(101) Li, T.; Bai, X.; Gulzar, U.; Bai, Y.-J.; Capiglia, C.; Deng, W.; Zhou, X.; Liu, Z.; Feng, Z.; Proietti Zaccaria, R. A Comprehensive Understanding of Lithium–Sulfur Battery Technology. *Adv. Funct. Mater.* **2019**, *29*, 1901730.

(102) Hou, T.-Z.; Chen, X.; Peng, H.-J.; Huang, J.-Q.; Li, B.-Q.; Zhang, Q.; Li, B. Design Principles for Heteroatom-Doped Nanocarbon to Achieve Strong Anchoring of Polysulfides for Lithium–Sulfur Batteries. *Small* **2016**, *12*, 3283-3291.

(103) Chen, K.; Sun, Z.; Fang, R.; Shi, Y.; Cheng, H.-M.; Li, F. Metal–Organic Frameworks (MOFs)-Derived Nitrogen-Doped Porous Carbon Anchored on Graphene with Multifunctional Effects for Lithium–Sulfur Batteries. *Adv. Funct. Mater.* **2018**, *28*, 1707592.

(104) Yang, J.; Xie, J.; Zhou, X.; Zou, Y.; Tang, J.; Wang, S.; Chen, F.; Wang, L. Functionalized N-Doped Porous Carbon Nanofiber Webs for a Lithium–Sulfur Battery with High Capacity and Rate Performance. *The Journal of Physical Chemistry C* **2014**, *118*, 1800-1807.

(105) Li, M.; Zhang, Y.; Hassan, F. M.; Ahn, W.; Wang, X.; Liu, W.; Jiang, G.; Chen, Z. Compact High Volumetric and Areal Capacity Lithium Sulfur Battery through Rock Salt induced Nano-Architectured Sulfur Host. *Journal of Materials Chemistry A* **2017**, *5*, 21435-21441

(106) Wang, Z.; Zhou, L.; Lou, X. W. Metal Oxide Hollow Nanostructures for Lithium-ion Batteries. *Adv. Mater.* **2012**, *24*, 1903-1911.

(107) Wang, S. Q.; Zhang, J. Y.; Chen, C. H. Dandelion-like hollow microspheres of CuO as anode material for lithium-ion batteries. *Scripta Materialia* **2007**, *57*, 337-340.

(108) Lai, X.; Halpert, J. E.; Wang, D. Recent advances in micro-/nano-structured hollow spheres for energy applications: From simple to complex systems. *Energy & Environmental Science* **2012**, *5*, 5604-5618.

(109) Yu Chen, H. C., Deping Zeng, Yunbo Tian, Feng Chen, Jingwei Feng, and Jianlin Shi. Core/Shell Structured Hollow Mesoporous Nanocapsules: A Potential Platform for Simultaneous Cell Imaging and Anticancer Drug Delivery. *ACS Nano* **2010**, *4*, 6001.

(110) Chen, J.-F.; Ding, H.-M.; Wang, J.-X.; Shao, L. Preparation and characterization of porous hollow silica nanoparticles for drug delivery application. *Biomaterials* **2004**, *25*, 723-727.

(111) Fei, J. B.; Cui, Y.; Yan, X. H.; Qi, W.; Yang, Y.; Wang, K. W.; He, Q.; Li, J. B. Controlled Preparation of MnO2 Hierarchical Hollow Nanostructures and Their Application in Water Treatment. *Adv. Mater.* **2008**, *20*, 452-456.

(112) Wang, B.; Wu, H.; Yu, L.; Xu, R.; Lim, T. T.; Lou, X. W. Template-free formation of uniform urchin-like alpha-FeOOH hollow spheres with superior capability for water treatment. *Adv. Mater.* **2012**, *24*, 1111-1116.

(113) Shaojun Guo, Y. F., Shaojun Dong, and Erkang Wang. High-Efficiency and Low-Cost Hybrid Nanomaterial as Enhancing Electrocatalyst: Spongelike Au/Pt Core/Shell Nanomaterial with Hollow Cavity. *Journal of Physical Chemistry C* **2007**, *111*, 17104.

(114) Cao, A. M.; Hu, J. S.; Liang, H. P.; Wan, L. J. Self-assembled vanadium pentoxide (V2O5) hollow microspheres from nanorods and their application in lithium-ion batteries. *Angewandte Chemie International Edition* **2005**, *44*, 4391-4395.

(115) Duck-Rye Chang, S.-H. L., Sun-Wook Kim, Hee-Tak Kim. Binary electrolyte based on tetra(ethylene glycol) dimethyl ether and 1,3-dioxolane for lithium–sulfur battery. *J. Power Sources* **2002**, *112*, 452.

(116) Zheng, J.; Lv, D.; Gu, M.; Wang, C.; Zhang, J. G.; Liu, J.; Xiao, J. How to Obtain Reproducible Results for Lithium Sulfur Batteries? *J. Electrochem. Soc.* **2013**, *160,* A2288-A2292.

(117) Ma, G.; Wen, Z.; Wang, Q.; Shen, C.; Peng, P.; Jin, J.; Wu, X. Enhanced performance of lithium sulfur battery with self-assembly polypyrrole nanotube film as the functional interlayer. *J. Power Sources* **2015**, *273*, 511-516.

(118) Chen, H. W.; Wang, C. H.; Dai, Y. F.; Qiu, S. Q.; Yang, J. L.; Lu, W.; Chen, L. W. Rational Design of Cathode Structure for High Rate Performance Lithium-Sulfur Batteries. *Nano Lett.* **2015**, *15*, 5443-5448.

(119) Zhu, L.; Peng, H.-J.; Liang, J.; Huang, J.-Q.; Chen, C.-M.; Guo, X.; Zhu, W.; Li, P.; Zhang, Q. Interconnected carbon nanotube/graphene nanosphere scaffolds as free-standing paper electrode for high-rate and ultra-stable lithium–sulfur batteries. *Nano Energy* **2015**, *11*, 746-755.

(120) Jin, F.; Xiao, S.; Lu, L.; Wang, Y. Efficient Activation of High-Loading Sulfur by Small CNTs Confined Inside a Large CNT for High-Capacity and High-Rate Lithium-Sulfur Batteries. *Nano Lett* **2016**, *16*, 440-447.

(121) Kim, H.; Lee, J.; Ahn, H.; Kim, O.; Park, M. J. Synthesis of three-dimensionally interconnected sulfur-rich polymers for cathode materials of high-rate lithium-sulfur batteries. *Nat. Commun.* **2015**, *6*, 7278.

(122) Hwang, J.-Y.; Kim, H. M.; Lee, S.-K.; Lee, J.-H.; Abouimrane, A.; Khaleel, M. A.; Belharouak, I.; Manthiram, A.; Sun, Y.-K. High-Energy, High-Rate, Lithium-Sulfur Batteries: Synergetic Effect of Hollow TiO2-Webbed Carbon Nanotubes and a Dual Functional Carbon-Paper Interlayer. *Adv. Energy Mater.* **2016**, *6*, 1501480.

(123) Zhang, C.; Wu, H. B.; Yuan, C.; Guo, Z.; Lou, X. W. Confining Sulfur in Double-Shelled Hollow Carbon Spheres for Lithium–Sulfur Batteries. *Angewandte Chemie International Edition* **2012**, *124*, 9730.

(124) Wang, X.; Li, G.; Li, J.; Zhang, Y.; Wook, A.; Yu, A.; Chen, Z.: Structural and chemical synergistic encapsulation of polysulfides enables ultralong-life lithium–sulfur batteries. In *Energy Environ. Sci.*, 2016; pp 10.1039/C1036EE00194G.

(125) Zhou, W.; Xiao, X.; Cai, M.; Yang, L. Polydopamine-coated, nitrogen-doped, hollow carbon-sulfur double-layered core-shell structure for improving lithium-sulfur batteries. *Nano Lett.* **2014**, *14*, 5250-5256.

(126) Liu, S.; Li, Y.; Hong, X.; Xu, J.; Zheng, C.; Xie, K. Reduced graphene oxide-hollow carbon sphere nanostructure cathode material with ultra-high sulfur content for high performance lithium-sulfur batteries. *Electrochim. Acta* **2016**, *188,* 516-522.

(127) Manthiram, A.; Chung, S. H.; Zu, C. Lithium-sulfur batteries: progress and prospects. *Adv. Mater.* **2015**, *27*, 1980-2006.

(128) Liu, J.; Yang, T.; Wang, D. W.; Lu, G. Q.; Zhao, D.; Qiao, S. Z. A facile soft-template synthesis of mesoporous polymeric and carbonaceous nanospheres. *Nat. Commun.* **2013**, *4*, 2798.

(129) Tang, J.; J. Liu; Salunkhe, R. R.; Wangd, T.; Yamauchi, Y. Nitrogen-doped hollow carbon spheres with large mesoporous shells engineered from diblock copolymer micelles. *ChemComm* **2016**, *52*, 55.

(130) Guo, P.; Song, H.; Chen, X. Hollow graphene oxide spheres self-assembled by W/O emulsion. *Journal of Materials Chemistry* **2010**, *20*, 4867.

(131) Xia, Y.; Wang, B.; Zhao, X.; Wang, G.; Wang, H. Core-shell composite of hierarchical MoS2 nanosheets supported on graphitized hollow carbon microspheres for high performance lithium-ion batteries. *Electrochim. Acta* **2016**, *187*, 55-64.

(132) Pickering, S. U. Emulsions. *Journal of the Chemical Society, Transactions* **1907**, *196*, 2001.

(133) Gonzenbach, U. T.; Studart, A. R.; Tervoort, E.; Gauckler, L. J. Ultrastable particle-stabilized foams. *Angewandte Chemie International Edition* **2006**, *45*, 3526-3530.

(134) Helen Hassander, B. J. a. B. T. The Mechanism of Emulsion Stabilization by Small Silica (Ludox) Particles. *Colloids and Surfaces* **1989**, *40*, 93-105.

(135) Piazza, E. V. a. R. Pickering Emulsions: Interfacial Tension, Colloidal Layer Morphology, and Trapped-Particle Motion. *Langmuir* **2003**, *19*, 6650.

(136) Dickinson, E. Use of nanoparticles and microparticles in the formation and stabilization of food emulsions. *Trends in Food Science & Technology* **2012**, *24*, 4-12.

(137) Dickinson, E. Food emulsions and foams: Stabilization by particles. *Current Opinion in Colloid & Interface Science* **2010**, *15*, 40-49.

(138) Binks, B. P.; Horozov, T. S. Aqueous Foams Stabilized Solely by Silica Nanoparticles. *Angewandte Chemie* **2005**, *117*, 3788-3791.

(139) Bernard P. Binks, R. M., Steven P. Armes,Syuji Fujii, and Andreas Schmid. pH-Responsive Aqueous Foams Stabilized by Ionizable Latex Particles. *Langmuir* **2007**, *23*, 8691.

(140) Nie, H.; Zhang, H.; Zhang, Y.; Liu, T.; Li, J.; Lai, Q. Nitrogen enriched mesoporous carbon as a high capacity cathode in lithium-oxygen batteries. *Nanoscale* **2013**, *5*, 8484-8487.

(141) Brown, E. N.; Kessler, M. R.; Sottos, N. R.; White, S. R. In situpoly(urea-formaldehyde) microencapsulation of dicyclopentadiene. *Journal of Microencapsulation* **2010**, *20*, 719-730.

(142) Yoku Shiraisw, H. S. a. H. K. The Effect of Agitation on the Rate of Emulsion Polymerization of Styrene *Journal of Chemical Engineering of Japan* **1968**, *2*, 64.

(143) Thompson, K. L.; Mable, C. J.; Lane, J. A.; Derry, M. J.; Fielding, L. A.; Armes, S. P. Preparation of Pickering double emulsions using block copolymer worms. *Langmuir* **2015**, *31*, 4137-4144.

(144) Dickson, A. G.; Millero, F. J. A comparison of the equilibrium constants for the dissociation of carbonic acid in seawater media. *Deep Sea Research Part A. Oceanographic Research Papers* **1987**, *34*, 1733-1743.

(145) Sebra, F. Microfoams--An Unexploited Colloid System. *Journal of Colloid and Interface Science* **1970**, *35*, 643.

(146) Gao, X.; Wang, L.-J.; Wu, C.; Cheng, Y.-W.; Li, X. Novel Bubble–Emulsion Hydrodynamic Model for Gas–Solid Bubbling Fluidized Beds. *Ind. Eng. Chem. Res.* **2013**, *52*, 10835-10844.

(147) Taylor, P. Ostwald ripening in emulsions. *Advances In Colloid and Interface Science* **1998**, *75*, 107.

(148) Hirofumi Daiguji, T. M., Hiroki Kinoshita, Takayuki Oyabu, and; Takemura, F. Fabrication of Hollow Melamine-Formaldehyde Microcapsules from Microbubble Templates. *Journal Physical Chemistry B* **2007**, *111*, 8879-8884.

(149) Zhou, J.; Qiao, X.; Binks, B. P.; Sun, K.; Bai, M.; Li, Y.; Liu, Y. Magnetic Pickering emulsions stabilized by Fe3O4 nanoparticles. *Langmuir* **2011**, *27*, 3308-3316.

(150) Fang, F. F.; Liu, Y. D.; Choi, H. J. Synthesis and electrorheological characteristics of polyaniline/organoclay nanoparticles via Pickering emulsion polymerization. *Smart Materials and Structures* **2010**, *19*, 124002.

(151) Nawaz, M.; Miran, W.; Jang, J.; Lee, D. S.: Stabilization of Pickering emulsion with surface-modified titanium dioxide for enhanced photocatalytic degradation of Direct Red 80. In *Catal. Today,* 2016; pp 10.1016/j.cattod.2016.1002.1017

(152) Pang, Q.; Tang, J.; Huang, H.; Liang, X.; Hart, C.; Tam, K. C.; Nazar, L. F. A Nitrogen and Sulfur Dual-Doped Carbon Derived from Polyrhodanine@Cellulose for Advanced Lithium-Sulfur Batteries. *Adv. Mater.* **2015**, *27*, 6021-6028.

(153) Pang, Q.; Nazar, L. F. Long-Life and High-Areal-Capacity Li-S Batteries Enabled by a Light-Weight Polar Host with Intrinsic Polysulfide Adsorption. *ACS Nano* **2016**, *10*, 4111-4118.

(154) Li, Y.; Li, T. T.; Yao, M.; Liu, S. Q. Metal-free nitrogen-doped hollow carbon spheres synthesized by thermal treatment of poly(o-phenylenediamine) for oxygen reduction reaction in direct methanol fuel cell applications. *Journal of Materials Chemistry* **2012**, *22*, 10911-10917.

(155) Jia, R.; Chen, J.; Zhao, J.; Zheng, J.; Song, C.; Li, L.; Zhu, Z. Synthesis of highly nitrogen-doped hollow carbon nanoparticles and their excellent electrocatalytic properties in dye-sensitized solar cells. *Journal of Materials Chemistry* **2010**, *20*, 10829.

(156) Han, J.; Xu, G.; Ding, B.; Pan, J.; Dou, H.; MacFarlane, D. R. Porous nitrogen-doped hollow carbon spheres derived from polyaniline for high performance supercapacitors. *Journal of Material Chemistry A* **2014**, *2*, 5352-5357.

(157) Feng, S.; Li, W.; Shi, Q.; Li, Y.; Chen, J.; Ling, Y.; Asiri, A. M.; Zhao, D. Synthesis of nitrogen-doped hollow carbon nanospheres for CO2 capture. *ChemComm* **2014**, *50*, 329-331.

(158) Song, M. Y.; Yang, D.-S.; Singh, K. P.; Yuan, J.; Yu, J.-S. Nitrogen-doped hollow carbon spheres with highly graphitized mesoporous shell: Role of Fe for oxygen evolution reaction. *Applied Catalysis B: Environmental* **2016**, *191*, 202-208.

(159) Wen, Y.; Wang, B.; Luo, B.; Wang, L. Long-Term Cycling Performance of Nitrogen-Doped Hollow Carbon Nanospheres as Anode Materials for Sodium-Ion Batteries. *European Journal of Inorganic Chemistry* **2016**, *2016*, 2051-2055.

(160) Zhou, G. M.; Zhao, Y. B.; Manthiram, A. Dual-Confined Flexible Sulfur Cathodes Encapsulated in Nitrogen-Doped Double-Shelled Hollow Carbon Spheres and Wrapped with Graphene for Li-S Batteries. *Adv. Energy Mater.* **2015**, *5*, 1402263.

(161) Pei, F.; An, T.; Zang, J.; Zhao, X.; Fang, X.; Zheng, M.; Dong, Q.; Zheng, N. From Hollow Carbon Spheres to N-Doped Hollow Porous Carbon Bowls: Rational Design of Hollow Carbon Host for Li-S Batteries. *Adv. Energy Mater.* **2016**, *6*, 1502539.

(162) Ji, X.; Lee, K. T.; Nazar, L. F. A highly ordered nanostructured carbon–sulphur cathode for lithium–sulphur batteries. *Nature materials* **2009**, *8*, 500-506.

(163) Sun, X. G.; Wang, X.; Mayes, R. T.; Dai, S. Lithium-sulfur batteries based on nitrogen-doped carbon and an ionic-liquid electrolyte. *ChemSusChem* **2012**, *5*, 2079-2085.

(164) Zhou, G.; Zhao, Y.; Manthiram, A. Dual-Confined Flexible Sulfur Cathodes Encapsulated in Nitrogen-Doped Double-Shelled Hollow Carbon Spheres and Wrapped with Graphene for Li–S Batteries. *Adv. Energy Mater.* **2015**, *5*, 1402263.

(165) Lina Wang , J. L., Shouyi Yuan , Yonggang Wang and Yongyao Xia To mitigate self-discharge of lithium–sulfur batteries by optimizing ionic liquid electrolytes. *Energy Environ. Science* **2016**, *9*, 224-231.

(166) Wang, L.; Wang, Y. G.; Xia, Y. Y. A high performance lithium-ion sulfur battery based on a Li2S cathode using a dual-phase electrolyte. *Energy & Environmental Science* **2015**, *8*, 1551-1558.

(167) Chen, S.; Dai, F.; Gordin, M. L.; Yu, Z.; Gao, Y.; Song, J.; Wang, D. Functional Organosulfide Electrolyte Promotes an Alternate Reaction Pathway to Achieve High Performance in Lithium-Sulfur Batteries. *Angew Chem Int Ed Engl* **2016**, *55*, 4231-4235.

(168) Zhao, M.; Peng, H.-J.; Wei, J.-Y.; Huang, J.-Q.; Li, B.-Q.; Yuan, H.; Zhang, Q. Dictating High-Capacity Lithium–Sulfur Batteries through Redox-Mediated Lithium Sulfide Growth. *Small Methods* **2020**, *4*, 1900344.

(169) Hwa, Y.; Seo, H. K.; Yuk, J.-m.; Cairns, E. J. Freeze-Dried Sulfur–Graphene Oxide–Carbon Nanotube Nanocomposite for High Sulfur-Loading Lithium/Sulfur Cells. *Nano Lett.* **2017**, *17*, 7086-7094.

(170) Pang, Q.; Liang, X.; Kwok, C. Y.; Kulisch, J.; Nazar, L. F. A Comprehensive Approach toward Stable Lithium–Sulfur Batteries with High Volumetric Energy Density. *Adv. Energy Mater.* **2017**, *7*, 1601630-n/a.

(171) Li, G.; Chen, Z.; Lu, J. Lithium-Sulfur Batteries for Commercial Applications. *Chem* **2018**, *4*, 3-7.

(172) Peng, H. J.; Huang, J. Q.; Cheng, X. B.; Zhang, Q. Review on High-Loading and High-Energy Lithium–Sulfur Batteries. *Adv. Energy Mater.* **2017**, *7*, 1700260.

(173) Chung, S. H.; Manthiram, A. Rational Design of Statically and Dynamically Stable Lithium–Sulfur Batteries with High Sulfur Loading and Low Electrolyte/Sulfur Ratio. *Adv. Mater.* **2018**, *30*.

(174) Chung, S.-H.; Luo, L.; Manthiram, A. TiS2–Polysulfide Hybrid Cathode with High Sulfur Loading and Low Electrolyte Consumption for Lithium–Sulfur Batteries. *ACS Energy Lett.* **2018**, *3*, 568-573.

(175) Li, G.; Lei, W.; Luo, D.; Deng, Y.; Deng, Z.; Wang, D.; Yu, A.; Chen, Z. Stringed "tube on cube" nanohybrids as compact cathode matrix for high-loading and lean-electrolyte lithium–sulfur batteries. *Energy & Environmental Science* **2018**.

(176) Yang, X.; Li, X.; Adair, K.; Zhang, H.; Sun, X. Structural Design of Lithium–Sulfur Batteries: From Fundamental Research to Practical Application. *Electrochemical Energy Reviews* **2018**.

(177) Pang, Q.; Nazar, L. F. Long-Life and High-Areal-Capacity Li–S Batteries Enabled by a Light-Weight Polar Host with Intrinsic Polysulfide Adsorption. *ACS Nano* **2016**, *10*, 4111-4118.

(178) Hu, C.; Kirk, C.; Cai, Q.; Cuadrado-Collados, C.; Silvestre-Albero, J.; Rodríguez-Reinoso, F.; Biggs, M. J. A High-Volumetric-Capacity Cathode Based on Interconnected Close-Packed N-Doped Porous Carbon Nanospheres for Long-Life Lithium–Sulfur Batteries. *Adv. Energy Mater.* **2017**, *7*.

(179) Zhu, L.; Zhu, W.; Cheng, X.-B.; Huang, J.-Q.; Peng, H.-J.; Yang, S.-H.; Zhang, Q. Cathode materials based on carbon nanotubes for high-energy-density lithium–sulfur batteries. *Carbon* **2014**, *75*, 161-168.

(180) Mao, Y.; Li, G.; Guo, Y.; Li, Z.; Liang, C.; Peng, X.; Lin, Z. Foldable interpenetrated metal-organic frameworks/carbon nanotubes thin film for lithium–sulfur batteries. *Nat. Commun.* **2017**, *8*, 14628.

(181) Ma, Y.; Zhang, H.; Wu, B.; Wang, M.; Li, X.; Zhang, H. Lithium sulfur primary battery with super high energy density: based on the cauliflower-like structured C/S cathode. *Scientific reports* **2015**, *5*, 14949.

(182) Gueon, D.; Hwang, J. T.; Yang, S. B.; Cho, E.; Sohn, K.; Yang, D.-K.; Moon, J. H. Spherical Macroporous Carbon Nanotube Particles with Ultrahigh Sulfur Loading for Lithium–Sulfur Battery Cathodes. *ACS Nano* **2018**, *12*, 226-233.

(183) Shahriary, L.; Athawale, A. A. Graphene oxide synthesized by using modified hummers approach. *Int J Renew Energy Environ Eng* **2014**, *2*, 58-63.

(184) Moy, D.; Manivannan, A.; Narayanan, S. R. Direct Measurement of Polysulfide Shuttle Current: A Window into Understanding the Performance of Lithium-Sulfur Cells. *J. Electrochem. Soc.* **2015**, *162*, A1-A7.

(185) Jung, D. S.; Hwang, T. H.; Lee, J. H.; Koo, H. Y.; Shakoor, R. A.; Kahraman, R.; Jo, Y. N.; Park, M.-S.; Choi, J. W. Hierarchical Porous Carbon by Ultrasonic Spray Pyrolysis Yields Stable Cycling in Lithium–Sulfur Battery. *Nano Lett.* **2014**, *14*, 4418-4425.

(186) Ma, J.; Fang, Z.; Yan, Y.; Yang, Z.; Gu, L.; Hu, Y.-S.; Li, H.; Wang, Z.; Huang, X. Novel Large-Scale Synthesis of a C/S Nanocomposite with Mixed Conducting Networks through a Spray Drying Approach for Li–S Batteries. *Adv. Energy Mater.* **2015**, *5*, 1500046-n/a.

(187) Shen, Y.; Jing, T.; Ren, W.; Zhang, J.; Jiang, Z.-G.; Yu, Z.-Z.; Dasari, A. Chemical and thermal reduction of graphene oxide and its electrically conductive polylactic acid nanocomposites. *Compos. Sci. Technol.* **2012**, *72*, 1430-1435.

(188) Kuhnhenn, M.; Joensen, T. V.; Reck, M.; Roisman, I. V.; Tropea, C. Study of the internal flow in a rotary atomizer and its influence on the properties of the resulting spray. *Int. J. Multiphase Flow* **2018**, *100*, 30-40.

(189) Bastan, F. E.; Erdogan, G.; Moskalewicz, T.; Ustel, F. Spray drying of hydroxyapatite powders: The effect of spray drying parameters and heat treatment on the particle size and morphology. *J. Alloys Compd.* **2017**, *724*, 586-596.

(190) Mao, Z.; Farkhondeh, M.; Pritzker, M.; Fowler, M.; Chen, Z. Multi-Particle Model for a Commercial Blended Lithium-Ion Electrode. *J. Electrochem. Soc.* **2016**, *163*, A458-A469.

(191) Washburn, E. W. The Dynamics of Capillary Flow. *Phys. Rev.* **1921**, *17*, 273-283.

(192) Yuan, Y.; Tan, G.; Wen, J.; Lu, J.; Ma, L.; Liu, C.; Zuo, X.; Shahbazian-Yassar, R.; Wu, T.; Amine, K. Encapsulating Various Sulfur Allotropes within Graphene Nanocages for Long-Lasting Lithium Storage. *Adv. Funct. Mater.* **2018**.

(193) Chang, D.-R.; Lee, S.-H.; Kim, S.-W.; Kim, H.-T. Binary electrolyte based on tetra(ethylene glycol) dimethyl ether and 1,3-dioxolane for lithium–sulfur battery. *J. Power Sources* **2002**, *112*, 452-460.

(194) Jiao, S.; Zheng, J.; Li, Q.; Li, X.; Engelhard, M. H.; Cao, R.; Zhang, J.-G.; Xu, W. Behavior of lithium metal anodes under various capacity utilization and high current density in lithium metal batteries. *Joule* **2018**, *2*, 110-124.

(195) Zhong, Y.; Xia, X.; Deng, S.; Zhan, J.; Fang, R.; Xia, Y.; Wang, X.; Zhang, Q.; Tu, J. Popcorn Inspired Porous Macrocellular Carbon: Rapid Puffing Fabrication from Rice and Its Applications in Lithium–Sulfur Batteries. *Adv. Energy Mater.* **2018**, *8*.

(196) Fan, F. Y.; Chiang, Y.-M. Electrodeposition Kinetics in Li-S Batteries: Effects of Low Electrolyte/Sulfur Ratios and Deposition Surface Composition. *J. Electrochem. Soc.* **2017**, *164*, A917-A922.

(197) Holzapfel, M.; Martinent, A.; Alloin, F.; Le Gorrec, B.; Yazami, R.; Montella, C. First lithiation and charge/discharge cycles of graphite materials, investigated by electrochemical impedance spectroscopy. *Journal of Electroanalytical Chemistry* **2003**, *546*, 41-50.

(198) Illig, J.; Ender, M.; Chrobak, T.; Schmidt, J. P.; Klotz, D.; Ivers-Tiffée, E. Separation of charge transfer and contact resistance in LiFePO4-cathodes by impedance modeling. *J. Electrochem. Soc.* **2012**, *159*, A952-A960.

(199) Shen, C.; Xie, J.; Zhang, M.; Zheng, J. P.; Hendrickson, M.; Plichta, E. J. Communication—Effect of Lithium Polysulfide Solubility on Capacity of Lithium-Sulfur Cells. *J. Electrochem. Soc.* **2017**, *164*, A1220-A1222.

(200) Li, G.; Wang, X.; Seo, M. H.; Li, M.; Ma, L.; Yuan, Y.; Wu, T.; Yu, A.; Wang, S.; Lu, J.; Chen, Z. Chemisorption of polysulfides through redox reactions with organic molecules for lithium-sulfur batteries. *Nat Commun* **2018**, *9*, 705.

(201) Conder, J.; Bouchet, R.; Trabesinger, S.; Marino, C.; Gubler, L.; Villevieille, C. Direct observation of lithium polysulfides in lithium–sulfur batteries using operando X-ray diffraction. *Nat. Energy* **2017**, *2*, 17069.

(202) Shen, C.; Xie, J.; Zhang, M.; Andrei, P.; Hendrickson, M.; Plichta, E. J.; Zheng, J. P. Understanding the role of lithium polysulfide solubility in limiting lithium-sulfur cell capacity. *Electrochim. Acta* **2017**, *248*, 90-97.

(203) Chung, S.-H.; Manthiram, A. Designing Lithium-Sulfur Cells with Practically Necessary Parameters. *Joule* **2018**, *2*, 710-724.

(204) Gao, Y.; Yan, Z.; Gray, J. L.; He, X.; Wang, D.; Chen, T.; Huang, Q.; Li, Y. C.; Wang, H.; Kim, S. H.; Mallouk, T. E.; Wang, D. Polymer–inorganic solid–electrolyte interphase for stable lithium metal batteries under lean electrolyte conditions. *Nature Materials* **2019**.

(205) Ghazi, Z. A.; Sun, Z.; Sun, C.; Qi, F.; An, B.; Li, F.; Cheng, H.-M. Key Aspects of Lithium Metal Anodes for Lithium Metal Batteries. *Small* **2019**, *15*, 1900687.

(206) Li, Y.; Fitch, B. Effective enhancement of lithium-ion battery performance using SLMP. *Electrochem. commun.* **2011**, *13*, 664-667.

(207) Meini, S.; Elazari, R.; Rosenman, A.; Garsuch, A.; Aurbach, D. The Use of Redox Mediators for Enhancing Utilization of Li_2S Cathodes for Advanced Li–S Battery Systems. *The Journal of Physical Chemistry Letters* **2014**, *5*, 915-918.

(208) Ito, S.; Nakakita, M.; Aihara, Y.; Uehara, T.; Machida, N. A synthesis of crystalline Li7P3S11 solid electrolyte from 1,2-dimethoxyethane solvent. *J. Power Sources* **2014**, *271*, 342-345.

(209) Liu, Z.; Fu, W.; Payzant, E. A.; Yu, X.; Wu, Z.; Dudney, N. J.; Kiggans, J.; Hong, K.; Rondinone, A. J.; Liang, C. Anomalous high ionic conductivity of nanoporous β-Li_3PS_4. *J. Am. Chem. Soc.* **2013**, *135*, 975-978.

(210) Zhu, Y.; He, X.; Mo, Y. First principles study on electrochemical and chemical stability of solid electrolyte–electrode interfaces in all-solid-state Li-ion batteries. *Journal of Materials Chemistry A* **2016**, *4*, 3253-3266.

(211) Luo, C.; Ji, X.; Chen, J.; Gaskell, K. J.; He, X.; Liang, Y.; Jiang, J.; Wang, C. Solid-State Electrolyte Anchored with a Carboxylated Azo Compound for All-Solid-State Lithium Batteries. *Angewandte Chemie* **2018**, *130*, 8703-8707.

(212) Zheng, J.; Tang, M.; Hu, Y.-Y. Lithium Ion Pathway within $Li_7La_3Zr_2O_{12}$-Polyethylene Oxide Composite Electrolytes. *Angew Chem Int Ed Engl* **2016**, *55*, 12538-12542.

(213) Lau, J.; DeBlock, R. H.; Butts, D. M.; Ashby, D. S.; Choi, C. S.; Dunn, B. S. Sulfide Solid Electrolytes for Lithium Battery Applications. *Adv. Energy Mater.* **2018**, *8*, 1800933.

(214) Richards, W. D.; Miara, L. J.; Wang, Y.; Kim, J. C.; Ceder, G. Interface Stability in Solid-State Batteries. *Chemistry of Materials* **2016**, *28*, 266-273.

(215) Zhu, Y.; He, X.; Mo, Y. Origin of Outstanding Stability in the Lithium Solid Electrolyte Materials: Insights from Thermodynamic Analyses Based on First-Principles Calculations. *ACS Appl. Mater. Interfaces* **2015**, *7*, 23685-23693.

(216) Zhang, Z.; Chen, S.; Yang, J.; Wang, J.; Yao, L.; Yao, X.; Cui, P.; Xu, X. Interface Re-Engineering of $Li_{10}GeP_2S_{12}$ Electrolyte and Lithium anode for All-Solid-State Lithium Batteries with Ultralong Cycle Life. *ACS Appl. Mater. Interfaces* **2018**, *10*, 2556-2565.

(217) Wenzel, S.; Leichtweiss, T.; Krüger, D.; Sann, J.; Janek, J. Interphase formation on lithium solid electrolytes—An in situ approach to study interfacial reactions by photoelectron spectroscopy. *Solid State Ionics* **2015**, *278*, 98-105.

(218) Wang, Q.; Zakeeruddin, S. M.; Wang, D.; Exnar, I.; Grätzel, M. Redox Targeting of Insulating Electrode Materials: A New Approach to High-Energy-Density Batteries. *Angewandte Chemie* **2006**, *118*, 8377-8380.

(219) Yao, X.; Dong, Q.; Cheng, Q.; Wang, D. Why Do Lithium–Oxygen Batteries Fail: Parasitic Chemical Reactions and Their Synergistic Effect. *Angewandte Chemie International Edition* **2016**, *55*, 11344-11353.

(220) Guo, Z.; Li, C.; Liu, J.; Wang, Y.; Xia, Y. A Long-Life Lithium–Air Battery in Ambient Air with a Polymer Electrolyte Containing a Redox Mediator. *Angewandte Chemie International Edition* **2017**, *56*, 7505-7509.

(221) Yang, Y.; Zhong, Y.; Shi, Q.; Wang, Z.; Sun, K.; Wang, H. Electrocatalysis in Lithium Sulfur Batteries under Lean Electrolyte Conditions. *Angewandte Chemie* **2018**, *130*, 15775-15778.

(222) Peng, H.-J.; Zhang, G.; Chen, X.; Zhang, Z.-W.; Xu, W.-T.; Huang, J.-Q.; Zhang, Q. Enhanced Electrochemical Kinetics on Conductive Polar Mediators for Lithium–Sulfur Batteries. *Angewandte Chemie International Edition* **2016**, *55*, 12990-12995.

(223) Dietrich, C.; Weber, D. A.; Sedlmaier, S. J.; Indris, S.; Culver, S. P.; Walter, D.; Janek, J.; Zeier, W. G. Lithium ion conductivity in Li2S–P2S5 glasses – building units and local structure evolution during the crystallization of superionic conductors Li3PS4, Li7P3S11 and Li4P2S7. *Journal of Materials Chemistry A* **2017**, *5*, 18111-18119.

(224) Lu, Y.; Gu, S.; Hong, X.; Rui, K.; Huang, X.; Jin, J.; Chen, C.; Yang, J.; Wen, Z. Pre-modified Li3PS4 based interphase for lithium anode towards high-performance Li-S battery. *Energy Storage Materials* **2018**, *11*, 16-23.

(225) Teragawa, S.; Aso, K.; Tadanaga, K.; Hayashi, A.; Tatsumisago, M. Liquid-phase synthesis of a Li 3 PS 4 solid electrolyte using N-methylformamide for all-solid-state lithium batteries. *Journal of Materials Chemistry A* **2014**, *2*, 5095-5099.

(226) Gao, Z.; Sun, H.; Fu, L.; Ye, F.; Zhang, Y.; Luo, W.; Huang, Y. Promises, Challenges, and Recent Progress of Inorganic Solid-State Electrolytes for All-Solid-State Lithium Batteries. *Adv. Mater.* **2018**, *30*.

(227) Sumita, M.; Tanaka, Y.; Ikeda, M.; Ohno, T. Charged and Discharged States of Cathode/Sulfide Electrolyte Interfaces in All-Solid-State Lithium Ion Batteries. *The Journal of Physical Chemistry C* **2016**, *120*, 13332-13339.

(228) Yang, Y.; Wu, Q.; Cui, Y.; Chen, Y.; Shi, S.; Wang, R.-Z.; Yan, H. Elastic Properties, Defect Thermodynamics, Electrochemical Window, Phase Stability, and Li+ Mobility of Li_3PS_4: Insights from First-Principles Calculations. *ACS Appl. Mater. Interfaces* **2016**, *8*, 25229-25242.

(229) Hakari, T.; Deguchi, M.; Mitsuhara, K.; Ohta, T.; Saito, K.; Orikasa, Y.; Uchimoto, Y.; Kowada, Y.; Hayashi, A.; Tatsumisago, M. Structural and Electronic-State Changes of a Sulfide Solid Electrolyte during the Li Deinsertion–Insertion Processes. *Chemistry of Materials* **2017**, *29*, 4768-4774.

(230) Zhang, S. S. Role of LiNO3 in rechargeable lithium/sulfur battery. *Electrochim. Acta* **2012**, *70*, 344-348.

(231) Berger, A.; Freiberg, A. T. S.; Siebel, A.; Thomas, R.; Patel, M. U. M.; Tromp, M.; Gasteiger, H. A.; Gorlin, Y. The Importance of Chemical Reactions in the Charging Process of Lithium-Sulfur Batteries. *J. Electrochem. Soc.* **2018**, *165*, A1288-A1296.

(232) Li, M.; Zhang, Y.; Bai, Z.; Liu, W. W.; Liu, T.; Gim, J.; Jiang, G.; Yuan, Y.; Luo, D.; Feng, K.; Yassar, R. S.; Wang, X.; Chen, Z.; Lu, J. A Lithium–Sulfur Battery using a 2D Current Collector Architecture with a Large-Sized Sulfur Host Operated under High Areal Loading and Low E/S Ratio. *Adv. Mater.* **2018**, *30*, 1804271.

(233) Li, G.; Wang, S.; Zhang, Y.; Li, M.; Chen, Z.; Lu, J. Revisiting the Role of Polysulfides in Lithium–Sulfur Batteries. *Adv. Mater.* **2018**, *30*, 1705590.

(234) Gorlin, Y.; Patel, M. U. M.; Freiberg, A.; He, Q.; Piana, M.; Tromp, M.; Gasteiger, H. A. Understanding the Charging Mechanism of Lithium-Sulfur Batteries Using Spatially Resolved Operando X-Ray Absorption Spectroscopy. *J. Electrochem. Soc.* **2016**, *163*, A930-A939.

(235) Partovi-Azar, P.; Kühne, T. D.; Kaghazchi, P. Evidence for the existence of Li2S2 clusters in lithium–sulfur batteries: ab initio Raman spectroscopy simulation. *Physical Chemistry Chemical Physics* **2015**, *17*, 22009-22014.

(236) Dietrich, C.; Koerver, R.; Gaultois, M. W.; Kieslich, G.; Cibin, G.; Janek, J.; Zeier, W. G. Spectroscopic characterization of lithium thiophosphates by XPS and XAS – a model to help monitor interfacial reactions in all-solid-state batteries. *Physical Chemistry Chemical Physics* **2018**, *20*, 20088-20095.

(237) Lin, Z.; Liu, Z.; Fu, W.; Dudney, N. J.; Liang, C. Lithium Polysulfidophosphates: A Family of Lithium-Conducting Sulfur-Rich Compounds for Lithium–Sulfur Batteries. *Angewandte Chemie* **2013**, *125*, 7608-7611.

(238) Hwa, Y.; Zhao, J.; Cairns, E. J. Lithium Sulfide (Li2S)/Graphene Oxide Nanospheres with Conformal Carbon Coating as a High-Rate, Long-Life Cathode for Li/S Cells. *Nano Lett.* **2015**, *15*, 3479-3486.

(239) Chung, S.-H.; Han, P.; Chang, C.-H.; Manthiram, A. A Shell-Shaped Carbon Architecture with High-Loading Capability for Lithium Sulfide Cathodes. *Adv. Energy Mater.* **2017**, *7*, 1700537.

(240) Seh, Z. W.; Zhang, Q.; Li, W.; Zheng, G.; Yao, H.; Cui, Y. Stable cycling of lithium sulfide cathodes through strong affinity with a bifunctional binder. *Chemical Science* **2013**, *4*, 3673-3677.

(241) Fan, L.; Li, M.; Li, X.; Xiao, W.; Chen, Z.; Lu, J. Interlayer Material Selection for Lithium-Sulfur Batteries. *Joule* **2019**, *3*, 361-386.

(242) Gao, Y.; Wang, D.; Li, Y. C.; Yu, Z.; Mallouk, T. E.; Wang, D. Salt-Based Organic–Inorganic Nanocomposites: Towards A Stable Lithium Metal/Li10GeP2S12 Solid Electrolyte Interface. *Angewandte Chemie International Edition* **2018**, *57*, 13608-13612.

(243) Banerjee, A.; Park, K. H.; Heo, J. W.; Nam, Y. J.; Moon, C. K.; Oh, S. M.; Hong, S.-T.; Jung, Y. S. Na3SbS4: A Solution Processable Sodium Superionic Conductor for All-Solid-State Sodium-Ion Batteries. *Angewandte Chemie International Edition* **2016**, *55*, 9634-9638.

(244) Chi, X.; Liang, Y.; Hao, F.; Zhang, Y.; Whiteley, J.; Dong, H.; Hu, P.; Lee, S.; Yao, Y. Tailored Organic Electrode Material Compatible with Sulfide Electrolyte for Stable All-Solid-State Sodium Batteries. *Angewandte Chemie International Edition* **2018**, *57*, 2630-2634.

(245) Yuan, Y.; Amine, K.; Lu, J.; Shahbazian-Yassar, R. Understanding materials challenges for rechargeable ion batteries with in situ transmission electron microscopy. *Nat. Commun.* **2017**, *8*, 15806.

(246) Lu, J.; Wu, T.; Amine, K. State-of-the-art characterization techniques for advanced lithium-ion batteries. *Nat. Energy* **2017**, *2*, 17011.

(247) Li, M.; Chen, Z.; Wu, T.; Lu, J. Li_2S- or S-Based Lithium-Ion Batteries. *Adv. Mater.* **2018**, 1801190.

(248) Wang, C.; Cai, W.; Li, G.; Liu, B.; Li, Z. In Situ Synthesis of Li_2S-Loaded amphiphilic Porous Carbon and Modification of the Li_2S Electrode for Long-Life Li_2S Batteries. *ChemElectroChem* **2018**, *5*, 112-118.

(249) Vizintin, A.; Chabanne, L.; Tchernychova, E.; Arčon, I.; Stievano, L.; Aquilanti, G.; Antonietti, M.; Fellinger, T.-P.; Dominko, R. The mechanism of Li_2S activation in lithium-sulfur batteries: Can we avoid the polysulfide formation? *J. Power Sources* **2017**, *344*, 208-217.

(250) Gerber, L. C. H.; Frischmann, P. D.; Fan, F. Y.; Doris, S. E.; Qu, X.; Scheuermann, A. M.; Persson, K.; Chiang, Y.-M.; Helms, B. A. Three-Dimensional Growth of Li_2S in Lithium–Sulfur Batteries Promoted by a Redox Mediator. *Nano Lett.* **2016**, *16*, 549-554.

(251) Li, M.; Bai, Z.; Li, Y.; Ma, L.; Dai, A.; Wang, X.; Luo, D.; Wu, T.; Liu, P.; Yang, L.; Amine, K.; Chen, Z.; Lu, J. Electrochemically primed functional redox mediator generator from the decomposition of solid state electrolyte. *Nat. Commun.* **2019**, *10*, 1890.

(252) Wei, S.; Xu, S.; Agrawral, A.; Choudhury, S.; Lu, Y.; Tu, Z.; Ma, L.; Archer, L. A. A stable room-temperature sodium–sulfur battery. *Nat. Commun.* **2016**, *7*, 11722.

(253) Yu, X.; Manthiram, A. Na_2S–Carbon Nanotube Fabric Electrodes for Room-Temperature Sodium–Sulfur Batteries. *Chemistry – A European Journal* **2015**, *21*, 4233-4237.

(254) Yu, X.; Manthiram, A. Performance enhancement and mechanistic studies of room-temperature sodium–sulfur batteries with a carbon-coated functional nafion separator and a Na_2S/activated carbon nanofiber cathode. *Chemistry of Materials* **2016**, *28*, 896-905.

(255) Wu, D. S.; Shi, F.; Zhou, G.; Zu, C.; Liu, C.; Liu, K.; Liu, Y.; Wang, J.; Peng, Y.; Cui, Y. Quantitative investigation of polysulfide adsorption capability of candidate materials for Li-S batteries. *Energy Storage Materials* **2018**, *13*, 241-246.

(256) Zou, Q.; Lu, Y.-C. Solvent-Dictated Lithium Sulfur Redox Reactions: An Operando UV–vis Spectroscopic Study. *The Journal of Physical Chemistry Letters* **2016**, *7*, 1518-1525.

(257) Cañas, N. A.; Fronczek, D. N.; Wagner, N.; Latz, A.; Friedrich, K. A. Experimental and Theoretical Analysis of Products and Reaction Intermediates of Lithium–Sulfur Batteries. *The Journal of Physical Chemistry C* **2014**, *118*, 12106-12114.

(258) Zhang, L.; Sun, D.; Feng, J.; Cairns, E. J.; Guo, J. Revealing the Electrochemical Charging Mechanism of Nanosized Li_2S by in Situ and Operando X-ray Absorption Spectroscopy. *Nano Lett.* **2017**, *17*, 5084-5091.

(259) Liang, X.; Hart, C.; Pang, Q.; Garsuch, A.; Weiss, T.; Nazar, L. F. A highly efficient polysulfide mediator for lithium–sulfur batteries. *Nat. Commun.* **2015**, *6*, 5682.

(260) Cañas, N. A.; Wolf, S.; Wagner, N.; Friedrich, K. A. In-situ X-ray diffraction studies of lithium–sulfur batteries. *J. Power Sources* **2013**, *226*, 313-319.

(261) Jha, H.; Buchberger, I.; Cui, X.; Meini, S.; Gasteiger, H. A. Li-S Batteries with Li_2S Cathodes and Si/C Anodes. *J. Electrochem. Soc.* **2015**, *162*, A1829-A1835.

(262) Skoko, Ž.; Popović, J.; Dekanić, K. Insight into microstructural development by XBroad program: Case of in-situ formation of the Al–Zn solid solution. *J. Phys. Chem. Solids* **2015**, *80*, 34-38.

Permission Licenses:

Chapter 1:

License Number: 4866011068951 for *Advanced Materials* **2018,** *30*, 1800561. (License obtained July 11 2020)

License Number: 4866060756344 for *Advanced Materials*, **2018**, *30*, 1801190. (License obtained July 11 2020)

Chapter 3:

License Number: 4866060387953 for Advanced Functional Materials 2016, 26 (8408-8417). (License obtained July 11 2020)

Chapter 4:

License Number: 4866060702794 for Advanced Materials 2018, 30 (1804271). (License obtained July 11 2020)